On the thermomechanics of field dislocations

Gabriel Lima Chaves

INSTITUT POLYTECHNIQUE DE PARIS

NNT : 2024IPPAX058

Thèse de doctorat

ÉCOLE POLYTECHNIQUE

IP PARIS

On the thermomechanics of field dislocations

Thèse de doctorat de l'Institut Polytechnique de Paris
préparée à l'École polytechnique

École doctorale n°626 École doctorale de l'Institut Polytechnique de Paris (EDIPP)
Spécialité de doctorat : Mécanique des solides, génie mécanique, productique, transport et génie civil

Thèse présentée et soutenue à Palaiseau, le 16 Septembre 2024, par

GABRIEL DANTE LIMA-CHAVES

Composition du Jury :

Samuel Forest Research Director, Mines ParisTech (UMR CNRS 7633)	Président
Thomas Hochrainer Professor, Graz University of Technology	Rapporteur
Vincent Taupin Researcher, Université de Lorraine (UMR CNRS 7239)	Rapporteur
Jérémy Bleyer Researcher, École des Ponts ParisTech (UMR CNRS 8205)	Examinateur
Konstantinos Danas Research Director, École Polytechnique (UMR CNRS 7649)	Examinateur
Katrin Schulz Professor, Karlsruhe Institute of Technology	Examinatrice
Lev Truskinovsky Research Director, ESPCI Paris (UMR CNRS 7636)	Examinateur
Manas V. Upadhyay Professor, École Polytechnique (UMR CNRS 7649)	Directeur de thèse

To my wife…

Acknowledgements

I would like to express my gratitude to all those who have supported me throughout my PhD journey.
First and foremost, I extend my deepest thanks to my thesis supervisor, Manas V. Upadhyay. Your scientific guidance, support, and understanding during the challenging times related to my distance from family have been invaluable.
I am also grateful for the funding provided by the European Research Council (ERC) through the European Union's Horizon 2020 research and innovation program for project GAMMA (grant agreement No. 946959).
I would like to acknowledge the Laboratoire de Mécanique des Solides for providing the necessary resources and facilities for my research, as well as the laboratory's staff for their support.
I also want to thank my friends and colleagues, especially my teammates Abdellah, Guillermo, Kewei, Nikhil and Steve. Your encouragement, camaraderie, and insightful discussions have made this journey not only manageable but also enjoyable. I am truly fortunate to have shared this experience with such supportive individuals.
Lastly, I would like to acknowledge the fruitful collaboration with Amit Acharya from Carnegie Mellon University. Our exchanges were really enjoyable and taught me a great deal.

Palaiseau, 16 Septembre 2024 G.D. L.C.

Abstract

This thesis investigates the coupling between dislocation evolution and heat conduction in continuum bodies through a theoretical and numerical approach. The main objectives are twofold: (i) to develop a finite deformation theory of thermomechanics of field (i.e. continuously represented) dislocations that account for the interplay between dislocation activity and temperature evolution, while considering only observable fields; (ii) to propose a geometrical linearisation of the finite deformation theory showing that it is similar to the small deformation thermal field dislocation mechanics (TFDM) theory proposed in Upadhyay, J. Mech. Phys. Solids, 145 (2020) 104150, and numerically implement the latter using the finite element (FE) approach to study temperature evolution during dislocation transport.

The fundamental aspects of dislocation modelling are reviewed, highlighting the different approaches that have commonly been used to study dislocation-based plasticity in crystals. After identifying the current limitations of the state of the art, a theory with a novel kinematics for thermo-elastoplastic problems based on dislocation mechanics in a finite deformation framework within a transient heterogeneous temperature field is proposed. The theory does not require the specification of a global reference configuration, whence we do not make use of a multiplicative decomposition of the deformation gradient into elastic, plastic, and thermal parts. Instead, considering only observable state variables, we show that the kinematics based on the conservation of Burgers vector is sufficient to yield the commonly-accepted additive decomposition of the velocity gradient into elastic, plastic, and thermal distortion rates. Accounting for the polar dislocation density as a state variable in the Helmholtz free energy of the system, using the first and second laws of thermodynamics, we obtain a new structure of the temperature evolution equation, which allows for solutions in the form of dispersive waves with finite propagation speed without a second derivative of the temperature field in time.

The developed theory is shown to reduce, when geometrically linearised, to the small-strain TFDM theory previously proposed. Then, the focus is turned to the latter, and the variational forms of its partial differential equations (PDEs) are presented. Using an open-source library designed to solve PDEs with the FE method, the variational forms are implemented in a staggered algorithm. The implementation is verified against an analytical solution for the temperature field generated by a moving dislocation, and excellent agreement is obtained. Some of the TFDM capabilities are then explored in examples of the heat generated by single edge/screw dislocation,

dislocation annihilation, and dislocation loop expansion, which provide a clear understanding of the transient thermoelastic and plastic heat sources involved in each case.
The present research advances the field of continuum dislocation modelling by proposing a novel theoretical framework, as well as the numerical implementation of its linearised version. This work serves as a basis for understanding the evolution of dislocation structures during different thermomechanical processes, such as metal additive manufacturing, welding, quenching, etc., which would ultimately contribute to better controlling the mechanical properties of manufactured parts. Future work would include an extension of the numerical implementation to the general finite-deformation theory proposed, as well as an upscaling of the latter to account for the role of statistically stored dislocations in classical problems of plasticity.

Keywords: dislocations, solid mechanics, plasticity, thermoelasticity, FEM

Résumé

Cette thèse explore le couplage entre l'évolution des dislocations et la conduction thermique dans les corps continus à travers une approche théorique et numérique. Les principaux objectifs sont : (i) développer une théorie de la thermomécanique des champs de dislocation en grandes déformations qui tient compte de l'interaction mutuelle entre l'activité des dislocations et l'évolution de la température, tout en considérant uniquement des champs observables ; (ii) proposer une linéarisation géométrique de cette théorie en montrant qu'elle revient à la théorie thermomécanique des champs de dislocations (TFDM) en petites déformations proposée par Upadhyay, J. Mech. Phys. Solids, 145 (2020) 104150, et implémenter numériquement cette dernière en utilisant la méthode des éléments finis (EF) pour étudier l'évolution de la température pendant le transport des dislocations.

Les aspects fondamentaux de la modélisation des dislocations sont passés en revue, mettant en évidence les différentes approches couramment utilisées. Après avoir identifié les limitations actuelles de l'état de l'art, une théorie avec une nouvelle cinématique basée sur la mécanique des dislocations dans un cadre de grandes déformations considérant un champ de température hétérogène transitoire est proposée. La théorie ne nécessite pas la spécification d'une configuration de référence globale, d'où l'absence de décomposition multiplicative du gradient de déformation en parties élastique, plastique et thermique. Au lieu de cela, en ne considérant que des variables d'état observables, il est montré que la cinématique basée sur la conservation du vecteur de Burgers est suffisante pour obtenir la décomposition additive couramment acceptée du gradient de vitesse en taux de distorsion élastique, plastique et thermique. En prenant en compte la densité de dislocations polaires comme variable d'état dans l'énergie libre de Helmholtz du système, et en utilisant les première et deuxième lois de la thermodynamique, une nouvelle structure de l'équation d'évolution de la température est obtenue, permettant des solutions sous forme d'ondes dispersives avec une vitesse de propagation finie, sans dérivée seconde du champ de température dans le temps.

La théorie développée est montrée se réduire, sous linéarisation géométrique, à la théorie TFDM en petites déformations précédemment proposée. Ensuite, l'accent est mis sur cette dernière, et les formes variationnelles de ses équations aux dérivées partielles (EDP) sont présentées. En utilisant une bibliothèque open-source conçue pour résoudre les EDP avec la méthode des EF, les formes variationnelles sont implémentées dans un algorithme échelonné. L'implémentation est vérifiée par rapport à une solution analytique pour le champ de température généré par une

dislocation en mouvement, et un excellent accord est obtenu. Certaines des capacités de TFDM sont ensuite explorées dans des exemples de chaleur générée par le mouvement d'une dislocation coin/vis, l'annihilation des dislocations et l'expansion des boucles de dislocations, fournissant une compréhension en profondeur des sources de chaleur thermoélastiques et plastiques transitoires impliquées dans chaque cas.
La présente recherche fait progresser le domaine de la modélisation des champs de dislocations en proposant un nouveau cadre théorique, ainsi que l'implémentation numérique de sa version linéarisée. Ce travail sert de base à la compréhension de l'évolution des structures de dislocations lors de différents processus thermomécaniques, tels que la fabrication additive de métaux, le soudage, la trempe, etc., ce qui pourrait contribuer à un meilleur contrôle des propriétés mécaniques des pièces fabriquées. Les travaux futurs incluraient une extension de l'implémentation numérique à la théorie proposée en grandes déformations, ainsi qu'un échelonnement de cette dernière pour tenir compte du rôle des dislocations statistiquement stockées dans les problèmes classiques de plasticité.

Mots clés : dislocations, mécanique des solides, plasticité, thermoélasticité, FEM

Contents

Acknowledgements i

Abstract (English/Français) iii

List of figures xi

1 Introduction 1
- 1.1 Context . . . 1
- 1.2 State of the art . . . 2
  - 1.2.1 Discrete modelling of dislocations . . . 2
  - 1.2.2 Continuum modelling of dislocations . . . 5
- 1.3 Problem statement and research questions . . . 12

2 Finite deformation thermomechanical theory of field dislocations 15
- 2.1 Abstract . . . 15
- 2.2 Introduction . . . 16
  - 2.2.1 Ordering-dependence of the multiplicative decomposition in finite deformation elastoplasticity . . . 19
- 2.3 Kinematics . . . 25
  - 2.3.1 Distortion fields and configurations . . . 25
  - 2.3.2 The thermomechanical line defect – a consequence of the definition of the Burgers vector . . . 26
  - 2.3.3 Conservation of Burgers vector . . . 28
- 2.4 Balance laws, dissipation analysis and constitutive equations . . . 30
  - 2.4.1 Mass balance . . . 30
  - 2.4.2 Balance of linear and angular momentum . . . 30
  - 2.4.3 First law of thermodynamics . . . 31
  - 2.4.4 Second law of thermodynamics . . . 31
  - 2.4.5 Helmholtz free energy density and constitutive relations . . . 32
  - 2.4.6 Temperature evolution . . . 34
  - 2.4.7 Taylor-Quinney coefficient . . . 39
  - 2.4.8 Initial boundary value problem of finite deformation field dislocations thermomechanics . . . 41
- 2.5 Geometric linearisation . . . 43

2.5.1 Boundary conditions . . . 46
2.5.2 Initial conditions . . . 47
2.6 Some examples for a given Helmholtz free energy density expressions . . . 47
2.6.1 Finite deformation: Saint-Venant-Kirchoff model with defect core energy 47
2.6.2 Small deformation: Saint-Venant-Kirchoff model with defect core energy 48
2.6.3 Comparison with the model proposed by Upadhyay, 2020 . . . 50
2.7 Conclusion . . . 51

3 Finite element implementation of the small deformation TFDM 53
3.1 Abstract . . . 53
3.2 Introduction . . . 54
3.3 The TFDM model . . . 55
3.3.1 Field equations of TFDM . . . 55
3.3.2 Boundary and initial conditions . . . 57
3.3.3 Nondimensionalization . . . 58
3.4 Finite element formulation and algorithm . . . 58
3.4.1 Evolution of $\boldsymbol{\alpha}^p$ . . . 58
3.4.2 Computation of $\boldsymbol{\chi}^p$ . . . 60
3.4.3 Evolution of $\boldsymbol{z}^p$ . . . 60
3.4.4 Computation of $\boldsymbol{u}$ . . . 60
3.4.5 Evolution of θ . . . 61
3.4.6 Small-strains TFDM-FE algorithm . . . 61
3.5 Results and discussion . . . 61
3.5.1 Temperature evolution due to dislocation motion: comparison between TFDM-FE and analytical solution . . . 61
3.5.2 Illustrative examples . . . 66
3.6 Conclusion and perspectives . . . 74

4 Conclusion 77
4.1 Summary of the research findings . . . 77
4.1.1 Thermomechanical theory of field dislocations . . . 77
4.1.2 Numerical implementation of the TFDM theory . . . 78
4.2 Recommendations for future research . . . 79

A Notation 81

B Invariance requirements of Y 83

C Ericksen's identity 85

D Linear stability analysis of the temperature evolution equation 87

E The Stokes-Helmholtz decomposition of W **93**
E.1 Large deformations 93
E.2 Small deformations 95

F Derivation of global dissipation rate D **97**

G Evaluation of the derivatives of Ψ for a Saint-Venant-Kirchhoff material **99**
G.1 Large deformations 99
G.2 Small deformations 100

H Supplementary figures for Chapter 3 **101**

Bibliography **111**

List of Figures

1.1 Relaxed (Ω_r) and current (Ω_t) configurations, with a dislocation core D represented, for the definition of the Burgers vector 7
1.2 Schematic representation of a dislocation line crossing an arbitrary surface element $\mathbf{d}\boldsymbol{S}_\Gamma$, adapted from Acharya, 2011. 9

2.1 Stress and plastic distortion evolution during simple shear, considering different orderings of the multiplicative decomposition of the deformation gradient tensor. 23
2.2 Stress and plastic distortion evolution during a combined stretch, contraction and shear, considering different orderings of the multiplicative decomposition of the deformation gradient tensor. 24
2.3 The transformation of Ω_t by $\boldsymbol{W}$, the only distortion tensor involved in this work. The $\nabla\theta_i$ represents that each polygon i is allowed to have a temperature gradient, as long as Ω_r remains stress-free. The additive decomposition of the velocity gradient into elastic, thermal and plastic parts is also shown and further discussed in Section 2.3.3. 26

3.1 Comparison of temperature profiles due to dislocation motion computed by the TFDM model and an analytical solution 65
3.2 Temperature field generated due to the motion of an edge dislocation 67
3.3 Temperature field generated due to the motion of a screw dislocation 68
3.4 Heat sources during edge and screw dislocation motion 69
3.5 Temperature field generated during the annihilation of two edge dislocations . . 72
3.6 Temperature field generated during a polygonal dislocation loop expansion . . . 75

H.1 Mesh used for the TFDM model verification 101
H.2 Heat sources evolution during edge dislocation annihilation 102
H.3 Mesh used for the loop expansion simulation 103

1 Introduction

In this thesis, a continuum theory of dislocation thermomechanics in a finite deformation framework is proposed, and its small deformation counterpart, which reduces to the theory proposed in Upadhyay, 2020, is numerically implemented. The theory aims at capturing the interplay between transient temperature gradients (in the solid state) and dislocation evolution (specifically, transport, annihilation, and generation) during thermomechanical processes such as metal additive manufacturing (AM), quenching, welding, rolling, etc., and in service conditions.

1.1 Context

Dislocations are line-type defects that are ubiquitous in crystalline materials and their evolution is thermomechanically activated. Thus far, much research efforts have been directed towards understanding dislocation mechanics in an isothermal setting at different temperatures. It is now well understood that higher temperatures lead to more pronounced atomic vibrations, which lower the activation barrier for dislocation kinetics (nucleation, interactions, transport). However, isothermal studies are insufficient to understand dislocation evolution occurring during complex thermomechanical processes such as AM, quenching, welding, rolling, etc., which result in strong transient temperature gradients.

Among the processes listed above, heat-matter interactions during AM result in some of the most extreme thermal conditions: strong temperature gradients (up to ~ 10 K/μm) and heating/cooling rates (up to $\sim 10^7$ K/s). A recent *in situ* X-ray diffraction experiment (Gaudez et al., 2023) conclusively demonstrated, for the first time, a strong evolution of dislocation structures in the solid state during AM. These results have set the stage for theoretical developments capable of providing a clear understanding of the evolution of dislocation structures due to transient thermal gradient effects. The research presented in this thesis focusses on developing such a theory.

Gaining a deeper insight into dislocation evolution during such processes requires a theoretical framework that explicitly considers the interaction between dislocation activity and temperature changes. This framework must account for the effect of thermomechanical boundary conditions

on the evolution of dislocations, thus being able to solve initial boundary value problems of dislocation thermomechanics, which typically involve time intervals and lengthscales of $\sim$ ms and $\sim \mu$m, respectively. As a first possibility in that direction, one could consider using an atomistic approach such as molecular dynamics (MD), which explicitly accounts for atomic positions and the interactions between atoms in bodies that may contain dislocations. However, due to its significant computational cost, this approach is limited to simulating very small domains ($\sim$ nm) for time intervals of the order of ns.

To that end, the theoretical developments are performed in a continuum framework. The proposed framework is endowed with the minimum necessary tools to tackle the initial boundary value problem of dislocation thermomechanics in a finite deformation setting that accounts for the interplay between transient temperature gradients and dislocation evolution (transport, annihilation, generation). Crystallography will not be explicitly incorporated in this framework, but the framework will be designed in such a way that it allows for accounting for crystallography; this aspect will be addressed in the perspectives Section 4.2.

The proposed framework derives its motivation from the small deformation thermal field dislocation mechanics (TFDM) theory, proposed by Upadhyay, 2020, which finds its roots in Kröner, 1958; Acharya, 2011. TFDM is a thermodynamically rigorous framework designed to study the dynamics of dislocations in bodies that undergo rapid temperature changes due to the imposed thermomechanical boundary conditions while also accounting for the dislocation activity contribution to temperature evolution. The finite-deformation thermomechanical theory of dislocations proposed here will be shown to reduce to TFDM when geometrically linearised; a numerical implementation of TFDM is presented to study some test cases of temperature evolution due to dislocation evolution.

In what follows, the state of the art is presented with a particular focus on the lead-up to the development of the TFDM model, and the thesis objectives are clearly stated.

1.2 State of the art

Although continuum dislocation modelling is the chosen framework in this research, for completeness, the following section presents a brief overview of the discrete modelling approaches that have been proposed to study dislocation mechanics.

1.2.1 Discrete modelling of dislocations

Dislocations first appeared as an abstract mathematical concept in the work of Volterra, 1907, which studied the equilibrium aspects of multiply connected elastic bodies. The link between dislocations and plasticity in crystals can be traced back to the discussion on the theoretical strength of a perfect crystal, first calculated by Frenkel, 1926 (Hull and Bacon, 2011). In this case, considering the shearing between two adjacent atom planes, plastic deformation would require

breaking at once all of the atomic bonds between these planes, displacing one plane relative to the other, and rebonding the atoms. In theory, this process would require considerable applied shear stress to overcome the barrier imposed by all these atomic bonds and initiate plastic flow.

However, the experimental observations at that time did not support this proposition; instead, multiple experiments resulted in shear stresses necessary to generate plastic deformation that were around 4 orders of magnitude below the theoretical estimate. In order to explain this discrepancy between the theoretical strength of a perfect crystal and the experimental results, Orowan, 1934; Polanyi, 1934; Taylor, 1934 independently proposed the concept of edge dislocation, which consists of an extra half-plane of atoms that ends in a line (the dislocation line) inside the microstructure. Plastic deformation would then stem from the motion of this line on a slip plane, produced by the subsequent debonding-rebonding of atoms in the vicinity of the dislocation line as a response to an externally applied shear stress. Shortly after, Burgers, 1939 introduced the description of a screw dislocation line, around which the atomic planes would be distorted in a "screw-like" fashion. The motion of these dislocation lines would require considerably smaller stresses compared to the perfect-crystal case because much fewer atomic bonding ruptures are involved in the process resulting in plastic deformation. Considering that most metals contain several of these dislocation lines, this would explain the discrepancy between the theoretical strength of a perfect crystal and the experimental observations. The confirmation of the existence of edge and screw dislocations in materials followed the development of imaging techniques such as electron microscopy, X-ray diffraction, and decoration methods, among others (Gevers et al., 1978; Hull and Bacon, 2011).

Subsequently, many theoretical approaches were introduced in an attempt to better understand and explain the different phenomena that were experimentally observed, involving the behaviour of a single dislocation and a collection of dislocations.

The smallest (atomic) scale models describe the region surrounding dislocation cores. Among such models, ab initio calculations based on density functional theory (DFT) are the most commonly used due to their powerful predictiveness (Clouet, 2018). In essence, ab initio calculations aim to describe the bonding between atoms through the resolution of Schrödinger's equation for the electrons in a body. Instead of solving the equation for each coordinate of each electron in the system, the DFT only considers the electronic density, which is a function of the atomic positions. In the context of dislocations, it is considered that only the valence electrons contribute to the atomic bonding, assuming that the innermost electrons have the same ground state as the isolated atom (Clouet, 2018). By accurately solving for dislocation cores, ab initio methods allow access to different local properties of the dislocations such as cross-slip and nucleation processes, the selection of glide planes where dislocation motion takes place, and the dislocation mobility that governs the motion (Rodney et al., 2017). However, because of their considerable computational cost, ab initio modelling of metals usually only allows a few hundred atoms to be simulated, which limits the domain of application of such methods.

Within the context of classical mechanics at the atomic level, molecular statics and molecular

dynamics (MS and MD) models consider atomic positions as degrees of freedom. Atoms are assumed to interact through a potential function depending on their positions, and in MS, the atomic positions are calculated by minimising the potential energy of a set of atoms to reach the ground equilibrium state of a system, which may include dislocations. In MD, the atomic trajectories are computed by integration of Newton's second law of motion (Bulatov and Cai, 2006) with the appropriate initial and boundary conditions. MS and MD simulations are usually informed by ab initio calculations, which provide the interatomic potential function for a specific atomic system. MD simulations allow for studying dislocation mobility, cross-slip, interactions of dislocations between themselves and with other defects such as grain boundaries, twins, precipitates, etc. Although being less computationally expensive than ab initio methods, MD simulations of metals are still limited to systems of $\sim 10^6$ atoms. Moreover, integration of the equations of motion requires very small time steps (~ 1 fs), which limits the application of MD simulations to very high strain rate scenarios, usually above 10^6 s^{-1} (Bertin et al., 2020; Bertin and Zhou, 2023).

On a larger scale ($\sim \mu$m), in the discrete dislocation dynamics (DDD) approach, the dislocations are represented as line segments embedded in an elastic continuum (Kubin et al., 1992; Weygand et al., 2001; Bulatov and Cai, 2006; Bertin et al., 2020), and the motion of and interaction between these segments is governed by prespecified rules that may account for the various dislocation-related phenomena, such as cross-slip, junction formation, annihilation, nucleation, etc. In this case, the degrees of freedom are the nodal positions at the extremities of each line segment, as well as the Burgers vector associated with the former. For a given set of line segments and Burgers vector that compose the dislocation network, the stress field can be computed using continuum linear elasticity. Given the stress state, the force on each segment of the dislocation line is computed (the Peach-Koehler force, Peach and Koehler, 1950) and is the force that will drive the motion of the segment according to a given mobility law. A strict bookkeeping scheme is required to keep track of the trajectory of each node and the eventual interactions between line segments. DDD simulations usually output quantities such as dislocation density, stored energy, accumulated shear strain, local stresses, and the final dislocation microstructure resulting from some deformation process (Fivel, 2008). Compared to atomistic simulations, the DDD approach has a significantly lower computational cost. However, the cost is still considerable if one wants to simulate typical strains and strain rates achieved in plasticity experiments, despite current advances in that direction (Bertin et al., 2019). In the context of thermomechanical processes, Cui et al., 2022 proposed a multi-scale approach that couples DDD and the finite element method to simulate the evolution of dislocations during the additive manufacturing of tungsten. In their work, the impact of the thermal gradient on the DDD simulation cell is not considered. Moreover, a one-way coupling between temperature evolution and dislocation activity is assumed, in which the heat generated by plastic flow is neglected.

In the context of this research, continuum approaches to dislocation modelling provide a suitable framework to model the length and time scales involved in the thermomechanical processes of interest here (see Section 1.1). Moreover, addressing the necessary thermal and mechanical boundary conditions is a built-in capability of such approaches, which also allow for a rather

straightforward and physics-based coupling between plasticity, mechanical equilibrium, and temperature evolution through the expression of conservation laws. Therefore, these continumm approaches are discussed in more detail in the next section.

1.2.2 Continuum modelling of dislocations

Most continuum dislocation models are introduced based on the notion of the dislocation density tensor (also usually called Nye's tensor) $\boldsymbol{\alpha}$, introduced by Nye, 1953, which is a second-order tensor, usually non-symmetric. In his work, Nye used geometrical arguments to show how the curvature of a crystal lattice can be related to $\boldsymbol{\alpha}$ through the relation

$$\boldsymbol{\kappa} = \boldsymbol{\alpha} - \frac{1}{2}\mathrm{tr}(\boldsymbol{\alpha})\mathbb{1}, \tag{1.1}$$

where $\boldsymbol{\kappa}$ denotes the lattice curvature tensor[1]. Crucially, Nye, 1953 also presented the precise nature of $\boldsymbol{\alpha}$ in terms of an ensemble of dislocation lines. Considering n dislocations whose lines are parallel to the unit vector $\boldsymbol{l}$ and whose Burgers vector is $\boldsymbol{b}$, it is shown that

$$\boldsymbol{\alpha} = n\boldsymbol{b} \otimes \boldsymbol{l}. \tag{1.2}$$

Hence, $\boldsymbol{\alpha}$ can fully describe the dislocation state in a body with respect to a given coordinate system. The diagonal components of $\boldsymbol{\alpha}$ contains information on the screw dislocation components, for which $\boldsymbol{b}$ and $\boldsymbol{l}$ are parallel, and the off-diagonal components represent the edge dislocation components, for which $\boldsymbol{b} \cdot \boldsymbol{l} = 0$. Finally, the following property of $\boldsymbol{\alpha}$ is also shown

$$\nabla \cdot \boldsymbol{\alpha} = 0, \tag{1.3}$$

which is the continuum equivalent of the statement that a dislocation line cannot end inside a body.

In Kröner, 1958, the fundamental relation between $\boldsymbol{\alpha}$ and the incompatibility in the plastic distortion tensor $\boldsymbol{U}^p$ was introduced, which reads

$$\boldsymbol{\alpha} = -\nabla \times \boldsymbol{U}^p. \tag{1.4}$$

Crutial for the continuum modelling of dislocations in thermomechanical processes is the idea that dislocations might be generated from temperature gradients, proposed in Kröner, 1958. Kröner stated that, within a continuous medium subjected to a non-uniform temperature distribution, elastic distortions can be eliminated by adding a dislocation density proportional to the curl of thermal strains, that is,

$$\boldsymbol{\alpha}^\theta \equiv -\nabla \times \boldsymbol{\varepsilon}^\theta, \tag{1.5}$$

[1]The mathematical notation used in this chapter can be found in Appendix A

where $\boldsymbol{\alpha}^{\theta}$ is introduced as a "quasi-dislocation" density and $\boldsymbol{\varepsilon}^{\theta}$ is the symmetric thermal strain tensor. The term "quasi-dislocation" stems from the fact that, rather than manifesting as a physical line defect in the material, $\boldsymbol{\alpha}^{\theta}$ is solely induced from incompatibilities in thermal strains.

In the following, different works were aimed at proposing continuum theories of internal stresses due to defects, notably due to dislocations. Building on the works of Eshelby, 1956 and Kröner, 1958, deWit, 1960 described a continuum theory of stationary dislocations, in a linearised isotropic elasticity setting. In his work, Green tensor functions are used to compute the displacement field due to the presence of a dislocation, with which the resulting stress field can also be obtained. Moreover, energy expressions for some dislocation line geometries are presented.

In Willis, 1967, the problem of determining the internal stress distribution due to dislocations is solved in a finite deformation framework while also allowing for the treatment of anisotropic materials. Based on this work, the following definition of the Burgers vector in a continuum framework is proposed. Consider a body $\mathcal{B} \subset \mathcal{E}^3$, where $\mathcal{E}^3$ denotes the three-dimensional Euclidean point space, which occupies different configurations $\Omega_i \subset \mathbb{R}^3$ that define the motion of the body. In particular, consider the current configuration Ω_t, in which dislocations are present and external boundary conditions are applied, as well as a relaxed, stress-free configuration Ω_r[2] (Fig. 1.1). An elastic distortion tensor $\boldsymbol{F}^e$ can be defined that maps tangent vectors between Ω_r and Ω_t, i.e.

$$\mathrm{d}\boldsymbol{x} = \boldsymbol{F}^e \mathrm{d}\boldsymbol{x}_r \quad \text{and} \quad \mathrm{d}\boldsymbol{x}_r = \boldsymbol{W}\,\mathrm{d}\boldsymbol{x}, \qquad \mathrm{d}\boldsymbol{x}_r \in \Omega_r, \mathrm{d}\boldsymbol{x} \in \Omega_t, \tag{1.6}$$

where $\boldsymbol{W} := \boldsymbol{F}^{e-1}$. By writing the displacement vector as

$$\boldsymbol{u}(\boldsymbol{x}, t) = \boldsymbol{x} - \boldsymbol{x}_r(\boldsymbol{x}, t), \tag{1.7}$$

the displacement can be computed at $\boldsymbol{x}_2$ (Fig. 1.1) as

$$\boldsymbol{u}(\boldsymbol{x}_2, t) = \boldsymbol{u}(\boldsymbol{x}_1, t) + \int_{\boldsymbol{x}_1}^{\boldsymbol{x}_2} (\nabla_x \boldsymbol{u})\,\mathbf{d}\boldsymbol{l}, \tag{1.8}$$

where the line integral is evaluated along a path joining $\boldsymbol{x}_1$ and $\boldsymbol{x}_2$, and $\mathbf{d}\boldsymbol{l}$ is the tangent vector to this path. Considering a closed path c_t (Fig. 1.1), the displacement at $\boldsymbol{x}_1 \in c_t$ can be written as

$$\boldsymbol{u}(\boldsymbol{x}_1^+, t) = \boldsymbol{u}(\boldsymbol{x}_1^-, t) + \oint_{c_t} (\nabla_x \boldsymbol{u})\,\mathbf{d}\boldsymbol{l}, \tag{1.9}$$

where $\boldsymbol{x}_1^+$ and $\boldsymbol{x}_1^-$ denote the limits on c_t to $\boldsymbol{x}_1$ from the left and from the right, respectively. In the absence of a dislocation core within c_t, the displacement at $\boldsymbol{x}_1$ is single-valued, such that

[2] A detailed description of the conceptual obtention of Ω_r from Ω_t can be found in Willis, 1967 and Zhang et al., 2015 Sec. 4.1

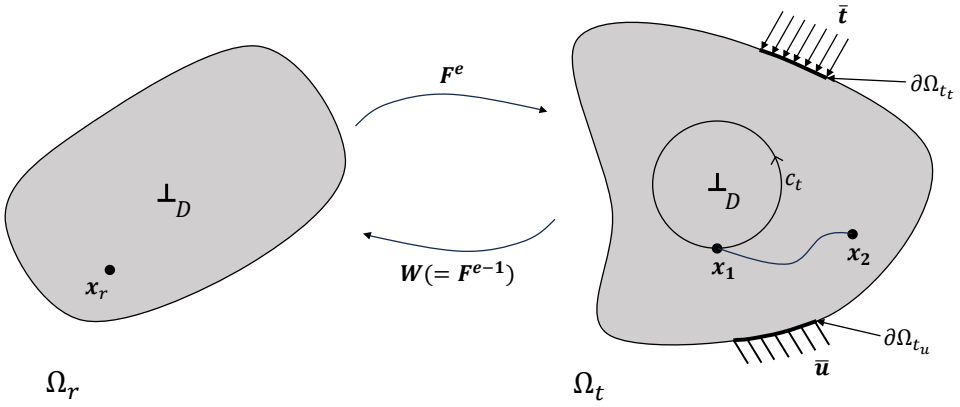

Figure 1.1: Relaxed (Ω_r) and current (Ω_t) configurations, with a dislocation core D represented. Points in Ω_r (Ω_t) are denoted $\boldsymbol{x}_r$ ($\boldsymbol{x}$). Ω_t may have applied boundary tractions $\bar{\boldsymbol{t}}$ on the boundary portion $\partial\omega_{t_t}$, as well as imposed displacements $\bar{\boldsymbol{u}}$ on the boundary portion $\partial\Omega_{t_u}$.

$\boldsymbol{u}(\boldsymbol{x}_1^+,t)=\boldsymbol{u}(\boldsymbol{x}_1^-,t)$ and

$$\oint_{c_t}(\nabla_x\boldsymbol{u})\,\mathbf{d}\boldsymbol{l}=0.$$

However, considering that c_t encloses a dislocation core D, $\boldsymbol{u}(\boldsymbol{x}_1,t)$ becomes multi-valued, and thus

$$\boldsymbol{u}(\boldsymbol{x}_1^+,t)-\boldsymbol{u}(\boldsymbol{x}_1^-,t)=\boldsymbol{b}_r=\oint_{c_t}\boldsymbol{U}\,\mathbf{d}\boldsymbol{l}, \tag{1.10}$$

where $\boldsymbol{b}_r\in\Omega_r$ is the ("true", as in Willis, 1967) Burgers vector, and $\boldsymbol{U}$ denotes the distortion tensor, which can no longer be represented as the gradient of a vector field due to the presence of the dislocation core D. Now, from Eq. (1.7), consider

$$\nabla_x\boldsymbol{u}=\mathbb{1}-\nabla_x\boldsymbol{x}_r=\mathbb{1}-\boldsymbol{W}. \tag{1.11}$$

Inserting Eq. (1.11) into Eq. (1.8), and carrying out a subsequent analysis similar to the above, the following relationship is obtained

$$\boldsymbol{b}_r=-\oint_{c_t}\boldsymbol{W}\,\mathbf{d}\boldsymbol{l}. \tag{1.12}$$

Note that Eq. (1.12) is a direct consequence of the presence of the dislocation core D, which

introduces an incompatibility in $\boldsymbol{W}$. Applying Stokes' theorem to Eq. (1.12) yields

$$\boldsymbol{b}_r = \int_{s_t} -(\nabla \times \boldsymbol{W})\,\hat{\boldsymbol{n}}\, ds = \int_{s_t} \boldsymbol{\alpha}\hat{\boldsymbol{n}}\, ds, \tag{1.13}$$

where s_t is a closed surface bounded by c_t, whose unit normal field is $\hat{\boldsymbol{n}}$, and $\boldsymbol{\alpha} := -\nabla \times \boldsymbol{W}$ is the dislocation density tensor.

The study of the dynamic case, in which the dislocations move, can be attributed to Mura, 1963; Kosevich, 1979. These authors introduced a kinematic equation of evolution of $\boldsymbol{\alpha}$ in the form of a Burgers vector conservation statement, in a small deformation setting, and without considering source terms that model dislocation nucleation. The expression obtained reads

$$\dot{\boldsymbol{\alpha}} = -\nabla \times (\boldsymbol{\alpha} \times \boldsymbol{v}^d) \tag{1.14}$$

where $\boldsymbol{v}^d$ is the dislocation velocity vector. As shown in Mura, 1963; Kosevich, 1979, the term $\boldsymbol{\alpha} \times \boldsymbol{v}^d$ corresponds to the plastic strain rate due to the motion of dislocation lines, and can be regarded as a "dislocation flux density" (Kosevich, 1979). To provide a further understanding of the physical implications of transport of the dislocation density expressed by Eq. (1.14), we follow the analysis proposed in Appendix B of Acharya, 2011 and analyze the components of $\dot{\boldsymbol{\alpha}}$ relative to a Cartesian coordinate system depicted in Fig. 1.2b. The coordinate system is such that the tangent vector $\mathbf{d}\boldsymbol{x}$ of Γ is in the direction of $\boldsymbol{e}_1$. Without loss of generality, it is assumed that the normal vector $\boldsymbol{n}$ is not parallel to $\boldsymbol{e}_1 \times \boldsymbol{e}_2$ or $\boldsymbol{e}_1 \times \boldsymbol{e}_3$. Referring to the dislocation line in Fig. 1.2a, note that only the velocity components in the direction of $\mathbf{d}\boldsymbol{S}_\Gamma$ generate a flux of $\boldsymbol{b}$ across Γ.

As a reminder, the action of a second-order tensor on a basis vector is written as

$$\boldsymbol{\alpha}\boldsymbol{e}_j = \alpha_{ik}(\boldsymbol{e}_i \otimes \boldsymbol{e}_k)\boldsymbol{e}_j = \alpha_{ik}\delta_{jk}\boldsymbol{e}_i = \alpha_{ij}\boldsymbol{e}_i$$

Hence, for a single dislocation line, $\boldsymbol{\alpha} = \boldsymbol{b} \otimes \boldsymbol{t}$, then $\boldsymbol{\alpha}\boldsymbol{e}_j = b_i t_j \boldsymbol{e}_i$, that is, the sum of the Burgers vector components along the line direction $\boldsymbol{e}_j$. The flux term $\boldsymbol{\alpha} \times \boldsymbol{v}^d$ can be decomposed into the coordinate system $\{\boldsymbol{e}_i\}$ as (Acharya, 2011)

$$\begin{aligned}(\boldsymbol{\alpha} \times \boldsymbol{v}^d)\mathbf{d}\boldsymbol{x} &= \Big[(\alpha_{ij}\boldsymbol{e}_i \otimes \boldsymbol{e}_j) \times \boldsymbol{v}^d\Big]\mathrm{d}x\,\boldsymbol{e}_1 = \Big[(\boldsymbol{\alpha}\boldsymbol{e}_j) \otimes (\boldsymbol{e}_j \times \boldsymbol{v}^d)\Big]\mathrm{d}x\,\boldsymbol{e}_1 \\ &= \Big[(\boldsymbol{e}_j \times \boldsymbol{v}^d) \cdot \mathrm{d}x\,\boldsymbol{e}_1\Big](\boldsymbol{\alpha}\boldsymbol{e}_j)\end{aligned}$$

Using this result and explicitly writing the components of $\boldsymbol{v}^d$ in the coordinate system gives

$$\begin{aligned}(\boldsymbol{\alpha} \times \boldsymbol{v}^d)\mathbf{d}\boldsymbol{x} \;=\; &\left\{\left[\boldsymbol{e}_1 \times (v_1^d\boldsymbol{e}_1 + v_2^d\boldsymbol{e}_2 + v_3^d\boldsymbol{e}_3)\right] \cdot \mathrm{d}x\,\boldsymbol{e}_1\right\}(\boldsymbol{\alpha}\boldsymbol{e}_1) \\ &+ \left\{\left[\boldsymbol{e}_2 \times (v_1^d\boldsymbol{e}_1 + v_2^d\boldsymbol{e}_2 + v_3^d\boldsymbol{e}_3)\right] \cdot \mathrm{d}x\,\boldsymbol{e}_1\right\}(\boldsymbol{\alpha}\boldsymbol{e}_2) \\ &+ \left\{\left[\boldsymbol{e}_3 \times (v_1^d\boldsymbol{e}_1 + v_2^d\boldsymbol{e}_2 + v_3^d\boldsymbol{e}_3)\right] \cdot \mathrm{d}x\,\boldsymbol{e}_1\right\}(\boldsymbol{\alpha}\boldsymbol{e}_3).\end{aligned} \tag{1.15}$$

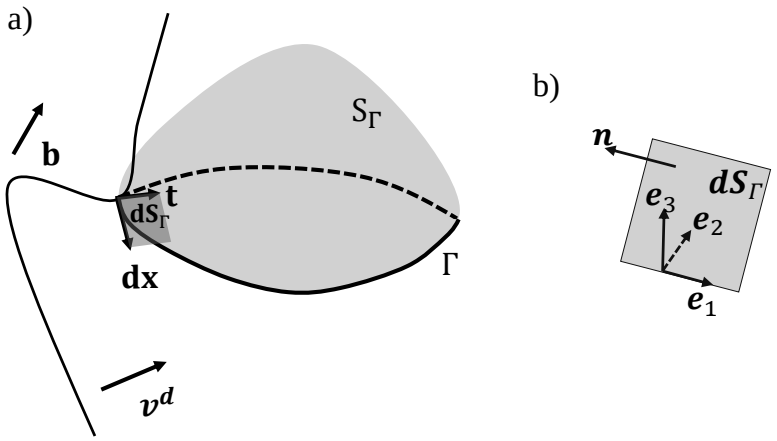

Figure 1.2: Schematic representation of a dislocation line crossing an arbitrary surface element $\mathbf{d}\boldsymbol{S}_\Gamma$, adapted from Acharya, 2011. a) Dislocation line with Burgers vector $\boldsymbol{b}$, line vector $\boldsymbol{t}$, and velocity vector $\boldsymbol{v}^d$, crossing an arbitrary curve Γ, with tangent vector $\mathbf{d}\boldsymbol{x}$, which encloses the surface S_Γ. b) Surface element $\mathbf{d}\boldsymbol{S}_\Gamma = \boldsymbol{t} \times \mathbf{d}\boldsymbol{x}$ with normal $\boldsymbol{n}$ and a local Cartesian coordinate system $\{\boldsymbol{e}_i\}$

The first line vanishes, and the remaining terms are

$$(\boldsymbol{\alpha} \times \boldsymbol{V})\mathbf{d}\boldsymbol{x} = v_3^d \mathrm{d}x(\boldsymbol{\alpha}\boldsymbol{e}_2) - v_2^d \mathrm{d}x(\boldsymbol{\alpha}\boldsymbol{e}_3),$$

that is, referring to Fig. 1.2, there can only be flux of the dislocation line across the curve Γ of the line components along direction $\boldsymbol{e}_2$ which have a velocity component along $\boldsymbol{e}_3$, and of the line components along direction $\boldsymbol{e}_3$ which have a velocity component along $\boldsymbol{e}_2$, which is expected. The line components that are tangent to Γ (that is, parallel to the basis vector $\boldsymbol{e}_1$) do not produce any flux, since they cannot enter or leave the surface element $\mathbf{d}\boldsymbol{S}_\Gamma$, which is shown by the first line of Eq. (1.15) vanishing identically.

1.2.2.1 Continuous Dislocation Dynamics (CDD)

Following the previously introduced notion of the dislocation density $\boldsymbol{\alpha}$, Hochrainer et al., 2007; Hochrainer et al., 2014; Hochrainer, 2015; Hochrainer, 2016 proposed a continuum dislocation dynamics model in which dislocations are natively distinguished based on their slip systems. The theory is based on a generalisation of $\boldsymbol{\alpha}$ to a higher-dimensional configurational space that contains variables characterising the direction of the dislocation line[3], leading to the definition of the "second order dislocation density" tensor $\boldsymbol{\alpha}^{\mathrm{II}}$ (Hochrainer et al., 2014). The latter is uniquely defined by two functions: the dislocation density ρ and the curvature density q. To handle the

[3]Considering a dislocation line with local tangent vector $\boldsymbol{t}$ and Burgers vector $\boldsymbol{b}$, an angle ϕ between $\boldsymbol{b}$ and $\boldsymbol{t}$ is assigned to each point on the dislocation line thus defining an extended configuration space in which the independent parameter is ϕ (Hochrainer et al., 2014)

significant computational cost introduced by the higher dimensionality of the problem, the authors consider the Fourier expansion of ρ and q, from which expansion coefficients the variables of the theory are extracted, namely the total dislocation density ρ_t, the dislocation density vector $\boldsymbol{\kappa}$, and the total curvature density q_t. The evolution equations for these variables are obtained by employing closure approximations that relate the higher-order Fourier coefficients of ρ and q in terms of lower-order ones, considered as the dynamic variables.

Another approach is presented in Starkey et al., 2020, consisting of a vector density representation of dislocations, also based on their respective slip systems, within the framework of finite deformation mesoscale crystal plasticity. For a given dislocation density ρ, the dislocation density vector is introduced as $\boldsymbol{\rho} = \rho \boldsymbol{t}$, with $\boldsymbol{t}$ being the unit tangent vector to the dislocation line, so that the dislocation density tensor can be written as $\boldsymbol{\alpha} = \boldsymbol{\rho} \otimes \boldsymbol{b}$. The authors adopt the multiplicative decomposition of the deformation gradient into elastic and plastic components and derive the transport equations for $\boldsymbol{\rho}$. Following a dissipation-based constitutive analysis, a mobility law for the dislocation velocity in terms of its driving force is proposed. A numerical implementation of the theory is shown in Starkey and El-Azab, 2022, and examples are given for a dislocation loop, a double-tilt boundary, and a uniaxial tensile test with Frank-Read dislocation sources.

1.2.2.2 Field Dislocation Mechanics (FDM)

Building on the works of Nye, 1953; Mura, 1963; Willis, 1967; Kosevich, 1979, Acharya introduced in Acharya, 2001, 2004 the FDM theory, consisting of a coupled system of partial differential equations (PDE) that describes crystal plasticity based on the theory of continuously distributed dislocations and the tensorial representation of the dislocation density. Dislocation-related variables are not introduced on a slip-system basis, under the expectation that slip-system-like behaviour will naturally emerge as an outcome of the theory (Acharya, 2004). In the latter, the transport equation of $\boldsymbol{\alpha}$ is used to evolve the dislocation density and is coupled to the stress field through the constitutive relation specified for the dislocation velocity $\boldsymbol{v}^d$. FDM is a model capable of accounting for the stress field of evolving dislocation densities at finite deformations in an anisotropic body, while also being able to account for intertial effects, without the need to specify neither a global reference configuration nor a multiplicative decomposition of the deformation gradient tensor $\boldsymbol{F}$. Instead, the inverse elastic distortion tensor $\boldsymbol{W} := \boldsymbol{F}^{e-1}$ is the only one needed.

Concerning Eq. (1.14), Acharya, 2001 considers an additional term $\boldsymbol{S}$ which represents the rate of generation of dislocations per unit area, such that the evolution statement for $\boldsymbol{\alpha}$ is written as

$$\dot{\boldsymbol{\alpha}} - \boldsymbol{\alpha}\boldsymbol{L}^T + \mathrm{tr}(\boldsymbol{L})\boldsymbol{\alpha} = -\nabla \times (\boldsymbol{\alpha} \times \boldsymbol{v}^d) + \boldsymbol{S} \tag{1.16}$$

where the two additional terms on the left-hand side arise from geometrical non-linearities in the framework of finite deformations, with $\boldsymbol{L}$ being the gradient of the velocity field on the current configuration. Essential to the theory, $\boldsymbol{v}^d$ and $\boldsymbol{S}$ are constitutively specified following a dissipation analysis based on the continuum description of the second law of thermodynamics.

Considering $\boldsymbol{\alpha}$ as the primary field of FDM, Acharya, 2001 argued about the impossibility of uniquely determining $\boldsymbol{W}$ and a displacement field for a given $\boldsymbol{\alpha}$. To avoid this issue, Acharya, 2004 introduced the Stokes-Helmholtz decomposition of $\boldsymbol{W}$ into incompatible and compatible parts as

$$\boldsymbol{W} = \boldsymbol{\chi} + \nabla \boldsymbol{f} \tag{1.17}$$

where $\boldsymbol{\chi}$ is a second-order incompatible tensor field, and $\boldsymbol{f}$ is the "plastic position vector" field (Acharya and Roy, 2006). Given $\boldsymbol{\alpha}$, $\boldsymbol{\chi}$ is computed by solving the system

$$\begin{aligned} &\nabla \times \boldsymbol{\chi} = -\boldsymbol{\alpha} \quad \text{in} \quad \Omega_t \\ &\left.\begin{aligned} \nabla \cdot \boldsymbol{\chi} = 0 \\ \boldsymbol{\chi}\hat{\boldsymbol{n}} = 0 \end{aligned}\right\} \quad \text{on} \quad \partial\Omega_t \end{aligned} \tag{1.18}$$

where $\hat{\boldsymbol{n}}$ is the unit normal field to the boundary $\partial\Omega_t$. The plastic deformation history is stored in $\nabla \boldsymbol{f}$, whose evolution is given by the following system (Acharya, 2004)

$$\begin{aligned} \nabla \cdot \nabla \dot{\boldsymbol{f}} &= \nabla \cdot \left(\boldsymbol{\alpha} \times \boldsymbol{v}^d + \boldsymbol{S} - \dot{\boldsymbol{\chi}} - \boldsymbol{\chi}\boldsymbol{L}\right) \quad \text{in} \quad \Omega_t \\ \left(\nabla \dot{\boldsymbol{f}}\right)\hat{\boldsymbol{n}} &= \left(\boldsymbol{\alpha} \times \boldsymbol{v}^d + \boldsymbol{S} - \dot{\boldsymbol{\chi}} - \boldsymbol{\chi}\boldsymbol{L}\right)\hat{\boldsymbol{n}} \quad \text{on} \quad \partial\Omega_t. \end{aligned} \tag{1.19}$$

alongside the specification of $\dot{\boldsymbol{f}}$ at an arbitrary point in Ω_t.

Acharya, 2011 proposed a microscopic interpretation of entropy and internal energy in the FDM theory by correlating the continuum entropy field with the statistical mechanics definition of entropy. The dissipative driving forces and energetic fields in FDM are defined through the use of the statistical mechanics notion of entropy of an isolated, constrained atomic system. An explicit link between the evolution of dislocation density and transient temperature variations was not established, and the effects of thermal strains in stress response was not considered.

1.2.2.3 Thermal Field Dislocation Mechanics (TFDM)

In Upadhyay, 2020, a strong coupling between the FDM theory and the heat conduction problem is proposed in a small deformation setting, resulting in the TFDM theory. TFDM is designed to study problems that involve strong temperature gradients and heating/cooling rates that may drive dislocation evolution and, alternatively, temperature evolutions that are generated by dislocation activity. This is achieved by considering the influence of the incompatibility in thermal strains on the evolution of $\boldsymbol{\alpha}$, which is written as

$$\dot{\boldsymbol{\alpha}} = \underbrace{-\nabla \times (\boldsymbol{\alpha}^p \times \boldsymbol{v}^d) + \boldsymbol{S}}_{\dot{\boldsymbol{\alpha}}^p} \underbrace{- \nabla \times \dot{\boldsymbol{\varepsilon}}^\theta}_{\dot{\boldsymbol{\alpha}}^\theta} \tag{1.20}$$

where $\boldsymbol{\alpha}^p$ is the dislocation density tensor, $\boldsymbol{\varepsilon}^\theta$ is the symmetric thermal strain tensor, $\boldsymbol{\alpha}^\theta$ is the "thermal quasi-dislocation" density tensor (Eq. (1.5)), and $\boldsymbol{\alpha}$ is Nye's tensor, which now

also directly carries contributions from the temperature evolution problem through $\boldsymbol{\alpha}^{\theta}$. The fully coupled problem consists of solving Eq. (1.20) alongside the mechanical equilibrium and temperature evolution equations, which stem from the three conservation laws that serve as basis for the theory: conservation of Burgers vector, linear/angular momentum, and energy. TFDM extends the capabilities of FDM by accounting for the effect of thermal strains in the stress response, as well as providing an expression for the temperature evolution, derived from the first law of thermodynamics, which includes the heat generated due to the evolution of dislocations.

1.3 Problem statement and research questions

As already stated in Upadhyay, 2020, most existing (discrete and continuum) dislocation modelling approaches assume isothermal and/or adiabatic conditions to study dislocation transport and interaction. To our knowledge, the first and only two-way coupling between the evolution of the dislocation density and the transient temperature fields was proposed in Upadhyay, 2020 within a small deformation framework. However, a numerical implementation of the theory, which would allow for an in-depth understanding of its capabilities, has not been presented yet.

Furthermore, the framework in Upadhyay, 2020 is limited to small deformations, and a comprehensive theory that incorporates the interaction between dislocation activity and temperature changes, while accommodating geometrical non-linearities, is missing. Such a framework would be highly pertinent to accurately study the evolution of dislocations in the microstructure during processes that involve submitting a body to severe thermomechanical boundary conditions, such as AM, welding, quenching, forging, etc.

The aim of this thesis is thus to develop a continuum theory in finite deformations capable of solving the initial boundary value problem of dislocation thermomechanics in the solid state, while accounting for the mutual interaction between dislocation activity (transport, annihilation, generation) and temperature evolution. The particular focus on temperatures below the solidus is motivated by recent observations in Gaudez et al., 2023 of a considerable evolution of dislocation structures in a body due to transient thermal gradients in the solid state. Furthermore, geometric linearisation of the theory will be shown to reduce to the small deformation framework in Upadhyay, 2020, and a numerical implementation of the latter constitutes another primary objective of the present work.

Therefore, the developments in this thesis will answer the following questions.

1. How could a finite deformation field dislocation thermomechanics theory be developed, based only on observable quantities?
   (a) How can the thermal effects be coupled with dislocation evolution?
   (b) What impact, if any, would this coupling have on the temperature evolution?
   (c) How to account for the partition of plastic work into heat and stored elastic energy,

expressed by the Taylor-Quinney coefficient (Taylor and Quinney, 1934)?

(d) Can the geometric linearisation of this theory be compared with the small strains framework in Upadhyay, 2020?

2. How could the theory proposed in Upadhyay, 2020 be implemented numerically?

   (a) How can this implementation be verified?

   (b) What is the profile of the temperature field generated due to the motion of an edge and a screw dislocations? What are the differences and why do they exist?

   (c) Considering dislocation lines that approach each other, what is the impact of the interaction of the stress field around their cores on the temperature evolution?

   (d) What is the temperature profile generated during the expansion of a dislocation loop? When the loop approaches a free surface, how does that impact the temperature evolution?

2 Finite deformation thermomechanical theory of field dislocations

In this chapter, a finite-deformation thermomechanical theory of field dislocations is presented. The preprint of the submitted paper can be found in Lima-Chaves et al., 2024, from which the following content is extracted.

2.1 Abstract

A geometrically nonlinear theory for field dislocation thermomechanics based entirely on measurable state variables is proposed. Instead of starting from an ordering-dependent multiplicative decomposition of the total deformation gradient tensor, the additive decomposition of the velocity gradient into elastic, plastic and thermal distortion rates is obtained as a natural consequence of the conservation of the Burgers vector. Based on this equation, the theory consistently captures the contribution of transient heterogeneous temperature fields on the evolution of the (polar) dislocation density. The governing equations of the model are obtained from the conservation of Burgers vector, mass, linear and angular momenta, and the First Law. The Second Law is used to deduce the thermodynamical driving forces for dislocation velocity. An evolution equation for temperature is obtained from the First Law and the Helmholtz free energy density, which is taken as a function of the following measurable quantities: elastic distortion, temperature and the dislocation density (the theory allows prescribing additional measurable quantities as internal state variables if needed). Furthermore, the theory allows one to compute the Taylor-Quinney factor, which is material and strain rate dependent. Accounting for the polar dislocation density as a state variable in the Helmholtz free energy of the system allows for temperature solutions in the form of dispersive waves with finite propagation speed, despite using Fourier's law of heat conduction as the constitutive assumption for the heat flux vector.

2.2 Introduction

We present a fully coupled finite-deformation thermomechanical theory of field dislocation mechanics, i.e., a theory based on partial differential equations (PDEs). The theory incorporates a two-way coupling between dislocation activity and temperature evolution, while accounting for unrestricted geometrical and material nonlinearities in a potentially anisotropic elastoplastic body. This theory is motivated by the finite deformation isothermal field dislocation mechanics theory (Acharya, 2001, Acharya, 2004) and the small-deformation thermomechanical framework of (Upadhyay, 2020). Specifically, the present theory is a generalisation of the thermomechanical theory in Acharya, 2011, by accounting for a flux term in the dislocation density evolution that allows for capturing thermal strain effects in the stress response, and of the one in Upadhyay, 2020 from a geometrical non-linearity perspective.

The motivation to develop this model arises from the need for a continuum framework in a geometrically nonlinear setting that has the minimum necessary tools to study the evolution of dislocations in bodies that undergo thermomechanical processes, such as additive manufacturing, welding, quenching, annealing, forming, forging, etc. The small deformation thermomechanical theory (Upadhyay, 2020) and its finite element implementation (Lima-Chaves and Upadhyay, 2024) have shown how dislocation activity induces the evolution of the temperature field. The need to develop a geometrically nonlinear theory became evident when simulating dislocations moving at large velocities (at a considerable fraction of the material shear wave propagation velocity) (Lima-Chaves and Upadhyay, 2024) or under rapidly evolving thermomechanical boundary conditions such as those occurring during additive manufacturing.

The proposed theory relies only on measurable (observable) fields at any given instant of time, namely, the elastic distortion, the polar dislocation density, the temperature field, and the material velocity. The theory does not require a multiplicative decomposition of the deformation gradient tensor into elastic and plastic distortions ($\boldsymbol{F} = \boldsymbol{F}^e \boldsymbol{F}^p$) in the isothermal case, as introduced by Bilby et al., 1957, Kröner, 1959, Lee, 1969, or into elastic, plastic and thermal parts in the thermomechanical case ($\boldsymbol{F} = \boldsymbol{F}^e \boldsymbol{F}^p \boldsymbol{F}^\theta$ or $\boldsymbol{F} = \boldsymbol{F}^e \boldsymbol{F}^\theta \boldsymbol{F}^p$), as considered in Zeng et al., 2022, Bammann and Solanki, 2010, Li et al., 2022, McAuliffe and Waisman, 2015, Felder et al., 2022, Grilli et al., 2022, Zhao et al., 2013, among others.

In the elastoplastic case, Clifton, 1972 discussed the equivalence between the decompositions $\boldsymbol{F} = \boldsymbol{F}^e_{(1)} \boldsymbol{F}^p_{(1)}$ ("classical") and $\boldsymbol{F} = \boldsymbol{F}^p_{(2)} \boldsymbol{F}^e_{(2)}$ ("reverse"), stating that either can be used for the analysis of finite elastic and plastic deformations of isotropic solids, the choice being a matter of convenience for the study in question. Lubarda, 1999 focused on the reverse decomposition $\boldsymbol{F} = \boldsymbol{F}^p_{(2)} \boldsymbol{F}^e_{(2)}$, and showed that for an isotropic solid, the same structure of constitutive equations is obtained as when using the classical decomposition, with $\boldsymbol{F}^e_{(1)} = \boldsymbol{F}^e_{(2)}$ if the material preserves its elastic properties during plastic deformation. More recently, Yavari and Sozio, 2023 proposed the equivalence of the classical and reverse decompositions for anisotropic solids, with the Cauchy stress computed by either being the same, "when the direct and reverse decompositions represent the same anelastic deformation." Here, in a simple example of an elastoplastic *evolution*

considering J_2 plasticity and isotropic elasticity in a purely mechanical setting, we show in Section 2.2.1 that the Cauchy stress history corresponding to a simple shear or a combined loading depends on the chosen ordering of the multiplicative decomposition. The evolution of the plastic distortion in the two cases is different, although not directly comparable, being tensors with different invariance properties.

In the context of finite deformation thermoelasticity, the multiplicative decomposition of $\boldsymbol{F}$ into elastic and thermal components ($\boldsymbol{F} = \boldsymbol{F}^e\boldsymbol{F}^\theta$) was introduced in Stojanovic et al., 1964 according to Sadik and Yavari, 2017. As in elastoplasticity theories, an intermediate configuration is introduced, which is obtained from the current configuration upon isothermal elastic unloading (Vujosevic and Lubarda, 2002). The non-uniqueness of the intermediate configuration is usually handled by considering a specific form for $\boldsymbol{F}^\theta$ according to the material to be modelled (Vujosevic and Lubarda, 2002). Within a finite deformation thermo-elastoplastic theory, if one considers a material that thermally expands isotropically, then the ordering of the plastic and thermal distortion tensors in the decomposition $\boldsymbol{F} = \boldsymbol{F}^e\boldsymbol{F}^p\boldsymbol{F}^\theta$ is irrelevant, since, in this case, $\boldsymbol{F}^\theta = \alpha(\theta)\mathbb{1}$, with $\alpha(\theta)$ being the thermal stretch ratio in an arbitrary direction (Vujosevic and Lubarda, 2002). However, in a more general case that encompasses thermal anisotropy, the factors in the multiplicative decomposition do not commute, and there is little physical guidance as to what should be chosen, with each choice having an impact on the constitutive relations of the theory.

Other researchers have also proposed finite deformation elastoplastic models that do not require the specification of a multiplicative decomposition of $\boldsymbol{F}$. Rubin and Bardella, 2023 proposed an Eulerian theory of size-dependent plasticity that does not rely on the multiplicative decomposition of $\boldsymbol{F}$, without including a detailed description of dislocation mechanics. In Acharya, 2004, a finite deformation time-dependent, isothermal dislocation mechanics theory is proposed, in which only the current configuration and a set of point-wise elastically unloaded configurations play a role in the theory, with the latter being defined through a kinematically fundamental statement of elastic incompatibility following the work of Willis, 1967 concerning dislocation statics. Following this line of work, Acharya and Zhang, 2015 show that, based on the conservation of the Burgers vector, in the isothermal case one recovers the well-accepted additive decomposition of the spatial velocity gradient into elastic and plastic parts, without the need to introduce the multiplicative decomposition $\boldsymbol{F} = \boldsymbol{F}^e\boldsymbol{F}^p$. This approach has seen significant development and validation against the experimental results in R. Arora and Acharya, 2020a, 2020b; R. Arora et al., 2020; A. Arora et al., 2022, 2023.

The novelty of our work is the development of exact kinematics for thermo-elastoplastic problems based on dislocation mechanics in a finite-deformation setting within a transient heterogeneous temperature field which does not involve a reference configuration and deformation from it, and one that leads to a dynamical model whose dissipation is invariant to superposed rigid body motions. Similarly to Upadhyay, 2020, this kinematics naturally arises from the conservation of the Burgers vector. However, the extension to finite deformations under the required 'design' constraints mentioned above is neither straightforward nor obvious; for instance, the present work differs fundamentally from Upadhyay, 2020 by only involving observable fields along the

lines of the finite deformation, thermomechanical model in Acharya, 2011, the latter, however, not incorporating the effect of thermal strains in stress response. These differences impact the evolution statement of the dislocation density in comparison to Acharya, 2011, Upadhyay, 2020, even apart from terms related to accounting for finite deformations. This difference is clearly shown in the comparison between the linearisation of the present model and the one in Upadhyay, 2020 on Section 2.6.3.

Building on the proposed kinematics and considering a constitutive assumption for the Helmholtz free energy that accounts for the (line-type) defect density in the body, the resulting structure of the PDE for temperature evolution is such that it allows for solutions in the form of dispersive temperature waves with *finite speeds of propagation*. This is despite assuming Fourier's law as the constitutive equation for the heat flux vector, which results in the instantaneous propagation of temperature throughout a domain characteristic of a linear parabolic problem. It is shown that, at least on a linear level, the obtained PDE admits solutions with well-posed growth, allowing for the onset of spatial pattern formation from the amplification of wave components of specific wavenumbers.

Our theory is well-suited for understanding the different sources of heat coming from thermomechanics and plastic work due to dislocation motion, with the latter being described by a geometrical argument of conservation of Burgers vector. The proposed framework allows us to evaluate the partition of plastic work into heat and stored energy in the material during thermomechanical processes. Understanding of this partition gained increased importance after the experiments conducted by Taylor and Quinney, 1934, which provided a measure of the latent energy stored in a material during cold work (see Bever et al., 1973 for an extensive survey on the topic). Subsequently, many studies were directed towards computing the plastic work that remained stored in the material (and converted into heat) through modelling. Different techniques have been used, among them dislocation dynamics (Benzerga et al., 2005), molecular dynamics (Kositski and Mordehai, 2021, Xiong et al., 2022, Stimac et al., 2022) and continuum approaches (Rosakis et al., 2000, Stainier and Ortiz, 2010, Dæhli et al., 2023, Longère, 2023), with the present fitting into the latter body of work.

This paper is divided as follows: Section 2.2.1 shows an example that illustrates the impact of the ordering of the elastoplastic multiplicative decomposition on the stress response of an isotropic material, which readers mainly interested in the development of the thermomechanical theory may safely skip. The kinematics based on the conservation of the Burgers vector is presented in Section 2.3. Then, the governing equations and the thermodynamical considerations of the theory are shown in Section 2.4, where the temperature evolution PDE and the partition of plastic work in the model are also discussed. A geometrical linearisation of the proposed framework is shown in Section 2.5. Considering a Saint-Venant-Kirchhoff material, a Helmholtz free energy expression is presented in Section 2.6, alongside the set of resulting equations of the model in the geometrically non-linear and linear cases, followed by a comparison with the theory developed in Upadhyay, 2020. The mathematical notation adopted in this paper can be consulted in Appendix A.

2.2.1 Ordering-dependence of the multiplicative decomposition in finite deformation elastoplasticity

The objective of this section is to study the impact of ordering on the multiplicative decomposition of the deformation gradient tensor ($\boldsymbol{F}$) into elastic ($\boldsymbol{F}^e$) and plastic ($\boldsymbol{F}^p$) distortions $\boldsymbol{F} = \boldsymbol{F}^e_{(1)}\boldsymbol{F}^p_{(1)}$ (denoted *Case 1*) or $\boldsymbol{F} = \boldsymbol{F}^p_{(2)}\boldsymbol{F}^e_{(2)}$ (denoted *Case 2*) in a simple and practical example within a purely mechanical setting, considering a given homogeneous deformation gradient history, constitutive relation for the stress response, and J_2 plasticity. More specifically, the evolution equations for $\dot{\boldsymbol{F}}^e_{(1)}$ (in *Case 1*) and $\dot{\boldsymbol{F}}^e_{(2)}$ (in *Case 2*) are solved for a given $\boldsymbol{F}(t)$ and $\boldsymbol{L}(t) = \dot{\boldsymbol{F}}\boldsymbol{F}^{-1}$, from which the Cauchy stress evolutions $\boldsymbol{\sigma}(\boldsymbol{F}^e_{(1)}(t))$ and $\boldsymbol{\sigma}(\boldsymbol{F}^e_{(2)}(t))$ are calculated and compared in simple shear and combined stretch-contraction-shear examples. The expression for $\boldsymbol{\sigma}$ is defined assuming hyperelasticity and following the frame-invariance requirements of $\boldsymbol{F}^e_{(1)}$ and $\boldsymbol{F}^e_{(2)}$. The plastic distortion rate $\boldsymbol{L}^p_{(i)}$, $i = 1,2$, is defined based on the simplest J_2 constitutive assumption and on the frame invariance requirements associated with $\mathrm{sym}(\boldsymbol{L}^p_{(i)})$. It is shown that $\boldsymbol{\sigma}(\boldsymbol{F}^e_{(1)}(t))$ and $\boldsymbol{\sigma}(\boldsymbol{F}^e_{(2)}(t))$ differ considerably in the examples considered here, so the choice of ordering in the multiplicative decomposition of $\boldsymbol{F}$ has a crucial impact on the evolution of stress in a body. As already mentioned, readers mainly interested in the theory presented in this work may skip to the end of this section.

A central tenet in this study is that any mechanical theory, and hence the ones considered here based on either of the decompositions in *Case 1* or *Case 2*, should reduce to conventional nonlinear elasticity as a limiting case. That is, considering $\boldsymbol{F}^p_{(i)} = \mathbb{1}$, $i = 1,2$, we have $\boldsymbol{F} = \boldsymbol{F}^e_{(i)}$ to recover elasticity, such that in both cases $\boldsymbol{F}^e_{(i)}$ is a two-point tensor with its co-domain being tangent spaces at points of the body in the current configuration.

The two cases are presented as follows:

Case 1: $\boldsymbol{F} = \boldsymbol{F}^e_{(1)}\boldsymbol{F}^p_{(1)}$ The spatial velocity gradient is written as

$$\begin{aligned}
&\boldsymbol{L} = \dot{\boldsymbol{F}}\boldsymbol{F}^{-1} = \left(\dot{\boldsymbol{F}}^e_{(1)}\boldsymbol{F}^p_{(1)} + \boldsymbol{F}^e_{(1)}\dot{\boldsymbol{F}}^p_{(1)}\right)\left(\boldsymbol{F}^{p-1}_{(1)}\boldsymbol{F}^{e-1}_{(1)}\right) = \dot{\boldsymbol{F}}^e_{(1)}\boldsymbol{F}^{e-1}_{(1)} + \boldsymbol{F}^e_{(1)}\dot{\boldsymbol{F}}^p_{(1)}\boldsymbol{F}^{p-1}_{(1)}\boldsymbol{F}^{e-1}_{(1)} \\
\implies &\boldsymbol{L} = \dot{\boldsymbol{F}}^e_{(1)}\boldsymbol{F}^{e-1}_{(1)} + \boldsymbol{L}^p_{(1)} \\
\implies &\dot{\boldsymbol{F}}^e_{(1)} = \left(\boldsymbol{L} - \boldsymbol{L}^p_{(1)}\right)\boldsymbol{F}^e_{(1)},
\end{aligned} \tag{2.1}$$

where we have defined $\boldsymbol{L}^p_{(1)} := \boldsymbol{F}^e_{(1)}\dot{\boldsymbol{F}}^p_{(1)}\boldsymbol{F}^{p-1}_{(1)}\boldsymbol{F}^{e-1}_{(1)}$.

Under a rigid body motion as in Eq. (B.1), $\boldsymbol{F}$ transforms as $\boldsymbol{F}^* = \boldsymbol{Q}\boldsymbol{F}$, and we have

$$\boldsymbol{F}^* = \boldsymbol{F}^{e*}_{(1)}\boldsymbol{F}^{p*}_{(1)} \implies \boldsymbol{F}^{e*}_{(1)}\boldsymbol{F}^{p*}_{(1)} = \boldsymbol{Q}\left(\boldsymbol{F}^e_{(1)}\boldsymbol{F}^p_{(1)}\right). \tag{2.2}$$

To recover elasticity, we set $\boldsymbol{F}^p_{(1)} = \mathbb{1}$ and $\boldsymbol{F}^{p*}_{(1)} = \mathbb{1}$ which implies $\boldsymbol{F} = \boldsymbol{F}^e_{(1)}$ and

$$\boldsymbol{F}^{e*}_{(1)} = \boldsymbol{Q}\boldsymbol{F}^e_{(1)}. \tag{2.3}$$

We assume that the invariance of $\boldsymbol{F}^e_{(1)}$ under a superposed rigid body motion remains the same in the elastoplastic case; then, Eqs. (2.2) and (2.3) imply

$$\boldsymbol{F}^{p*}_{(1)} = \boldsymbol{F}^{p}_{(1)}. \tag{2.4}$$

Case 2: $\boldsymbol{F} = \boldsymbol{F}^p_{(2)}\boldsymbol{F}^e_{(2)}$ The velocity gradient now reads

$$\begin{aligned} &\boldsymbol{L} = \dot{\boldsymbol{F}}\boldsymbol{F}^{-1} = \dot{\boldsymbol{F}}^p_{(2)}\boldsymbol{F}^{p-1}_{(2)} + \boldsymbol{F}^p_{(2)}\dot{\boldsymbol{F}}^e_{(2)}\boldsymbol{F}^{e-1}_{(2)}\boldsymbol{F}^{p-1}_{(2)} \\ \implies &\dot{\boldsymbol{F}}^e_{(2)} = \boldsymbol{F}^{p-1}_{(2)}\left(\boldsymbol{L} - \boldsymbol{L}^p_{(2)}\right)\boldsymbol{F}^p_{(2)}\boldsymbol{F}^e_{(2)} = \boldsymbol{F}^e_{(2)}\boldsymbol{F}^{-1}\left(\boldsymbol{L} - \boldsymbol{L}^p_{(2)}\right)\boldsymbol{F}, \end{aligned} \tag{2.5}$$

where $\boldsymbol{L}^P_{(2)} := \dot{\boldsymbol{F}}^p_{(2)}\boldsymbol{F}^{p-1}_{(2)}$.

Superposed rigid body motion in this case requires

$$\boldsymbol{F}^* = \boldsymbol{F}^{p*}_{(2)}\boldsymbol{F}^{e*}_{(2)} \implies \boldsymbol{F}^{p*}_{(2)}\boldsymbol{F}^{e*}_{(2)} = \boldsymbol{Q}\left(\boldsymbol{F}^p_{(2)}\boldsymbol{F}^e_{(2)}\right). \tag{2.6}$$

As before, to recover elasticity we set $\boldsymbol{F}^p_{(2)} = \mathbb{1}$, such that $\boldsymbol{F} = \boldsymbol{F}^e_{(2)}$ and

$$\boldsymbol{F}^* = \boldsymbol{F}^{e*}_{(2)} \implies \boldsymbol{F}^{e*}_{(2)} = \boldsymbol{Q}\boldsymbol{F}^e_{(2)}. \tag{2.7}$$

Assuming that this invariance requirement of $\boldsymbol{F}^e_{(2)}$ also applies in the elastoplastic case, Eqs. (2.6) and (2.7) gives

$$\begin{aligned} &\boldsymbol{F}^{p*}_{(2)} = \boldsymbol{Q}\left(\boldsymbol{F}^p_{(2)}\boldsymbol{F}^e_{(2)}\right)\left(\boldsymbol{F}^{e*}_{(2)}\right)^{-1} = \boldsymbol{Q}\left(\boldsymbol{F}^p_{(2)}\boldsymbol{F}^e_{(2)}\right)\boldsymbol{F}^{e-1}\boldsymbol{Q}^T \\ \implies &\boldsymbol{F}^{p*}_{(2)} = \boldsymbol{Q}\boldsymbol{F}^p_{(2)}\boldsymbol{Q}^T, \end{aligned} \tag{2.8}$$

that is, $\boldsymbol{F}^p_{(2)}$ transforms as a tensor on the current configuration under a superposed rigid body motion.

To define the Cauchy stress tensor, we consider that the stress response given by $\boldsymbol{\sigma} = \hat{\boldsymbol{\sigma}}(\boldsymbol{F}^e)$. Given that $\boldsymbol{F}^e_{(i)}$ transforms as $\boldsymbol{F}^{e*}_{(i)} = \boldsymbol{Q}\boldsymbol{F}^e_{(i)}$ under a superposed rigid body motion for $i = 1, 2$ (Eqs. (2.3) and (2.7)), the material frame indifference for the stress tensor (c.f., Truesdell et al., 2004) requires the reduced constitutive equation $\hat{\boldsymbol{\sigma}}(\boldsymbol{F}^e_{(i)}) = \boldsymbol{F}^e_{(i)}\tilde{\boldsymbol{\sigma}}(\boldsymbol{C}^e_{(i)})\boldsymbol{F}^{eT}_{(i)}$, where $\boldsymbol{C}^e_{(i)} = \boldsymbol{F}^{eT}_{(i)}\boldsymbol{F}^e_{(i)}$ is the right Cauchy-Green tensor. For this example, we choose $\tilde{\boldsymbol{\sigma}}(\boldsymbol{C}^e_{(i)}) = \mathbb{C} : \boldsymbol{E}_{(i)}$ with $\boldsymbol{E}_{(i)} = \frac{1}{2}(\boldsymbol{C}^e_{(i)} - \mathbb{1})$. Hence, we write the Cauchy stress tensor as

$$\boldsymbol{\sigma}_{(i)} = \boldsymbol{F}^e_{(i)}\left[\frac{1}{2}\mathbb{C} : \left(\boldsymbol{F}^{eT}_{(i)}\boldsymbol{F}^e_{(i)} - \mathbb{1}\right)\right]\boldsymbol{F}^{eT}_{(i)}. \tag{2.9}$$

Next, we choose an expression for $\boldsymbol{L}^p_{(i)}$ based on J_2 plasticity theory and the invariance require-

ments of $\mathrm{sym}(\boldsymbol{L}^p_{(i)})$. For a superposed rigid body motion, in *Case 1* we write Eq. (2.1) as

$$\begin{aligned}
&\mathrm{sym}(\boldsymbol{L}^*) = \mathrm{sym}\Big(\dot{\boldsymbol{F}}^{e*}_{(1)}(\boldsymbol{F}^{e*}_{(1)})^{-1}\Big) + \mathrm{sym}(\boldsymbol{L}^{p*}_{(1)}) \\
\implies &\boldsymbol{Q}\mathrm{sym}(\boldsymbol{L})\boldsymbol{Q}^T = \boldsymbol{Q}\mathrm{sym}\Big(\dot{\boldsymbol{F}}^{e}_{(1)}\boldsymbol{F}^{e-1}_{(1)}\Big)\boldsymbol{Q}^T + \mathrm{sym}(\boldsymbol{L}^{p*}_{(1)}) \\
\implies &\mathrm{sym}(\boldsymbol{L}^{p*}_{(1)}) = \boldsymbol{Q}\mathrm{sym}(\boldsymbol{L}^{p}_{(1)})\boldsymbol{Q}^T,
\end{aligned} \tag{2.10}$$

where Eq. (2.3) was used. For *Case 2* we write Eq. (2.5) as

$$\begin{aligned}
&\mathrm{sym}(\boldsymbol{L}^*) = \mathrm{sym}(\boldsymbol{L}^{p*}_{(2)}) + \mathrm{sym}\Big(\boldsymbol{F}^{p*}\dot{\boldsymbol{F}}^{e*}_{(2)}(\boldsymbol{F}^{e*}_{(2)})^{-1}(\boldsymbol{F}^{p*}_{(2)})^{-1}\Big) \\
\implies &\boldsymbol{Q}\mathrm{sym}(\boldsymbol{L})\boldsymbol{Q}^T = \mathrm{sym}(\boldsymbol{L}^{p*}_{(2)}) + \boldsymbol{Q}\mathrm{sym}\Big(\boldsymbol{F}^{p}\dot{\boldsymbol{F}}^{e}_{(2)}\boldsymbol{F}^{e-1}_{(2)}\boldsymbol{F}^{p-1}_{(2)}\Big)\boldsymbol{Q}^T \\
\implies &\mathrm{sym}(\boldsymbol{L}^{p*}_{(2)}) = \boldsymbol{Q}\mathrm{sym}(\boldsymbol{L}^{p}_{(2)})\boldsymbol{Q}^T.
\end{aligned} \tag{2.11}$$

Hence, for both *Case 1* and *Case 2* we use

$$\begin{aligned}
\boldsymbol{L}^p_{(i)} &= a_{(i)}\frac{\mathrm{dev}(\boldsymbol{\sigma}_{(i)})}{\|\mathrm{dev}(\boldsymbol{\sigma}_{(i)}\|} \\
a_{(i)} &= \hat{\gamma}_0\left(\frac{\|\mathrm{dev}(\boldsymbol{\sigma}_{(i)})\|}{\sqrt{2}g}\right)^{\frac{1}{m}},
\end{aligned} \tag{2.12}$$

where $\hat{\gamma}_0$ is the reference strain rate, g is the material strength and m is the material rate sensitivity coefficient, and $\mathrm{dev}(\boldsymbol{\sigma}) = \boldsymbol{\sigma} - \frac{1}{3}\mathrm{tr}(\boldsymbol{\sigma})\mathbb{1}$ is the stress deviator. This allows a "most" unbiased choice allowing for minimum deviations between the predictions of the two cases.

2.2.1.1 Example: simple shear

Consider a homogeneous, time-dependent deformation gradient tensor whose components with respect to an orthonormal basis $\{\hat{\boldsymbol{e}}_1, \hat{\boldsymbol{e}}_2, \hat{\boldsymbol{e}}_3\}$ are expressed in matrix form as

$$\boldsymbol{F}(t) = \begin{pmatrix} 1 & \gamma_0 t & 0 \\ 0 & 1 & 0 \\ 0 & 0 & 1 \end{pmatrix}, \tag{2.13}$$

which corresponds to a simple shear along $\hat{\boldsymbol{e}}_1 \otimes \hat{\boldsymbol{e}}_2$. The corresponding components of the velocity gradient $\boldsymbol{L} = \dot{\boldsymbol{F}}\boldsymbol{F}^{-1}$ are given by

$$\boldsymbol{L}(t) = \begin{pmatrix} 0 & \gamma_0 & 0 \\ 0 & 0 & 0 \\ 0 & 0 & 0 \end{pmatrix}. \tag{2.14}$$

The example consists of solving the evolution equations for $\dot{\boldsymbol{F}}^e_{(i)}$, $i = 1,2$ given by Eqs. (2.1) and (2.5), with $\boldsymbol{F}$ and $\boldsymbol{L}$ given by Eqs. (2.13) and (2.14), respectively, $\boldsymbol{L}^p_{(i)}$ computed by Eq. (2.12),

and $\boldsymbol{\sigma}_{(i)}$ expressed as in Eq. (2.9). The parameters used in the calculations are $E = 100$ GPa, $\nu = 0.3$, $\gamma_0 = 1\ \mathrm{s}^{-1}$, $g = 50$ MPa, $m = 0.01$. The numerical integration of Eqs. (2.1) and (2.5) is carried out up to $t_F = 1$ s, with a time step of $\Delta t = 10^{-5}$ s, resulting in a $\gamma_0 t_F = 1$ shear strain.

For this simple example, considerable differences emerge in the stress response according to the ordering of the multiplicative decomposition, as shown in Fig. 2.1. The evolutions depicted in Fig. 2.1a, d, and g cannot be directly compared, as $\boldsymbol{F}^p_{(1)}$ and $\boldsymbol{F}^p_{(2)}$ are not tensors with the same domain and co-domain. The normal Cauchy stress components σ_{11} and σ_{22} remain constant and close to zero in *Case 1*, whereas in *Case 2*, they evolve to positive and negative values, respectively, producing a significant deviation (Fig. 2.1b, c, e, and f). The shear component σ_{12} behaves differently according to the ordering, with a constant plateau after yielding in *Case 1*, and softening in *Case 2*, such that the relative difference constantly increases to reach above 40 % at $\Gamma = 1$ (Fig. 2.1h and i). Finally, $\|\mathrm{dev}(\boldsymbol{\sigma})\|$ and $\|\boldsymbol{\sigma}\|$ present a similar evolution in both cases, but with a considerable relative difference that reaches a maximum of 80 % for both (Fig. 2.1j).

2.2.1.2 Example: combined stretch, contraction and shear

In this example, we write the deformation gradient tensor components as

$$\boldsymbol{F}(t) = \begin{pmatrix} 1 + d\gamma_0 t & \gamma_0 t & 0 \\ 0 & 1 - d\gamma_0 t & 0 \\ 0 & 0 & 1 \end{pmatrix}, \tag{2.15}$$

where d is a constant factor. This deformation gradient corresponds to a combined stretch along $\hat{\boldsymbol{e}}_1$, contraction along $\hat{\boldsymbol{e}}_2$, and shear along $\hat{\boldsymbol{e}}_1 \otimes \hat{\boldsymbol{e}}_2$. The corresponding components of the velocity gradient are given by

$$\boldsymbol{L}(t) = \begin{pmatrix} \frac{d\gamma_0}{1+d\gamma_0 t} & \frac{\gamma_0}{1-(d\gamma_0 t)^2} & 0 \\ 0 & \frac{d\gamma_0}{-1+d\gamma_0 t} & 0 \\ 0 & 0 & 0 \end{pmatrix}. \tag{2.16}$$

The example consists of solving the evolution equations for $\dot{\boldsymbol{F}}^e_{(i)}$, $i = 1,2$ given by Eqs. (2.1) and (2.5), with $\boldsymbol{F}$ and $\boldsymbol{L}$ given by Eqs. (2.15) and (2.16), respectively, $\boldsymbol{L}^p_{(i)}$ computed by Eq. (2.12), and $\boldsymbol{\sigma}_{(i)}$ expressed as in Eq. (2.9). The parameters used in the calculations are $E = 100$ GPa, $\nu = 0.3$, $d = 0.05$, $\gamma_0 = 1\ \mathrm{s}^{-1}$, $g = 50$ MPa, $m = 0.01$. The numerical integration of Eqs. (2.1) and (2.5) is carried out up to $t_F = 1$ s, with a time step of $\Delta t = 10^{-5}$ s, resulting in a $\gamma_0 t_F = 100$ % strain in shear and $d\gamma_0 t_F = 5$ % strain in stretch and contraction.

In this combined loading, considerable differences also arise due to the ordering of the multiplicative decomposition. As in the previous case, the components of $\boldsymbol{F}^p$ cannot be directly compared. The normal Cauchy stress component σ_{11} is positive in the beginning due to the stretching in the $\hat{\boldsymbol{e}}_1$ direction, but becomes negative due to the combined and nonlinear interactions between the contraction and shear in the other directions. Similar behaviour is obtained for both orderings of

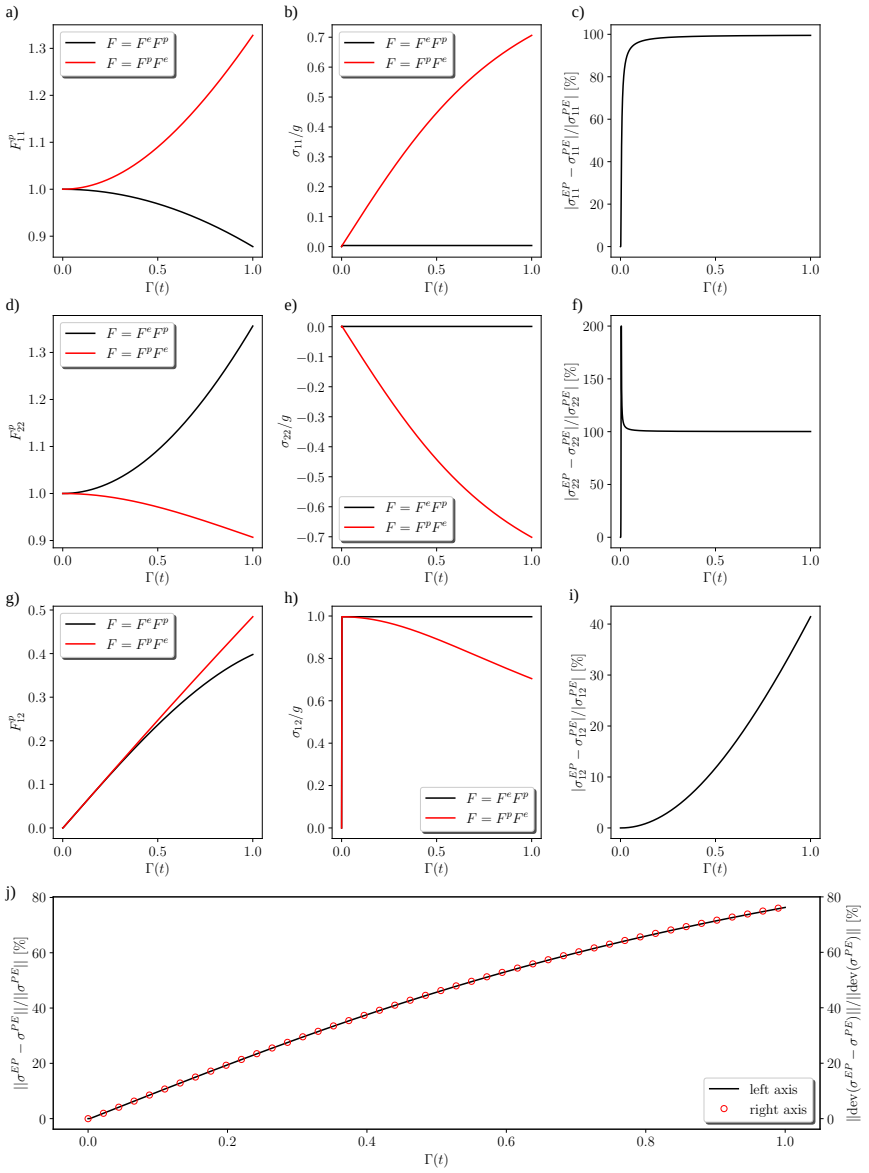

Figure 2.1: Stress and plastic distortion evolution during simple shear considering different orderings of the multiplicative decomposition of the deformation gradient tensor, plotted against $\Gamma(t) = \|\int \boldsymbol{L}\,\mathrm{d}t\|$. a), d), g): Evolution of the 11, 12 and 22 components of the plastic distortion tensor for each case; the EP and PE superscripts indicate variables resulting from the decompositions $\boldsymbol{F} = \boldsymbol{F}^e\boldsymbol{F}^p$ and $\boldsymbol{F} = \boldsymbol{F}^p\boldsymbol{F}^e$, respectively. b), e), h): Evolution of the 11, 12 and 22 components of the Cauchy stress tensor for each case, with the relative differences shown in c), f), and i). The curve in f) is capped at 200 % to suppress the large peak due to the red curve in e) crossing 0. j): Evolution of the relative differences in the Frobenius norm of the Cauchy stress deviator and full stress tensor for each case.

the multiplicative decomposition but with a considerable relative difference of around 25 % at $\Gamma = 1$ (Fig. 2.2b and c). The component σ_{22} is purely negative due to contraction along the $\hat{\boldsymbol{e}}_2$,

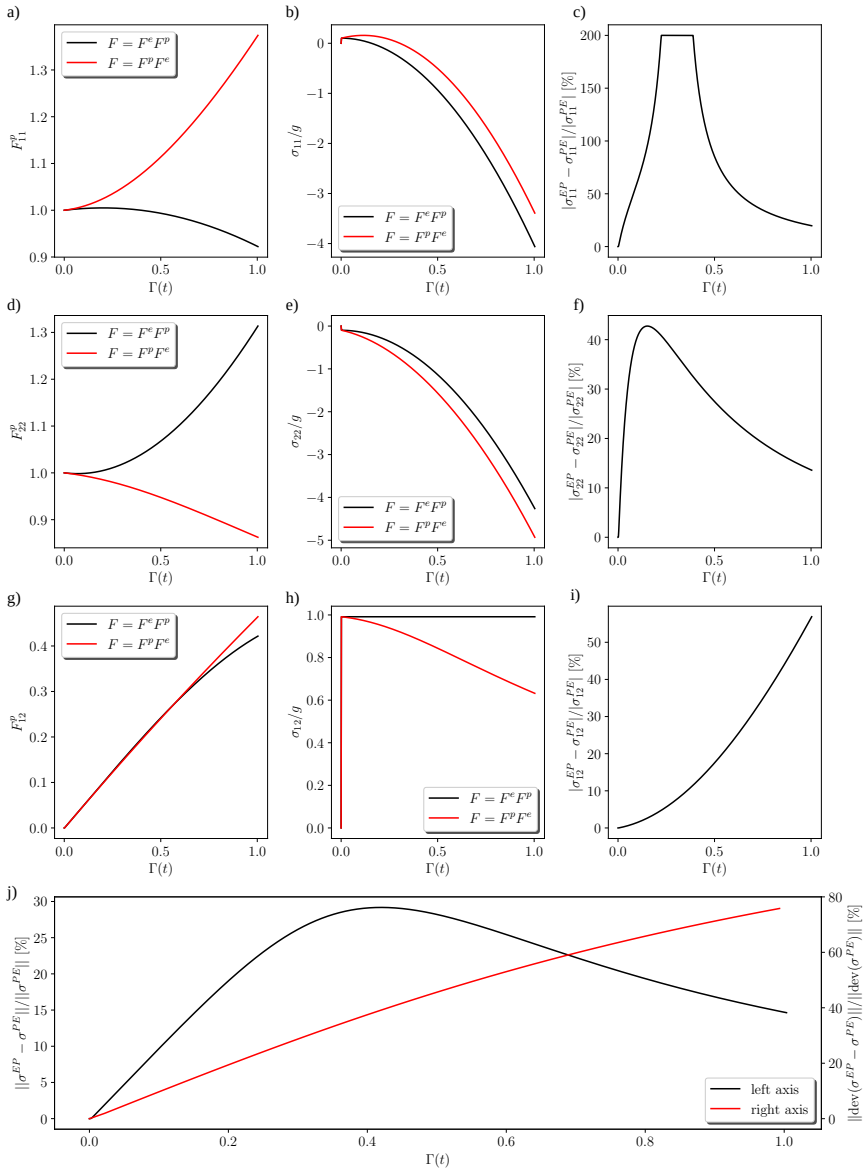

Figure 2.2: Stress and plastic distortion evolution for a combined stretch, contraction and shear considering different orderings of the multiplicative decomposition of the deformation gradient tensor, plotted against $\Gamma(t) = \|\int \boldsymbol{L}\,\mathrm{d}t\|$. a), d), g): Evolution of the 11, 12 and 22 components of the plastic distortion tensor for each case; the EP and PE superscripts indicate variables resulting from the decompositions $\boldsymbol{F} = \boldsymbol{F}^e\boldsymbol{F}^p$ and $\boldsymbol{F} = \boldsymbol{F}^p\boldsymbol{F}^e$, respectively. b), e), h): Evolution of the 11, 12 and 22 components of the Cauchy stress tensor for each case, with the relative differences shown in c), f), and i); the curve in c) is capped at 200 % to avoid having a large peak due to the red curve in b) crossing 0. j): Evolution of the relative differences in the Frobenius norm of the Cauchy stress deviator and full stress tensor for each case.

and the relative difference between the stress evolutions reaches around 40 % before decreasing to 20 % at $\Gamma = 1$ (Fig. 2.2e, f). The shear component σ_{12} presents a behaviour similar to the previous

simple shear example (Fig. 2.2h and i). Finally, $\|\mathrm{dev}(\boldsymbol{\sigma})\|$ and $\|\boldsymbol{\sigma}\|$ present a similar evolution for both orderings, but with a considerable relative difference that reaches a maximum of 80 % and 30 % in each case, respectively (Fig. 2.2j).

2.2.1.3 Summary and implications

The ordering-dependence of the decompositions becomes evident in the presence of rotation of the material, that is when shear is involved. Pure stretch/contraction simulations result in no difference in stress evolution due to the decomposition ordering. The present discussion also extends to the thermo-elastoplastic case, in which a third thermal distortion tensor $\boldsymbol{F}^{\theta}$ can be included in the multiplicative decomposition, thus yielding six possible multiplicative decompositions of the deformation gradient into elastic, plastic, and thermal components. Of course, in the thermally isotropic case, the position $\boldsymbol{F}^{\theta}$ in the multiplicative decomposition would be irrelevant, since it would be expressed as a multiple of the identity tensor. However, in the more general anisotropic case, we expect that the six possible orderings would result in even more differences in the stress response of the body.

Considering a given body in its as-received state, it is impossible to uniquely define its plastic/thermal history, its current stress state and temperature distribution being the only accessible internal variables relevant in the context of this work. Therefore, both the definition of $\boldsymbol{F}^{p}$ and $\boldsymbol{F}^{\theta}$, and the order in which they appear in the decomposition, are arbitrary. In this sense, a unique multiplicative decomposition of the deformation gradient would require assuming knowledge of the precise deformation history of the body, which is not available to us. The only deformation history that we can follow starts from the first "current" configuration, that is, the as-received body.

These are some of the reasons why in our theory we avoid relying on such decompositions, working instead on the current configuration with kinematics based on the conservation of the Burgers vector, presented in the next section, which does not require the introduction of a global reference configuration and a plastic distortion from it.

2.3 Kinematics

2.3.1 Distortion fields and configurations

Consider a body Ω that contains a distribution of dislocation lines and a temperature gradient at a given moment in time t due to some combination of constant mechanical and thermal boundary conditions, as well as internal forces and heat sources within Ω. We shall assume that the local temperature $\theta(\boldsymbol{x},t)$ is below the solidus temperature everywhere in Ω at any given instant in time, that is, Ω always remains in the solid state. These configurations of Ω parametrized by time shall be called its current configurations and is denoted as Ω_t. Next, suppose that the body, at each fixed instant of time, can be relaxed pointwise to a set (Ω_r) of local stress-free configurations

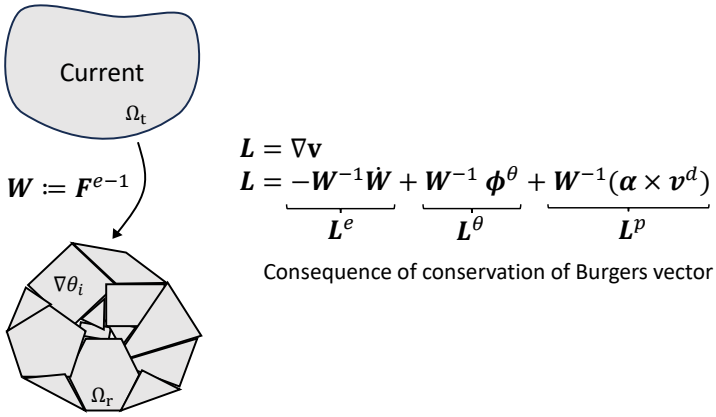

Figure 2.3: The transformation of Ω_t by $\boldsymbol{W}$, the only distortion tensor involved in this work. The $\nabla\theta_i$ represents that each polygon i is allowed to have a temperature gradient, as long as Ω_r remains stress-free. The additive decomposition of the velocity gradient into elastic, thermal and plastic parts is also shown and further discussed in Section 2.3.3.

through the inverse elastic distortion tensor $\boldsymbol{W} := \boldsymbol{F}^{e-1}$ (Fig. 2.3).

Despite not adopting the multiplicative decomposition, as shall be shown, our model yields the well-known and accepted additive decomposition of the spatial velocity gradient ($\boldsymbol{L}$) into elastic ($\boldsymbol{L}^e$), thermal ($\boldsymbol{L}^\theta$) and plastic ($\boldsymbol{L}^p$) distortion rates (see, e.g. Nemat-Nasser, 1982 and the references therein). Furthermore, and crucially, this decomposition arises as a natural consequence of the conservation of the Burgers vector. We note that one could indeed build (non-unique) plastic and thermal distortion tensors out of this information by invoking an arbitrarily fixed reference configuration; however, this consideration is merely a consequence of the theory, if so desired, and not a necessary physical element.

2.3.2 The thermomechanical line defect – a consequence of the definition of the Burgers vector

In a uniform θ field and the absence of dislocations, $\boldsymbol{W}$ is compatible (curl-free) i.e., $\nabla\times\boldsymbol{W} = 0$, in Ω_t, and could thus be represented as the gradient of a vector field (in a simply-connected domain). In the presence of dislocations and/or temperature gradients, an incompatibility might be introduced in $\boldsymbol{W}$, that is, $\nabla\times\boldsymbol{W} \neq 0$, at one or more points in the body.

If we are to draw a closed circuit (a Burgers circuit) in Ω_t and take the line integral of $\boldsymbol{W}$ over that circuit, and if this line integral is non-vanishing, then it characterises the vector topological charge (Burgers vector) carried by a line-type defect as

$$\boldsymbol{b}_r := -\oint_{c_t} \boldsymbol{W}\,\mathrm{d}\boldsymbol{x} = -\int_{s_t} (\nabla\times\boldsymbol{W})\hat{\boldsymbol{n}}\,\mathrm{d}s = \int_{s_t} \boldsymbol{\alpha}\hat{\boldsymbol{n}}\,\mathrm{d}s, \tag{2.17}$$

where c_t denotes a closed curve in Ω_t with line element $\mathbf{d}\boldsymbol{x}$, and s_t is an arbitrary surface enclosed by c_t, whose normal is $\hat{\boldsymbol{n}}$. The two-point tensor $\boldsymbol{\alpha}$ is an areal density defined as

$$\boldsymbol{\alpha} := -\nabla \times \boldsymbol{W}. \tag{2.18}$$

In regions where only dislocations contribute to the incompatibility in $\boldsymbol{W}$, $\boldsymbol{\alpha}$ and $\boldsymbol{b}$ only characterise dislocations. This association is very well known and accepted since the pioneering works of Nye, 1953, Kröner, 1958, deWit, 1960, and Mura, 1963. In fact, over the years, the definition of Burgers vector has become synonymous with the character of a dislocation.

However, the very definition of the Burgers vector in Eq. (2.17) allows one to capture the incompatibility in $\boldsymbol{W}$ irrespective of the source of that incompatibility; in the context of this work, this incompatibility could arise from either dislocations or heterogeneous θ fields or both (Kröner, 1958; Upadhyay, 2020). Furthermore, the definition of the Burgers vector makes it difficult to distinguish between the different contributors to the incompatibility of $\boldsymbol{W}$, especially in a geometrically non-linear setting. We note that this point is made from a measurement point of view (e.g. direct measurement of $\boldsymbol{W}$ or computing Burgers vectors from molecular statics simulations).

The consequences of different contributors to the incompatibility of elastic distortion were first explored by Kröner, 1958 in a small deformation stationary thermomechanics setting and later in a kinematic and dynamic setting by Upadhyay, 2020. Kröner argued that the incompatibility in $\boldsymbol{W}$ induced by a heterogeneous θ arises from a defect that also has a line-type nature. Kröner named this defect as the thermal quasi-dislocation, where "quasi" indicates that while this incompatibility is captured by the same type of areal density and vector used to characterise dislocations, it does not manifest itself as a line-type defect. However, both Kröner, 1958 and Upadhyay, 2020 relied on the definition of plastic and thermal strain tensors. This definition can be applied in the small-deformation case, where each contribution (elastic, plastic, thermal) to the strain tensor can be separately added to the total strain tensor (from a reference configuration that is necessarily introduced for geometric linearisation). In the geometrically non-linear case, the introduction of these tensors would require assuming full knowledge of the thermomechanical history of a body by introducing a global reference configuration and a plastic distortion tensor from it. In this work, the thermomechanics of field dislocations is treated in the dynamic, finite-deformation setting without such a requirement.

Following the arguments presented by Kröner, 1958, in regions where dislocations are not present but where the heterogeneous θ field induces an incompatibility in $\boldsymbol{W}$, $\boldsymbol{\alpha}$ and $\boldsymbol{b}$ can be non-vanishing. There is no evidence that a line-type thermal defect manifests itself in such situations, but non-vanishing $\boldsymbol{\alpha}$ and $\boldsymbol{b}$ do not have to arise from a line-type defect. They will be non-zero whenever $\nabla \times \boldsymbol{W} \neq 0$ is respected. As demonstrated in the small deformation setting in Upadhyay, 2020, in a domain containing a constant temperature gradient but no dislocations, constant non-zero $\boldsymbol{\alpha}$ and $\boldsymbol{b}$ are generated everywhere, and these quantities are measurable.

In the more general case, where both dislocations and heterogeneous θ field are present in the domain, $\boldsymbol{\alpha}$ and $\boldsymbol{b}$ can be non-vanishing and we assert that it is not possible to uniquely separate their contributions to the incompatibility in $\boldsymbol{W}$. In this situation, we postulate that the line defect has a thermomechanical character and henceforth we shall call it the *thermomechanical defect*, with $\boldsymbol{\alpha}$ representing its density. In the case where only dislocations contribute to incompatibility in $\boldsymbol{W}$, this thermomechanical defect manifests itself simply as a dislocation line, but not necessarily, when the dislocation lines may form dense distribution on the scale of observation. Similarly, in a dislocation-free medium with a heterogeneous θ that contributes to incompatibilities in $\boldsymbol{W}$, the thermomechanical defect does not manifest itself as a line, but has the character of the thermal defect as postulated by Kröner, 1958. This feature becomes important when dealing with the kinematics of this line defect (Section 2.3.3).

Note that in the case where only dislocations contribute to $\boldsymbol{\alpha}$ and $\boldsymbol{b}$, their magnitudes will depend on θ regardless of whether θ contributes to the incompatibility in $\boldsymbol{W}$, through the temperature dependence of the crystal lattice spacing.

2.3.3 Conservation of Burgers vector

Let the thermomechanical boundary conditions evolve with time, resulting in the motion of the thermomechanical line defect. Then, the conservation of the Burgers vector of this line defect can be written as follows (see Acharya, 2011, Appendix B for a detailed derivation):

$$\begin{aligned}\frac{\mathrm{d}}{\mathrm{d}t}\boldsymbol{b}_r &= -\frac{\mathrm{d}}{\mathrm{d}t}\oint_{c_t}\boldsymbol{W}\,\mathrm{d}\boldsymbol{x} = -\oint_{c_t}\left(\boldsymbol{\alpha}\times\boldsymbol{v}^d+\boldsymbol{\phi}^\theta\right)\mathrm{d}\boldsymbol{x}\\ &= \frac{\mathrm{d}}{\mathrm{d}t}\int_{s_t}\boldsymbol{\alpha}\hat{\boldsymbol{n}}\,\mathrm{d}s = -\int_{s_t}\nabla\times\left(\boldsymbol{\alpha}\times\boldsymbol{v}^d+\boldsymbol{\phi}^\theta\right)\hat{\boldsymbol{n}}\,\mathrm{d}s,\end{aligned} \tag{2.19}$$

where $\boldsymbol{v}^d$ is the velocity *relative to the material* of the thermomechanical defect, whose expression is constitutively prescribed guided by the condition of non-negativeness of the global thermomechanical dissipation (see Section 2.4.5). $\boldsymbol{\phi}^\theta$ represents a crucial source term that arises from the transient heterogeneous θ. The argument to support this comes from the idea proposed in the work of Kröner, 1958 and substantiated in Upadhyay, 2020. In the presence of large transient temperature gradients, the thermomechanical defect evolution can have a contribution from the incompatibility in thermal strains induced by the evolving heterogeneous temperature field, and that contribution is accounted for in $\boldsymbol{\phi}^\theta$. Alternatively, such a contribution leads to the additive decomposition of the velocity gradient into thermal and plastic parts (Eq. (2.26)), resulting, in the small deformation theory, in the familiar expression for the elastic strain rate affecting the stress rate in classical thermoelasticity. From Eq. (2.19) we obtain the following evolution statement of $\boldsymbol{\alpha}$:

$$\mathring{\boldsymbol{\alpha}} = -\nabla\times\left(\boldsymbol{\alpha}\times\boldsymbol{v}^d+\boldsymbol{\phi}^\theta\right), \tag{2.20}$$

where $\mathring{\boldsymbol{\alpha}} := \mathrm{tr}(\boldsymbol{L})\boldsymbol{\alpha} + \dot{\boldsymbol{\alpha}} - \boldsymbol{\alpha}\boldsymbol{L}^T$, is the convected derivative of $\boldsymbol{\alpha}$ (Acharya, 2001), $\boldsymbol{L} = \nabla\boldsymbol{v}$ is the velocity gradient, and $\boldsymbol{v}$ is the material velocity in Ω_t. In Eqs. (2.19) and (2.20), the term $(\boldsymbol{\alpha}\times\boldsymbol{v}^d)$ represents the flux of Burgers vector carried by thermomechanical defect lines across the curve c_t with a velocity $\boldsymbol{v}^d$ (Acharya, 2011), and $\nabla\times\boldsymbol{\phi}^\theta$ represents a source of elastic incompatibility (areal density) due to the transient heterogeneous θ in s_t.

In the small deformation case (Upadhyay, 2020), it was shown that $\boldsymbol{\phi}^\theta$ is directly related to the evolution of thermal strains as $\boldsymbol{\phi}^\theta = \partial_t\boldsymbol{\varepsilon}^\theta = \partial_t\Big[\boldsymbol{\gamma}(\theta-\theta_0)\Big]$, where ∂_t denotes the partial derivative with respect to time, $\boldsymbol{\varepsilon}^\theta$ is the thermal strain, $\boldsymbol{\gamma}$ is a positive-definite second-order tensor of thermal expansion coefficients, and θ_0 is a reference temperature value. In our work, we introduce the contribution of the incompatibility in thermal strains to the evolution of $\boldsymbol{\alpha}$ through the flux term $\nabla\times\boldsymbol{\phi}^\theta$ and define

$$\boldsymbol{\phi}^\theta = \boldsymbol{Y}\dot{\theta} \tag{2.21}$$

where $\boldsymbol{Y}$ is a two-point second-order tensor of coefficients of thermal expansion that transforms vectors from the current to the relaxed lattice state at any given point. To comply with frame invariance requirements (see Appendix B), the simplest choice for $\boldsymbol{Y}$ is

$$\boldsymbol{Y} = \boldsymbol{W}\boldsymbol{\gamma} \tag{2.22}$$

where $\boldsymbol{\gamma}$ is the second-order tensor of thermal expansion coefficients defined in Ω_t, thus being a measurable quantity on the current configuration. Frame invariance requires that, under a rigid body motion, the thermal expansion tensor transform as $\boldsymbol{\gamma}^* = \boldsymbol{Q}\boldsymbol{\gamma}\boldsymbol{Q}^T$ (see Appendix B), where $\boldsymbol{\gamma}^*$ is the rotated tensor, and $\boldsymbol{Q}$ is a proper rotation tensor. Complying with this requirement, we define

$$\boldsymbol{\gamma} = \sum_{i=1}^{3} d_i(\theta)\,\boldsymbol{l}_i\otimes\boldsymbol{l}_i \tag{2.23}$$

where $d_i(\theta)$ are the thermal expansion coefficients along the directions $\boldsymbol{l}_i$, which correspond to the eigenvectors of the left Cauchy-Green deformation tensor $\boldsymbol{B}^e = \boldsymbol{F}^e\boldsymbol{F}^{eT}$. In the thermally isotropic case, we have that $d_i(\theta) = d(\theta)$, such that $\boldsymbol{Y} = d(\theta)\boldsymbol{W}$. Therefore, we write the thermal flux $\boldsymbol{\phi}^\theta$ as

$$\boldsymbol{\phi}^\theta = \boldsymbol{W}\boldsymbol{\gamma}\dot{\theta} \tag{2.24}$$

Eq. (2.19) also imposes a specific expression for the evolution of $\boldsymbol{W}$ up to a gradient term. This gradient term is ignored as a physically motivated constitutive choice (Acharya and Zhang, 2015) for which plastic strain rate arises only where dislocations are present and a transient temperature gradient generates incompatible thermal strains. The evolution of $\boldsymbol{W}$ then is

$$\dot{\boldsymbol{W}} + \boldsymbol{W}\boldsymbol{L} = \boldsymbol{\alpha}\times\boldsymbol{v}^d + \boldsymbol{W}\boldsymbol{\gamma}\dot{\theta}. \tag{2.25}$$

By left-multiplying by $\boldsymbol{W}^{-1}$, we obtain the following additive decomposition of $\boldsymbol{L}$ as a natural consequence of the statement of conservation of topological charge Eq. (2.19):

$$\boldsymbol{L} = \underbrace{-\boldsymbol{W}^{-1}\dot{\boldsymbol{W}}}_{\boldsymbol{L}^e} + \underbrace{\boldsymbol{W}^{-1}\left(\boldsymbol{\alpha}\times\boldsymbol{v}^d\right)}_{\boldsymbol{L}^p} + \underbrace{\boldsymbol{\gamma}\dot{\theta}}_{\boldsymbol{L}^\theta}. \tag{2.26}$$

where $\boldsymbol{L}^e$, $\boldsymbol{L}^p$ and $\boldsymbol{L}^\theta$ correspond to the elastic, plastic and thermal distortion rates, respectively. Crucially, we have arrived at this result without the need to assume a multiplicative decomposition of the deformation gradient. We note here that, just like $\boldsymbol{\phi}^\theta$, other mechanisms of inelastic strain rate, such as arising from phase transformations and twinning, can be incorporated to Eq. (2.25) as an additive term $\boldsymbol{S}^i$, leading to

$$\boldsymbol{L} = \underbrace{-\boldsymbol{W}^{-1}\dot{\boldsymbol{W}}}_{\boldsymbol{L}^e} + \underbrace{\boldsymbol{W}^{-1}\left(\boldsymbol{\alpha}\times\boldsymbol{v}^d\right)}_{\boldsymbol{L}^p} + \underbrace{\boldsymbol{\gamma}\dot{\theta}}_{\boldsymbol{L}^\theta} + \underbrace{\boldsymbol{W}^{-1}\boldsymbol{S}^i}_{\boldsymbol{L}^i}. \tag{2.27}$$

provided $\boldsymbol{S}^i$ is a measurable quantity in the current configuration, with $\boldsymbol{L}^i$ being the corresponding inelastic strain rate. In the event that $\boldsymbol{S}^i$ has a non-zero curl, then it would appear in Eq. (2.20) as an additive source term with $\boldsymbol{\phi}^\theta$.

2.4 Balance laws, dissipation analysis and constitutive equations

2.4.1 Mass balance

If ρ is a space and time-dependent mass density field, then the conservation of mass statement is

$$\frac{\mathrm{d}}{\mathrm{d}t}\int_{\Omega_t}\rho\,\mathrm{d}v = 0 \quad \Rightarrow \quad \dot{\rho} + \nabla\cdot(\rho\boldsymbol{v}) = 0. \tag{2.28}$$

2.4.2 Balance of linear and angular momentum

The balance of linear momentum reads

$$\nabla\cdot\boldsymbol{\sigma} + \rho\boldsymbol{b}_f = \rho\dot{\boldsymbol{v}}, \tag{2.29}$$

where $\boldsymbol{\sigma}$ is the Cauchy stress tensor and $\boldsymbol{b}_f$ is the body force density per unit mass.

Angular momentum balance implies that the Cauchy stress tensor is symmetric i.e.,

$$\boldsymbol{\sigma} = \boldsymbol{\sigma}^T. \tag{2.30}$$

2.4.3 First law of thermodynamics

The first law of thermodynamics for the continuum thermomechanical problem is written as

$$\frac{\mathrm{d}}{\mathrm{d}t}\left(\int_{\Omega_t}\rho\varepsilon\,\mathrm{d}v+\frac{1}{2}\int_{\Omega_t}\rho\boldsymbol{v}\cdot\boldsymbol{v}\,\mathrm{d}v\right)=-\int_{\partial\Omega_t}\boldsymbol{q}\cdot\hat{\boldsymbol{n}}\,\mathrm{d}s+\int_{\partial\Omega_t}\boldsymbol{t}\cdot\boldsymbol{v}\,\mathrm{d}s+\int_{\Omega_t}\rho r\,\mathrm{d}v+\int_{\Omega_t}\rho\boldsymbol{b}_f\cdot\boldsymbol{v}\,\mathrm{d}v, \tag{2.31}$$

where ε is the internal energy density, $\boldsymbol{q}$ is the heat flux vector, $\boldsymbol{t}$ is the traction vector and ρr are internal heat sources.

Considering Cauchy's theorem, we have that $\boldsymbol{t}=\boldsymbol{\sigma}\hat{\boldsymbol{n}}$, such that using Eq. (2.29) in Eq. (2.31) and rearranging terms gives

$$\int_{\Omega_t}\rho\dot{\varepsilon}\,\mathrm{d}v=-\int_{\Omega_t}\nabla\cdot\boldsymbol{q}\,\mathrm{d}v+\int_{\Omega_t}\boldsymbol{\sigma}:\boldsymbol{L}\,\mathrm{d}v+\int_{\Omega_t}\rho r\,\mathrm{d}v. \tag{2.32}$$

In the local form, it is written as

$$\rho\dot{\varepsilon}=-\nabla\cdot\boldsymbol{q}+\boldsymbol{\sigma}:\boldsymbol{L}+\rho r. \tag{2.33}$$

2.4.4 Second law of thermodynamics

We consider the second law of thermodynamics for a continuum body as

$$\frac{\mathrm{d}}{\mathrm{d}t}\int_{\Omega_t}\rho\eta\,\mathrm{d}v\geq-\int_{\partial\Omega_t}\frac{\boldsymbol{q}}{\theta}\cdot\hat{\boldsymbol{n}}\,\mathrm{d}s+\int_{\Omega_t}\frac{\rho r}{\theta}\,\mathrm{d}v, \tag{2.34}$$

where η is the entropy density of the body. Eliminating ρr from Eq. (2.34) by using Eq. (2.33), and using the divergence theorem on the boundary term, we get

$$\int_{\Omega_t}\rho(\theta\dot{\eta}-\dot{\varepsilon})\,\mathrm{d}v-\int_{\Omega_t}\frac{1}{\theta}\boldsymbol{q}\cdot\nabla\theta\,\mathrm{d}v+\int_{\Omega_t}\boldsymbol{\sigma}:\boldsymbol{L}\,\mathrm{d}v\geq 0. \tag{2.35}$$

Then, we define the Helmholtz free energy density Ψ as

$$\Psi=\varepsilon-\eta\theta\implies\dot{\varepsilon}=\dot{\Psi}+\dot{\eta}\theta+\eta\dot{\theta}. \tag{2.36}$$

Inserting Eq. (2.36) in Eq. (2.35) gives the global dissipation inequality

$$D:=\int_{\Omega_t}\left[-\rho\left(\dot{\Psi}+\eta\dot{\theta}\right)-\frac{1}{\theta}\boldsymbol{q}\cdot\nabla\theta+\boldsymbol{\sigma}:\boldsymbol{L}\right]\mathrm{d}v\geq 0. \tag{2.37}$$

We use this form of the second law to provide guidance on the possible constitutive assumptions

that guarantee non-negative dissipation.

2.4.5 Helmholtz free energy density and constitutive relations

Let us assume that the Helmholtz free energy is a function of the state variables $(\boldsymbol{W}, \theta, \boldsymbol{\alpha})$ such that $\Psi \equiv \Psi(\boldsymbol{W}, \theta, \boldsymbol{\alpha})$. Then

$$\dot{\Psi} = \partial_{\boldsymbol{W}}\Psi : \dot{\boldsymbol{W}} + \partial_\theta \Psi \dot{\theta} + \partial_{\boldsymbol{\alpha}}\Psi : \dot{\boldsymbol{\alpha}}. \tag{2.38}$$

Next, substitute Eq. (2.25) for $\dot{\boldsymbol{W}}$ and plug Eq. (2.38) into Eq. (2.37) to arrive at

$$\begin{aligned} D = &\int_{\Omega_t} \left(\boldsymbol{\sigma} : \boldsymbol{L} - \frac{1}{\theta}\boldsymbol{q}\cdot\nabla\theta\right) \mathrm{d}v + \int_{\Omega_t} \rho \boldsymbol{W}^T \partial_{\boldsymbol{W}}\Psi : \boldsymbol{L}\, \mathrm{d}v - \int_{\Omega_t} \rho \partial_{\boldsymbol{W}}\Psi : \left(\boldsymbol{\alpha}\times\boldsymbol{v}^d + \boldsymbol{W}\boldsymbol{\gamma}\dot{\theta}\right) \mathrm{d}v \\ &- \int_{\Omega_t} \rho \partial_{\boldsymbol{\alpha}}\Psi : \left[-\mathrm{tr}(\boldsymbol{L})\boldsymbol{\alpha} + \boldsymbol{\alpha}\boldsymbol{L}^T - \nabla\times\left(\boldsymbol{\alpha}\times\boldsymbol{v}^d + \boldsymbol{W}\boldsymbol{\gamma}\dot{\theta}\right)\right] \mathrm{d}v - \int_{\Omega_t} \rho\Big(\partial_\theta\Psi + \eta\Big)\dot{\theta}\, \mathrm{d}v \geq 0, \end{aligned} \tag{2.39}$$

where Eq. (2.20) was used for $\dot{\boldsymbol{\alpha}}$. After rearranging the terms, we get (see Appendix F)

$$\begin{aligned} D = &\int_{\Omega_t} \left[\boldsymbol{\sigma} + \mathrm{sym}(\rho\boldsymbol{W}^T\partial_{\boldsymbol{W}}\Psi - \rho(\partial_{\boldsymbol{\alpha}}\Psi)^T\boldsymbol{\alpha} + \rho(\partial_{\boldsymbol{\alpha}}\Psi : \boldsymbol{\alpha})\mathbb{1})\right] : \mathrm{sym}(\boldsymbol{L})\, \mathrm{d}v \\ &+ \int_{\Omega_t} \mathrm{skew}(\rho\boldsymbol{W}^T\partial_{\boldsymbol{W}}\Psi - \rho(\partial_{\boldsymbol{\alpha}}\Psi)^T\boldsymbol{\alpha} + \rho(\partial_{\boldsymbol{\alpha}}\Psi : \boldsymbol{\alpha})\mathbb{1}) : \mathrm{skew}(\boldsymbol{L})\, \mathrm{d}v \\ &- \int_{\Omega_t} \left[\rho\eta + \rho\partial_\theta\Psi + \left(\rho\partial_{\boldsymbol{W}}\Psi - \nabla\times\rho\partial_{\boldsymbol{\alpha}}\Psi\right) : \boldsymbol{W}\boldsymbol{\gamma}\right]\dot{\theta}\, \mathrm{d}v \\ &- \int_{\Omega_t} \left\{\left[(\rho\partial_{\boldsymbol{W}}\Psi - \nabla\times\rho\partial_{\boldsymbol{\alpha}}\Psi)^T\boldsymbol{\alpha}\right] : \mathbf{X}\right\}\cdot\boldsymbol{v}^d\, \mathrm{d}v \\ &- \int_{\Omega_t} \frac{1}{\theta}\boldsymbol{q}\cdot\nabla\theta\, \mathrm{d}v \\ &- \int_{\partial\Omega_t} \rho\partial_{\boldsymbol{\alpha}}\Psi : \left[\left(\boldsymbol{\alpha}\times\boldsymbol{v}^d + \boldsymbol{W}\boldsymbol{\gamma}\dot{\theta}\right)\times\hat{\boldsymbol{n}}\right]\, \mathrm{d}s \geq 0. \end{aligned} \tag{2.40}$$

where we have considered the balance of angular momentum (Eq. (2.30)). Since $\mathrm{skew}(\boldsymbol{L})$ is related to a rigid rotation of the body, the second integral in Eq. (2.40) would indicate a dissipation associated with this rigid motion. Hence, the objectivity of dissipation requires this integral to vanish, which is shown to be the case in Appendix C as a stringent test of the statements of kinematic evolution of the theory. Thus, the second term in Eq. (2.40) vanishes.

Now, consider a motion where dislocations do not move relative to the material, i.e., $\boldsymbol{v}^d = 0$, and θ remains uniform and constant in Ω_t. Such a process should not result in any dissipation, and

this is only possible if the following constitutive relationship is assumed for the Cauchy stress:

$$\boldsymbol{\sigma} = -\rho \boldsymbol{W}^T \partial_{\boldsymbol{W}} \Psi + \rho (\partial_{\boldsymbol{\alpha}} \Psi)^T \boldsymbol{\alpha} - \rho (\partial_{\boldsymbol{\alpha}} \Psi : \boldsymbol{\alpha}) \mathbb{1} \tag{2.41}$$

Eq. (2.41) is a nonclassical form of a hyperelastic law (Chaboche, 1993), with $-\rho \boldsymbol{W}^T \partial_{\boldsymbol{W}} \Psi$ the hyperelastic part of $\boldsymbol{\sigma}$, and the two last terms being a direct consequence of the geometrical non-linearity and the chosen dependence of Ψ on $\boldsymbol{\alpha}$. Indeed, considering the expression for $\mathring{\boldsymbol{\alpha}}$ in Eq. (2.20), a reversible process (e.g., a quasi-static elastic loading with negligible temperature changes) would produce an instantaneous change in $\boldsymbol{\alpha}$ through the terms in $\boldsymbol{L}$ (which are present only in the finite strain case and required for the Burgers vector conservation), as also shown in R. Arora et al., 2020, thus requiring the presence of the last two terms in $\boldsymbol{\sigma}$ to ensure no dissipation during such process. The validity of Eq. (2.41) as a constitutive statement for $\boldsymbol{\sigma}$ with respect to the balance of angular momentum is discussed in Appendix C. With the expression in Eq. (2.41) for the Cauchy stress, the first term in Eq. (2.40) vanishes.

Next, we consider the case where no mechanical loading is applied, the dislocations are not moving, and the body temperature is uniform but can undergo homogeneous heating/cooling. In this situation, the only remaining term in the dissipation inequality Eq. (2.40) is the third term involving entropy η. Since $\dot{\theta}$ can be arbitrary in this case, the term in square brackets is set to zero to ensure non-negative dissipation, which yields

$$\eta = -\partial_\theta \Psi - \left(\partial_{\boldsymbol{W}} \Psi - \frac{1}{\rho} \nabla \times \rho \partial_{\boldsymbol{\alpha}} \Psi \right) : \boldsymbol{W} \boldsymbol{\gamma}. \tag{2.42}$$

Note that the second term in Eq. (2.42) is a direct consequence of considering the contribution of the incompatibility induced by the transient heterogeneous θ as a source term in the thermomechanical defect density evolution (Eq. (2.20)). With these relationships, the dissipation inequality is reduced to

$$\begin{aligned} D = &\int_{\Omega_t} \left\{ \left[(-\rho \partial_{\boldsymbol{W}} \Psi + \nabla \times \rho \partial_{\boldsymbol{\alpha}} \Psi)^T \boldsymbol{\alpha} \right] : \mathbf{X} \right\} \cdot \boldsymbol{v}^d \, \mathrm{d}v - \int_{\Omega_t} \frac{1}{\theta} \boldsymbol{q} \cdot \nabla \theta \, \mathrm{d}v \\ &- \int_{\partial \Omega_t} \rho \partial_{\boldsymbol{\alpha}} \Psi : \left[\left(\boldsymbol{\alpha} \times \boldsymbol{v}^d + \boldsymbol{W} \boldsymbol{\gamma} \dot{\theta} \right) \times \hat{\boldsymbol{n}} \right] \, \mathrm{d}s \geq 0. \end{aligned} \tag{2.43}$$

To ensure the non-negativeness of the heat flux term, we consider the generalized Fourier's law of heat conduction

$$\boldsymbol{q} := -\boldsymbol{K} \nabla \theta, \tag{2.44}$$

where $\boldsymbol{K}$ is the positive definite second-order thermal heat conductivity tensor which, in the general case, could be θ and/or $\boldsymbol{W}$-dependent. We assume that the driving force $\boldsymbol{f}_v$ for the

dislocation velocity takes the form

$$\boldsymbol{f}_{\upsilon} = \left[(-\rho\partial_{\boldsymbol{W}}\Psi + \nabla\times\rho\partial_{\boldsymbol{\alpha}}\Psi)^{T}\,\boldsymbol{\alpha}\right] : \mathbf{X}. \tag{2.45}$$

In the specific case of a single dislocation line and neglecting the dependence of Ψ in $\boldsymbol{\alpha}$, Eq. (2.45) reduces to the form of the well-known Peach-Koehler force acting on the dislocation line (Peach and Koehler, 1950).

Note that, in Eq. (2.43), we neglect the contribution of the boundary term to the enforcement of non-negative entropy production in the body. With these considerations, the global dissipation of the model is written as

$$D = \int_{\Omega_t} \boldsymbol{f}_{\upsilon}\cdot\boldsymbol{v}^{d}\,\mathrm{d}\upsilon - \int_{\Omega_t}\frac{1}{\theta}\boldsymbol{q}\cdot\nabla\theta\,\mathrm{d}\upsilon. \tag{2.46}$$

This enables us to consider a simple kinetic assumption on the dislocation velocity expression that ensures the non-negativeness of D such as

$$\boldsymbol{v}^{d} = \frac{1}{B}\boldsymbol{f}_{\upsilon}, \quad B>0, \tag{2.47}$$

where B is a material parameter corresponding to the dislocation drag coefficient.

2.4.6 Temperature evolution

Inserting the rate form of the Legendre transform Eq. (2.36) into Eq. (2.33) for $\dot{\varepsilon}$, and using Eqs. (2.38) and (2.42) for $\dot{\Psi}$, and η, respectively, gives

$$\rho\left[\partial_{\boldsymbol{W}}\Psi : \dot{\boldsymbol{W}} + \partial_{\boldsymbol{\alpha}}\Psi : \dot{\boldsymbol{\alpha}} - \dot{\theta}\left(\partial_{\boldsymbol{W}}\Psi - \frac{1}{\rho}\nabla\times\rho\partial_{\boldsymbol{\alpha}}\Psi\right) : \boldsymbol{W}\boldsymbol{\gamma} + \theta\dot{\eta}\right] = -\nabla\cdot\boldsymbol{q} + \boldsymbol{\sigma} : \boldsymbol{L} + \rho r. \tag{2.48}$$

Next, taking the material time derivative of Eq. (2.42), we have

$$\begin{aligned}\dot{\eta} &= -\overline{\dot{\partial_{\theta}\Psi}} - \overline{\left(\partial_{\boldsymbol{W}}\Psi - \frac{1}{\rho}\nabla\times\rho\partial_{\boldsymbol{\alpha}}\Psi\right) : \boldsymbol{W}\boldsymbol{\gamma}}^{\cdot} \\ &= -\partial^{2}_{\theta\boldsymbol{W}}\Psi : \dot{\boldsymbol{W}} - \partial^{2}_{\theta\theta}\Psi\dot{\theta} - \partial^{2}_{\theta\boldsymbol{\alpha}}\Psi : \dot{\boldsymbol{\alpha}} - \left[\partial^{2}_{\boldsymbol{W}\boldsymbol{W}}\Psi : \dot{\boldsymbol{W}} + \partial^{2}_{\boldsymbol{W}\theta}\Psi\dot{\theta} + \partial^{2}_{\boldsymbol{W}\boldsymbol{\alpha}}\Psi : \dot{\boldsymbol{\alpha}}\right. \\ &\qquad \left. + \frac{\dot{\rho}}{\rho^{2}}\nabla\times\rho\partial_{\boldsymbol{\alpha}}\Psi - \frac{1}{\rho}\overline{\nabla\times(\rho\partial_{\boldsymbol{\alpha}}\Psi)}^{\cdot}\right] : \boldsymbol{W}\boldsymbol{\gamma} - \left(\partial_{\boldsymbol{W}}\Psi - \frac{1}{\rho}\nabla\times\rho\partial_{\boldsymbol{\alpha}}\Psi\right) : \overline{\dot{\boldsymbol{W}\boldsymbol{\gamma}}}.\end{aligned} \tag{2.49}$$

Consider a tensor field $\boldsymbol{A}(\boldsymbol{x},t)$, and an arbitrary reference configuration Ω_0 (e.g. the as-received body), with $\boldsymbol{x}_0 \in \Omega_0$ denoting the position vector in Ω_0. Then, we have

$$\dot{\overline{\frac{\partial \boldsymbol{A}}{\partial \boldsymbol{x}}}} = \dot{\overline{\frac{\partial \boldsymbol{A}}{\partial \boldsymbol{x}_0}\frac{\partial \boldsymbol{x}_0}{\partial \boldsymbol{x}}}} = \frac{\partial \dot{\boldsymbol{A}}}{\partial \boldsymbol{x}_0}\boldsymbol{F}^{-1} + \frac{\partial \boldsymbol{A}}{\partial \boldsymbol{x}_0}\dot{\overline{\boldsymbol{F}^{-1}}}. \tag{2.50}$$

Now,

$$\boldsymbol{F}\boldsymbol{F}^{-1} = \mathbb{1} \implies \boldsymbol{F}\dot{\overline{\boldsymbol{F}^{-1}}} = -\dot{\boldsymbol{F}}\boldsymbol{F}^{-1} \implies \dot{\overline{\boldsymbol{F}^{-1}}} = -\boldsymbol{F}^{-1}\boldsymbol{L}, \tag{2.51}$$

such that, by inserting into Eq. (2.50), we have

$$\dot{\overline{\frac{\partial \boldsymbol{A}}{\partial \boldsymbol{x}}}} = \frac{\partial \dot{\boldsymbol{A}}}{\partial \boldsymbol{x}} - \frac{\partial \boldsymbol{A}}{\partial \boldsymbol{x}}\boldsymbol{L}. \tag{2.52}$$

With that, we can write

$$\begin{aligned} &\left[\dot{\overline{\nabla \times \boldsymbol{A}}}\right]_{ij} = \epsilon_{jkl}\dot{\overline{A_{il,k}}} = \epsilon_{jkl}(\dot{A}_{il,k} - A_{il,m}L_{mk}) = \epsilon_{jkl}\dot{A}_{il,k} + A_{il,m}L_{mk}\epsilon_{jlk} \\ &\implies \dot{\overline{\nabla \times \boldsymbol{A}}} = \nabla \times \dot{\boldsymbol{A}} + [(\nabla \boldsymbol{A})\boldsymbol{L}] : \mathbf{X} \end{aligned} \tag{2.53}$$

such that the second term in the last line of Eq. (2.49) becomes

$$\dot{\overline{\nabla \times (\rho \partial_{\boldsymbol{\alpha}} \Psi)}} = \nabla \times \left(\dot{\rho}\partial_{\boldsymbol{\alpha}}\Psi + \rho\partial^2_{\boldsymbol{\alpha}\boldsymbol{W}}\Psi : \dot{\boldsymbol{W}} + \rho\partial^2_{\boldsymbol{\alpha}\theta}\Psi\dot{\theta} + \rho\partial^2_{\boldsymbol{\alpha}\boldsymbol{\alpha}}\Psi : \dot{\boldsymbol{\alpha}}\right) + \left[\nabla(\rho\partial_{\boldsymbol{\alpha}}\Psi)\boldsymbol{L}\right] : \mathbf{X} \tag{2.54}$$

and Eq. (2.49) can be written as

$$\begin{aligned} \dot{\eta} = -\partial^2_{\theta\boldsymbol{W}}\Psi : \dot{\boldsymbol{W}} - \partial^2_{\theta\theta}\Psi\dot{\theta} - \partial^2_{\theta\boldsymbol{\alpha}}\Psi : \dot{\boldsymbol{\alpha}} - \Bigg[&\partial^2_{\boldsymbol{W}\boldsymbol{W}}\Psi : \dot{\boldsymbol{W}} + \partial^2_{\boldsymbol{W}\theta}\Psi\dot{\theta} + \partial^2_{\boldsymbol{W}\boldsymbol{\alpha}}\Psi : \dot{\boldsymbol{\alpha}} \\ &+ \frac{\dot{\rho}}{\rho^2}\nabla \times \rho\partial_{\boldsymbol{\alpha}}\Psi - \frac{1}{\rho}\nabla \times \left(\dot{\rho}\partial_{\boldsymbol{\alpha}}\Psi + \rho\partial^2_{\boldsymbol{\alpha}\boldsymbol{W}}\Psi : \dot{\boldsymbol{W}} + \rho\partial^2_{\boldsymbol{\alpha}\theta}\Psi\dot{\theta} + \rho\partial^2_{\boldsymbol{\alpha}\boldsymbol{\alpha}}\Psi : \dot{\boldsymbol{\alpha}}\right) \\ &- \frac{1}{\rho}(\nabla(\rho\partial_{\boldsymbol{\alpha}}\Psi)\boldsymbol{L}) : \mathbf{X}\Bigg] : \boldsymbol{W}\boldsymbol{\gamma} - \left(\partial_{\boldsymbol{W}}\Psi - \frac{1}{\rho}\nabla \times \rho\partial_{\boldsymbol{\alpha}}\Psi\right) : \dot{\overline{\boldsymbol{W}\boldsymbol{\gamma}}}. \end{aligned} \tag{2.55}$$

Inserting Eq. (2.55) in Eq. (2.48) and using Eq. $(2.41)_1$ for $\boldsymbol{\sigma}$ gives

$$\begin{aligned}
&\rho\partial_{\boldsymbol{W}}\Psi : \dot{\boldsymbol{W}} + \rho\partial_{\boldsymbol{\alpha}}\Psi : \dot{\boldsymbol{\alpha}} - \rho\dot{\theta}\left(\partial_{\boldsymbol{W}}\Psi - \frac{1}{\rho}\nabla\times\rho\partial_{\boldsymbol{\alpha}}\Psi\right) : \boldsymbol{W}\boldsymbol{\gamma} + \rho\theta\Bigg\{ - \partial^2_{\theta\boldsymbol{W}}\Psi : \dot{\boldsymbol{W}} - \partial^2_{\theta\theta}\Psi\dot{\theta} \\
&\quad - \partial^2_{\theta\boldsymbol{\alpha}}\Psi : \dot{\boldsymbol{\alpha}} - \Bigg[\partial^2_{\boldsymbol{W}\boldsymbol{W}}\Psi : \dot{\boldsymbol{W}} + \partial^2_{\boldsymbol{W}\theta}\Psi\dot{\theta} + \partial^2_{\boldsymbol{W}\boldsymbol{\alpha}}\Psi : \dot{\boldsymbol{\alpha}} + \frac{\dot{\rho}}{\rho^2}\nabla\times\rho\partial_{\boldsymbol{\alpha}}\Psi \\
&\quad - \frac{1}{\rho}\nabla\times\left(\dot{\rho}\partial_{\boldsymbol{\alpha}}\Psi + \rho\partial^2_{\boldsymbol{\alpha}\boldsymbol{W}}\Psi : \dot{\boldsymbol{W}} + \rho\partial^2_{\boldsymbol{\alpha}\theta}\Psi\dot{\theta} + \rho\partial^2_{\boldsymbol{\alpha}\boldsymbol{\alpha}}\Psi : \dot{\boldsymbol{\alpha}}\right) - \frac{1}{\rho}(\nabla(\rho\partial_{\boldsymbol{\alpha}}\Psi)\boldsymbol{L}) : \mathbf{X}\Bigg] : \boldsymbol{W}\boldsymbol{\gamma} \\
&\quad - \left(\partial_{\boldsymbol{W}}\Psi - \frac{1}{\rho}\nabla\times\rho\partial_{\boldsymbol{\alpha}}\Psi\right) : \dot{\overline{\boldsymbol{W}\boldsymbol{\gamma}}}\Bigg\} = -\nabla\cdot\boldsymbol{q} - \rho\partial_{\boldsymbol{W}}\Psi : \boldsymbol{W}\boldsymbol{L} + \rho\partial_{\boldsymbol{\alpha}}\Psi : \left(\boldsymbol{\alpha}\boldsymbol{L}^T - \mathrm{tr}(\boldsymbol{L})\boldsymbol{\alpha}\right) + \rho r
\end{aligned} \tag{2.56}$$

Rearrange terms

$$\begin{aligned}
&\Big[\Big(-\rho\partial_{\boldsymbol{W}}\Psi + \nabla\times\rho\partial_{\boldsymbol{\alpha}}\Psi - \rho\theta\partial^2_{\boldsymbol{W}\theta}\Psi\Big) : \boldsymbol{W}\boldsymbol{\gamma} - \rho\theta\partial^2_{\theta\theta}\Psi\Big]\dot{\theta} + \theta\nabla\times\left(\rho\partial^2_{\boldsymbol{\alpha}\theta}\Psi\dot{\theta}\right) : \boldsymbol{W}\boldsymbol{\gamma} \\
&\quad = -\rho\partial_{\boldsymbol{W}}\Psi : \left(\dot{\boldsymbol{W}} + \boldsymbol{W}\boldsymbol{L}\right) - \rho\partial_{\boldsymbol{\alpha}}\Psi : \left(\dot{\boldsymbol{\alpha}} + \mathrm{tr}(\boldsymbol{L})\boldsymbol{\alpha} - \boldsymbol{\alpha}\boldsymbol{L}^T\right) + \rho\theta\partial^2_{\theta\boldsymbol{W}}\Psi : \dot{\boldsymbol{W}} + \rho\theta\partial^2_{\theta\boldsymbol{\alpha}}\Psi : \dot{\boldsymbol{\alpha}} \\
&\qquad + \rho\theta\Bigg[\partial^2_{\boldsymbol{W}\boldsymbol{W}}\Psi : \dot{\boldsymbol{W}} + \partial^2_{\boldsymbol{W}\boldsymbol{\alpha}}\Psi : \dot{\boldsymbol{\alpha}} + \frac{\dot{\rho}}{\rho^2}\nabla\times\rho\partial_{\boldsymbol{\alpha}}\Psi - \frac{1}{\rho}\nabla\times\Big(\dot{\rho}\partial_{\boldsymbol{\alpha}}\Psi + \rho\partial^2_{\boldsymbol{\alpha}\boldsymbol{W}}\Psi : \dot{\boldsymbol{W}} \\
&\qquad\quad + \rho\partial^2_{\boldsymbol{\alpha}\boldsymbol{\alpha}}\Psi : \dot{\boldsymbol{\alpha}}\Big) - \frac{1}{\rho}(\nabla(\rho\partial_{\boldsymbol{\alpha}}\Psi)\boldsymbol{L}) : \mathbf{X}\Bigg] : \boldsymbol{W}\boldsymbol{\gamma} - \nabla\cdot\boldsymbol{q} + \rho r \\
&\qquad + \theta(\rho\partial_{\boldsymbol{W}}\Psi - \nabla\times\rho\partial_{\boldsymbol{\alpha}}\Psi) : \left(\dot{\boldsymbol{W}}\boldsymbol{\gamma} + \boldsymbol{W}\mathbb{G} : \dot{\boldsymbol{W}}\right),
\end{aligned} \tag{2.57}$$

where we consider

$$\dot{\boldsymbol{\gamma}} = \frac{\partial\boldsymbol{\gamma}}{\partial\boldsymbol{B}^e} : \frac{\partial\boldsymbol{B}^e}{\partial\boldsymbol{W}} : \dot{\boldsymbol{W}} = \mathbb{G} : \dot{\boldsymbol{W}}. \tag{2.58}$$

Use Eqs. (2.20) and (2.25) on the first and second terms of the right-hand side, respectively, to get

$$\begin{aligned}
&\Big[\Big(-\rho\partial_{\boldsymbol{W}}\Psi+\nabla\times\rho\partial_{\boldsymbol{\alpha}}\Psi-\rho\theta\partial^2_{\boldsymbol{W}\theta}\Psi\Big):\boldsymbol{W}\boldsymbol{\gamma}-\rho\theta\partial^2_{\theta\theta}\Psi\Big]\dot\theta+\theta\nabla\times\big(\rho\partial^2_{\boldsymbol{\alpha}\theta}\Psi\dot\theta\big):\boldsymbol{W}\boldsymbol{\gamma}\\
&\quad=-\rho\partial_{\boldsymbol{W}}\Psi:\big(\boldsymbol{\alpha}\times\boldsymbol{v}^d+\boldsymbol{W}\boldsymbol{\gamma}\dot\theta\big)+\rho\partial_{\boldsymbol{\alpha}}\Psi:\nabla\times\big(\boldsymbol{\alpha}\times\boldsymbol{v}^d+\boldsymbol{W}\boldsymbol{\gamma}\dot\theta\big)+\rho\theta\partial^2_{\theta\boldsymbol{W}}\Psi:\dot{\boldsymbol{W}}\\
&\qquad+\rho\theta\partial^2_{\theta\boldsymbol{\alpha}}\Psi:\dot{\boldsymbol{\alpha}}+\rho\theta\Bigg[\partial^2_{\boldsymbol{W}\boldsymbol{W}}\Psi:\dot{\boldsymbol{W}}+\partial^2_{\boldsymbol{W}\boldsymbol{\alpha}}\Psi:\dot{\boldsymbol{\alpha}}+\frac{\dot\rho}{\rho^2}\nabla\times\rho\partial_{\boldsymbol{\alpha}}\Psi-\frac{1}{\rho}\nabla\times\Big(\dot\rho\partial_{\boldsymbol{\alpha}}\Psi\\
&\qquad+\rho\partial^2_{\boldsymbol{\alpha}\boldsymbol{W}}\Psi:\dot{\boldsymbol{W}}+\rho\partial^2_{\boldsymbol{\alpha}\boldsymbol{\alpha}}\Psi:\dot{\boldsymbol{\alpha}}\Big)-\frac{1}{\rho}(\nabla(\rho\partial_{\boldsymbol{\alpha}}\Psi)\boldsymbol{L}):\mathbf{X}\Bigg]:\boldsymbol{W}\boldsymbol{\gamma}-\nabla\cdot\boldsymbol{q}+\rho r\\
&\qquad+\theta\big[\rho\partial_{\boldsymbol{W}}\Psi\boldsymbol{\gamma}^T-\nabla\times(\rho\partial_{\boldsymbol{\alpha}}\Psi)\boldsymbol{\gamma}^T+(\rho\partial_{\boldsymbol{W}}\Psi-\nabla\times\rho\partial_{\boldsymbol{\alpha}}\Psi):\boldsymbol{W}\mathbb{G}\big]:\dot{\boldsymbol{W}}.
\end{aligned}\tag{2.59}$$

Cancel out and rearrange terms

$$\begin{aligned}
&\Big[\Big(\nabla\times\rho\partial_{\boldsymbol{\alpha}}\Psi-\rho\theta\partial^2_{\boldsymbol{W}\theta}\Psi\Big):\boldsymbol{W}\boldsymbol{\gamma}-\rho\theta\partial^2_{\theta\theta}\Psi\Big]\dot\theta+\theta\nabla\times\big(\rho\partial^2_{\boldsymbol{\alpha}\theta}\Psi\dot\theta\big):\boldsymbol{W}\boldsymbol{\gamma}-\rho\partial_{\boldsymbol{\alpha}}\Psi:\nabla\times\big(\boldsymbol{W}\boldsymbol{\gamma}\dot\theta\big)\\
&\quad=-\rho\partial_{\boldsymbol{W}}\Psi:\big(\boldsymbol{\alpha}\times\boldsymbol{v}^d\big)+\rho\partial_{\boldsymbol{\alpha}}\Psi:\nabla\times\big(\boldsymbol{\alpha}\times\boldsymbol{v}^d\big)+\rho\theta\big(\partial^2_{\theta\boldsymbol{W}}\Psi+\boldsymbol{W}\boldsymbol{\gamma}:\partial^2_{\boldsymbol{W}\boldsymbol{W}}\Psi\big):\dot{\boldsymbol{W}}\\
&\qquad+\rho\theta\big(\partial^2_{\theta\boldsymbol{\alpha}}\Psi+\boldsymbol{W}\boldsymbol{\gamma}:\partial^2_{\boldsymbol{W}\boldsymbol{\alpha}}\Psi\big):\dot{\boldsymbol{\alpha}}+\Bigg[\frac{\theta\dot\rho}{\rho}\nabla\times\rho\partial_{\boldsymbol{\alpha}}\Psi-\theta\nabla\times\Big(\dot\rho\partial_{\boldsymbol{\alpha}}\Psi\\
&\qquad+\rho\partial^2_{\boldsymbol{\alpha}\boldsymbol{W}}\Psi:\dot{\boldsymbol{W}}+\rho\partial^2_{\boldsymbol{\alpha}\boldsymbol{\alpha}}\Psi:\dot{\boldsymbol{\alpha}}\Big)-\theta(\nabla(\rho\partial_{\boldsymbol{\alpha}}\Psi)\boldsymbol{L}):\mathbf{X}\Bigg]:\boldsymbol{W}\boldsymbol{\gamma}-\nabla\cdot\boldsymbol{q}+\rho r\\
&\qquad+\theta\big[\rho\partial_{\boldsymbol{W}}\Psi\boldsymbol{\gamma}^T-\nabla\times(\rho\partial_{\boldsymbol{\alpha}}\Psi)\boldsymbol{\gamma}^T+(\rho\partial_{\boldsymbol{W}}\Psi-\nabla\times\rho\partial_{\boldsymbol{\alpha}}\Psi):\boldsymbol{W}\mathbb{G}\big]:\dot{\boldsymbol{W}},
\end{aligned}\tag{2.60}$$

Use Eqs. (2.20) and (2.25) for the $\dot{\boldsymbol{W}}$ and $\dot{\boldsymbol{\alpha}}$ terms

$$\begin{aligned}
&\Big[\Big(\nabla\times\rho\partial_{\boldsymbol{\alpha}}\Psi-\rho\theta\partial^2_{\boldsymbol{W}\theta}\Psi\Big):\boldsymbol{W}\boldsymbol{\gamma}-\rho\theta\partial^2_{\theta\theta}\Psi\Big]\dot\theta+\theta\nabla\times\big(\rho\partial^2_{\boldsymbol{\alpha}\theta}\Psi\dot\theta\big):\boldsymbol{W}\boldsymbol{\gamma}-\rho\partial_{\boldsymbol{\alpha}}\Psi:\nabla\times\big(\boldsymbol{W}\boldsymbol{\gamma}\dot\theta\big)\\
&\quad=-\rho\partial_{\boldsymbol{W}}\Psi:\big(\boldsymbol{\alpha}\times\boldsymbol{v}^d\big)+\rho\partial_{\boldsymbol{\alpha}}\Psi:\nabla\times\big(\boldsymbol{\alpha}\times\boldsymbol{v}^d\big)-\nabla\cdot\boldsymbol{q}+\rho r\\
&\qquad+\rho\theta\big(\partial^2_{\theta\boldsymbol{W}}\Psi+\boldsymbol{W}\boldsymbol{\gamma}:\partial^2_{\boldsymbol{W}\boldsymbol{W}}\Psi\big):\Big(-\boldsymbol{W}\boldsymbol{L}+\boldsymbol{\alpha}\times\boldsymbol{v}^d+\boldsymbol{W}\boldsymbol{\gamma}\dot\theta\Big)\\
&\qquad+\rho\theta\big(\partial^2_{\theta\boldsymbol{\alpha}}\Psi+\boldsymbol{W}\boldsymbol{\gamma}:\partial^2_{\boldsymbol{W}\boldsymbol{\alpha}}\Psi\big):\Big(-\mathrm{tr}(\boldsymbol{L})\boldsymbol{\alpha}+\boldsymbol{\alpha}\boldsymbol{L}^T-\nabla\times(\boldsymbol{\alpha}\times\boldsymbol{v}^d+\boldsymbol{W}\boldsymbol{\gamma}\dot\theta)\Big)\\
&\qquad+\Bigg\{\frac{\theta\dot\rho}{\rho}\nabla\times\rho\partial_{\boldsymbol{\alpha}}\Psi-\theta\nabla\times\Bigg[\dot\rho\partial_{\boldsymbol{\alpha}}\Psi+\rho\partial^2_{\boldsymbol{\alpha}\boldsymbol{W}}\Psi:\Big(-\boldsymbol{W}\boldsymbol{L}+\boldsymbol{\alpha}\times\boldsymbol{v}^d+\boldsymbol{W}\boldsymbol{\gamma}\dot\theta\Big)\\
&\qquad+\rho\partial^2_{\boldsymbol{\alpha}\boldsymbol{\alpha}}\Psi:\Big(-\mathrm{tr}(\boldsymbol{L})\boldsymbol{\alpha}+\boldsymbol{\alpha}\boldsymbol{L}^T-\nabla\times(\boldsymbol{\alpha}\times\boldsymbol{v}^d)\Big)\Bigg]-\theta(\nabla(\rho\partial_{\boldsymbol{\alpha}}\Psi)\boldsymbol{L}):\mathbf{X}\Bigg\}:\boldsymbol{W}\boldsymbol{\gamma}\\
&\qquad+\theta\big[\rho\partial_{\boldsymbol{W}}\Psi\boldsymbol{\gamma}^T-\nabla\times(\rho\partial_{\boldsymbol{\alpha}}\Psi)\boldsymbol{\gamma}^T+(\rho\partial_{\boldsymbol{W}}\Psi-\nabla\times\rho\partial_{\boldsymbol{\alpha}}\Psi):\boldsymbol{W}\mathbb{G}\big]:\Big(-\boldsymbol{W}\boldsymbol{L}+\boldsymbol{\alpha}\times\boldsymbol{v}^d+\boldsymbol{W}\boldsymbol{\gamma}\dot\theta\Big),
\end{aligned}\tag{2.61}$$

Collecting all $\dot{\theta}$ terms on the left, using Eq. $(2.41)_2$ and grouping terms on the right gives

$$
\begin{aligned}
&\Bigg\{ \Big[\nabla\times\rho\partial_{\boldsymbol{\alpha}}\Psi(\mathbb{1}+\theta\boldsymbol{\gamma}^T) - 2\rho\theta\partial^2_{\boldsymbol{W}\theta}\Psi - \rho\theta\boldsymbol{W}\boldsymbol{\gamma} : \partial^2_{\boldsymbol{W}\boldsymbol{W}}\Psi - \rho\theta\partial_{\boldsymbol{W}}\Psi\boldsymbol{\gamma}^T \\
&\qquad - \theta(\rho\partial_{\boldsymbol{W}}\Psi - \nabla\times\rho\partial_{\boldsymbol{\alpha}}\Psi) : \boldsymbol{W}\mathbb{G} \Big] : \boldsymbol{W}\boldsymbol{\gamma} - \rho\theta\partial^2_{\theta\theta}\Psi \Bigg\}\dot{\theta} + \theta\nabla\times\left(\rho\partial^2_{\boldsymbol{\alpha}\theta}\Psi\dot{\theta}\right) : \boldsymbol{W}\boldsymbol{\gamma} \\
&- \left[\rho\partial_{\boldsymbol{\alpha}}\Psi - \rho\theta\left(\partial^2_{\theta\boldsymbol{\alpha}}\Psi + \boldsymbol{W}\boldsymbol{\gamma} : \partial^2_{\boldsymbol{W}\boldsymbol{\alpha}}\Psi\right)\right] : \nabla\times\left(\boldsymbol{W}\boldsymbol{\gamma}\dot{\theta}\right) \\
&+ \theta\nabla\times\left[\rho\partial^2_{\boldsymbol{\alpha}\boldsymbol{W}}\Psi : \boldsymbol{W}\boldsymbol{\gamma}\dot{\theta} - \rho\partial^2_{\boldsymbol{\alpha}\boldsymbol{\alpha}}\Psi : \nabla\times\left(\boldsymbol{W}\boldsymbol{\gamma}\dot{\theta}\right)\right] : \boldsymbol{W}\boldsymbol{\gamma} \\
&= \\
&\quad -\nabla\cdot\boldsymbol{q} + \rho r + \Bigg[-\rho\partial_{\boldsymbol{W}}\Psi\left(\mathbb{1}-\theta\boldsymbol{\gamma}^T\right) + \theta(\rho\partial_{\boldsymbol{W}}\Psi - \nabla\times\rho\partial_{\boldsymbol{\alpha}}\Psi) : \boldsymbol{W}\mathbb{G} - \theta\nabla\times(\rho\partial_{\boldsymbol{\alpha}}\Psi)\boldsymbol{\gamma}^T \\
&\qquad + \rho\theta\left(\partial^2_{\theta\boldsymbol{W}}\Psi + \boldsymbol{W}\boldsymbol{\gamma} : \partial^2_{\boldsymbol{W}\boldsymbol{W}}\Psi\right)\Bigg] : \left(\boldsymbol{\alpha}\times\boldsymbol{v}^d\right) + \Bigg\{ -\rho\theta\boldsymbol{W}^T\left(\partial^2_{\theta\boldsymbol{W}}\Psi + \boldsymbol{W}\boldsymbol{\gamma} : \partial^2_{\boldsymbol{W}\boldsymbol{W}}\Psi\right) \\
&\qquad - \left[\rho\theta\left(\partial^2_{\theta\boldsymbol{\alpha}}\Psi + \boldsymbol{W}\boldsymbol{\gamma} : \partial^2_{\boldsymbol{W}\boldsymbol{\alpha}}\Psi\right) : \boldsymbol{\alpha}\right]\mathbb{1} + \left[\rho\theta\left(\partial^2_{\theta\boldsymbol{\alpha}}\Psi + \boldsymbol{W}\boldsymbol{\gamma} : \partial^2_{\boldsymbol{W}\boldsymbol{\alpha}}\Psi\right)^T\boldsymbol{\alpha}\right] \\
&\qquad + \theta\left[-\rho(\boldsymbol{W}^T\partial_{\boldsymbol{W}}\Psi)\boldsymbol{\gamma}^T + \boldsymbol{W}^T\nabla\times(\rho\partial_{\boldsymbol{\alpha}}\Psi)\boldsymbol{\gamma}^T + \left(-\rho\boldsymbol{W}^T\partial_{\boldsymbol{W}}\Psi + \boldsymbol{W}^T\nabla\times\rho\partial_{\boldsymbol{\alpha}}\Psi\right) : \boldsymbol{W}\mathbb{G}\right] \Bigg\} : \boldsymbol{L} \\
&\quad + \left[\rho\partial_{\boldsymbol{\alpha}}\Psi - \rho\theta\left(\partial^2_{\theta\boldsymbol{\alpha}}\Psi + \boldsymbol{W}\boldsymbol{\gamma} : \partial^2_{\boldsymbol{W}\boldsymbol{\alpha}}\Psi\right)\right] : \nabla\times\left(\boldsymbol{\alpha}\times\boldsymbol{v}^d\right) \\
&\quad + \Bigg\{ \frac{\theta\dot{\rho}}{\rho}\nabla\times\rho\partial_{\boldsymbol{\alpha}}\Psi - \theta\nabla\times\Bigg[\dot{\rho}\partial_{\boldsymbol{\alpha}}\Psi + \rho\partial^2_{\boldsymbol{\alpha}\boldsymbol{W}}\Psi : \Big(-\boldsymbol{W}\boldsymbol{L} + \boldsymbol{\alpha}\times\boldsymbol{v}^d\Big) \\
&\qquad + \rho\partial^2_{\boldsymbol{\alpha}\boldsymbol{\alpha}}\Psi : \Big(-\mathrm{tr}(\boldsymbol{L})\boldsymbol{\alpha} + \boldsymbol{\alpha}\boldsymbol{L}^T - \nabla\times(\boldsymbol{\alpha}\times\boldsymbol{v}^d)\Big)\Bigg] - \theta(\nabla(\rho\partial_{\boldsymbol{\alpha}}\Psi)\boldsymbol{L}) : \mathbf{X} \Bigg\} : \boldsymbol{W}\boldsymbol{\gamma}.
\end{aligned}
\tag{2.62}
$$

Eq. (2.62) covers the most general case, in which Ψ could have coupled terms between the state variables $\boldsymbol{W}$, θ and $\boldsymbol{\alpha}$. We recall here that the present model is applicable in the solid state of the body, such that Eq. (2.62) is valid for θ below the solidus temperature.

To address the main implications of the new physical coupling between the evolution of the general thermomechanical defect density $\boldsymbol{\alpha}$ and the flux of thermal strains (Eq. (2.20)), an analysis of the structure of Eq. (2.62) is carried out in Appendix D in a simplified linear, one-dimensional case. The following aspects stand out:

- In the adiabatic case, neglecting the heat diffusion term, the temperature evolution remains governed by a PDE, owing to the presence of spatial derivatives of θ on the left-hand side of Eq. (2.62).

- The behaviour of the solutions of Eq. (2.62) is in the form of *dispersive temperature waves* i.e., with finite propagation speed. It arises from the mixed temporal and spatial derivatives in Eq. (2.62), which in turn occur because $\boldsymbol{\alpha}$ is introduced as an internal state variable.

- The well-posedness of Eq. (2.62) is shown in a linearised setting. Along with the expected decay for a range of wavenumbers, the solution also admits well-posed growth. This can be the source of spatial patterning resulting from the growth of some Fourier components in the temperature.

Generally, when considering Fourier's law of heat conduction as the constitutive statement for the heat conduction vector (Eq. (2.44)), the resulting temperature evolution is such that a temperature change in the body is immediately felt throughout the entirety of it, giving rise to an infinite temperature propagation speed. To overcome this limitation, multiple strategies have been employed in the literature, usually involving the use of an extended constitutive relation for the heat flux vector that considers its rate associated with a certain relaxation time. This results in a hyperbolic evolution law for the temperature evolution, thus giving rise to wave-like solutions of the temperature field, which propagate at finite speeds (see Joseph and Preziosi, 1989 and the references therein for a broad overview, including that of the pioneering work of Cattaneo, 1948).

More recently, Mariano, 2017; Mariano and Spadini, 2022 analysed a rigid thermal conductor and showed that, by considering the existence of a geometrical descriptor of the microstructure of a body, the energy balance statement leads to a finite speed of temperature propagation governed by a hyperbolic PDE. Their result is said to be independent of the microstructure type, provided that the latter is sensitive to temperature changes. Moreover, their approach did not require any changes to Fourier's law of heat conduction. The theory presented here seems to align well with these results. In our case, the thermomechanical defect density $\boldsymbol{\alpha}$ can be seen as the descriptor that provides information about low-dimensional structures (dislocation lines and incompatibilities in thermal strains) on a larger scale. The fundamental statement of the evolution of $\boldsymbol{\alpha}$ (Eq. (2.20)) comprises the effect of a transient temperature field, which in turn results in convection-diffusion effects in the PDE that governs the temperature evolution in the body (Eq. (2.62)) due to the accounting of the energetic contribution of $\boldsymbol{\alpha}$ to Helmholtz free energy (Eq. (2.38)). Similarly to Mariano and Spadini, 2022, the use here of Fourier's law (Eq. (2.44)) did not impede this result, and the obtained temperature field propagates at finite speeds.

2.4.7 Taylor-Quinney coefficient

In the pioneering work of Taylor and Quinney, 1934, the authors measured the amount of energy that remained stored in metallic rods after severe plastic deformation and introduced a coefficient, later called the Taylor-Quinney coefficient (TQC), defined as

$$\beta_{\text{int}} = \frac{W - Q}{W}, \tag{2.63}$$

where W corresponds to the total work done on a rod, and Q is the heat dissipated by it during the deformation. Afterwards, different definitions were used that fall under the same denomination of TQC (Rittel et al., 2017). Notably, the so-called *differential* TQC β_{diff} is used as a measure of the instantaneous partition of plastic work into heat and stored energy during deformation, while the *integral* TQC (Eq. (2.63)) expresses the amount of plastic work that is stored as latent energy in the body after deformation (Rittel, 1999, Rittel et al., 2017, Stimac et al., 2022).

Following Rosakis et al., 2000, from Eq. (2.62) we define

$$
\begin{aligned}
\dot{Q}^p = &\Bigg[-\rho\partial_{\boldsymbol{W}}\Psi\left(\mathbb{1}-\theta\boldsymbol{\gamma}^T\right)+\theta\left(\rho\partial_{\boldsymbol{W}}\Psi-\nabla\times\rho\partial_{\boldsymbol{\alpha}}\Psi\right):\boldsymbol{W}\mathbb{G}-\theta\nabla\times(\rho\partial_{\boldsymbol{\alpha}}\Psi)\boldsymbol{\gamma}^T \\
&+\rho\theta\left(\partial^2_{\theta\boldsymbol{W}}\Psi+\boldsymbol{W}\boldsymbol{\gamma}:\partial^2_{\boldsymbol{W}\boldsymbol{W}}\Psi\right)\Bigg]:\left(\boldsymbol{\alpha}\times\boldsymbol{v}^d\right) \\
&+\left[\rho\partial_{\boldsymbol{\alpha}}\Psi-\rho\theta\left(\partial^2_{\theta\boldsymbol{\alpha}}\Psi+\boldsymbol{W}\boldsymbol{\gamma}:\partial^2_{\boldsymbol{W}\boldsymbol{\alpha}}\Psi\right)\right]:\nabla\times\left(\boldsymbol{\alpha}\times\boldsymbol{v}^d\right) \\
&-\left\{\theta\nabla\times\left[\rho\partial^2_{\boldsymbol{\alpha}\boldsymbol{W}}\Psi:\left(\boldsymbol{\alpha}\times\boldsymbol{v}^d\right)-\rho\partial^2_{\boldsymbol{\alpha}\boldsymbol{\alpha}}\Psi:\nabla\times(\boldsymbol{\alpha}\times\boldsymbol{v}^d)\right]\right\}:\boldsymbol{W}\boldsymbol{\gamma} \\
\dot{Q}^e = &-\Bigg\{\rho\theta\boldsymbol{W}^T\left(\partial^2_{\theta\boldsymbol{W}}\Psi+\boldsymbol{W}\boldsymbol{\gamma}:\partial^2_{\boldsymbol{W}\boldsymbol{W}}\Psi\right)+\left[\rho\theta\left(\partial^2_{\theta\boldsymbol{\alpha}}\Psi+\boldsymbol{W}\boldsymbol{\gamma}:\partial^2_{\boldsymbol{W}\boldsymbol{\alpha}}\Psi\right):\boldsymbol{\alpha}\right]\mathbb{1} \\
&\qquad-\left[\rho\theta\left(\partial^2_{\theta\boldsymbol{\alpha}}\Psi+\boldsymbol{W}\boldsymbol{\gamma}:\partial^2_{\boldsymbol{W}\boldsymbol{\alpha}}\Psi\right)^T\boldsymbol{\alpha}\right]-\theta\Big[-\rho(\boldsymbol{W}^T\partial_{\boldsymbol{W}}\Psi)\boldsymbol{\gamma}^T+\boldsymbol{W}^T\nabla\times(\rho\partial_{\boldsymbol{\alpha}}\Psi)\boldsymbol{\gamma}^T \\
&\qquad+\left(-\rho\boldsymbol{W}^T\partial_{\boldsymbol{W}}\Psi+\boldsymbol{W}^T\nabla\times\rho\partial_{\boldsymbol{\alpha}}\Psi\right):\boldsymbol{W}\mathbb{G}\Big]\Bigg\}:\boldsymbol{L} \\
&-\Bigg\{\theta\nabla\times\Big[\dot{\rho}\partial_{\boldsymbol{\alpha}}\Psi-\rho\partial^2_{\boldsymbol{\alpha}\boldsymbol{W}}\Psi:\boldsymbol{W}\boldsymbol{L}+\rho\partial^2_{\boldsymbol{\alpha}\boldsymbol{\alpha}}\Psi:\left(-\operatorname{tr}(\boldsymbol{L})\boldsymbol{\alpha}+\boldsymbol{\alpha}\boldsymbol{L}^T\right)\Big] \\
&\qquad+\theta\left(\nabla(\rho\partial_{\boldsymbol{\alpha}}\Psi)\boldsymbol{L}\right):\mathbf{X}-\frac{\theta\dot{\rho}}{\rho}\nabla\times\rho\partial_{\boldsymbol{\alpha}}\Psi\Bigg\}:\boldsymbol{W}\boldsymbol{\gamma},
\end{aligned}
\tag{2.64}
$$

where $\dot{Q}^p$ is the heating due to inelastic effects governed by the thermomechanical defect density evolution and $\dot{Q}^e$ is the thermoelastic contribution to heating. We introduce the plastic work rate as $\dot{W}^p=-\rho\partial_{\boldsymbol{W}}\Psi:(\boldsymbol{\alpha}\times\boldsymbol{v}^d)$, so that the fraction of $\dot{W}^p$ converted into $\dot{Q}^p$ can be defined as

$$
\beta_{\text{diff}}=\frac{\dot{Q}^p}{\dot{W}^p}. \tag{2.65}
$$

Denoting the left-hand side of Eq. (2.62) as $\mathcal{L}[\dot{\theta}]$, and considering Eq. (2.65), we can rewrite the temperature evolution as

$$
\mathcal{L}[\dot{\theta}]=-\nabla\cdot\boldsymbol{q}+\rho r+\beta_{\text{diff}}\dot{W}^p+\dot{Q}^e, \tag{2.66}
$$

which shows that it is governed by heat diffusion, internal heat sources, plastic work due to the evolution of the thermomechanical defect density, and thermoelastic effects.

In our model, the rate of conversion of plastic work into heat (Eq. (2.65)) is influenced by the strain rates. This influence is manifested through the stress dependence of the line defect velocity $\boldsymbol{v}^d$ and defect source $\boldsymbol{S}$. The dependence of β on the loading conditions is well-established in the literature (see Rittel et al., 2017 and the references therein). The key aspect of our approach is that the rather straightforward argument of conservation of Burgers vector in Eq. (2.19) yields the structure of Eq. (2.66) that allows for studying temperature evolution during plastic work. In other approaches, a similar result is obtained with the introduction of phenomenological expressions for the accumulated plastic strains or other conventional plasticity-related variables (Stainier and Ortiz, 2010, Nieto-Fuentes et al., 2018, Longère, 2023, Zeng et al., 2022, Dæhli et al., 2023). Note that β_{diff} depends on the choice of Ψ, and the key point here is that our description of plasticity allows for studying plastic work repartition into heat directly from the evolution of thermomechanical defects while accounting for temperature effects and involving unambiguously definable quantities, measurable from the current state (at least in principle).

2.4.8 Initial boundary value problem of finite deformation field dislocations thermomechanics

In this section, we summarize the set of governing equations and constitutive relations of the model. The initial and boundary conditions are also shown. For an approach to solving for $\boldsymbol{W}$ using the Stokes-Helmholtz decomposition, as detailed in Acharya, 2004, we direct the reader to Appendix E.1.

Kinematics and dislocation density evolution

$$\dot{\boldsymbol{W}} + \boldsymbol{W}\boldsymbol{L} = \boldsymbol{\alpha} \times \boldsymbol{v}^d + \boldsymbol{W}\boldsymbol{\gamma}\dot{\theta} \tag{2.67a}$$

$$\mathring{\boldsymbol{\alpha}} = -\nabla \times \left(\boldsymbol{\alpha} \times \boldsymbol{v}^d + \boldsymbol{W}\boldsymbol{\gamma}\dot{\theta} \right), \quad \mathring{\boldsymbol{\alpha}} = \operatorname{tr}(\boldsymbol{L})\boldsymbol{\alpha} + \dot{\boldsymbol{\alpha}} - \boldsymbol{\alpha}\boldsymbol{L}^T \tag{2.67b}$$

$$\boldsymbol{v}^d = \frac{1}{\boldsymbol{B}} \left[(-\rho \partial_{\boldsymbol{W}} \Psi + \nabla \times \rho \partial_{\boldsymbol{\alpha}} \Psi)^T \boldsymbol{\alpha} \right] : \mathbf{X} \tag{2.67c}$$

Mass density evolution

$$\dot{\rho} + \nabla \cdot (\rho \boldsymbol{v}) = 0 \tag{2.67d}$$

Dynamics

$$\nabla \cdot \boldsymbol{\sigma} + \rho \boldsymbol{b}_f = \rho \dot{\boldsymbol{v}} \tag{2.67e}$$

$$\boldsymbol{\sigma} = -\rho \boldsymbol{W}^T \partial_{\boldsymbol{W}} \Psi + \rho (\partial_{\boldsymbol{\alpha}} \Psi)^T \boldsymbol{\alpha} - \rho (\partial_{\boldsymbol{\alpha}} \Psi : \boldsymbol{\alpha}) \mathbb{1} \tag{2.67f}$$

Temperature evolution

$$
\begin{aligned}
&\Bigg\{\Bigg[\nabla\times\rho\partial_{\boldsymbol{\alpha}}\Psi(\mathbb{1}+\theta\boldsymbol{\gamma}^T)-2\rho\theta\partial^2_{\boldsymbol{W}\theta}\Psi-\rho\theta\boldsymbol{W}\boldsymbol{\gamma}:\partial^2_{\boldsymbol{W}\boldsymbol{W}}\Psi-\rho\theta\partial_{\boldsymbol{W}}\Psi\boldsymbol{\gamma}^T\\
&\qquad-\theta(\rho\partial_{\boldsymbol{W}}\Psi-\nabla\times\rho\partial_{\boldsymbol{\alpha}}\Psi):\boldsymbol{W}\mathbb{G}\Bigg]:\boldsymbol{W}\boldsymbol{\gamma}-\rho\theta\partial^2_{\theta\theta}\Psi\Bigg\}\dot{\theta}+\theta\nabla\times\left(\rho\partial^2_{\boldsymbol{\alpha}\theta}\Psi\dot{\theta}\right):\boldsymbol{W}\boldsymbol{\gamma}\\
&-\left[\rho\partial_{\boldsymbol{\alpha}}\Psi-\rho\theta\left(\partial^2_{\theta\boldsymbol{\alpha}}\Psi+\boldsymbol{W}\boldsymbol{\gamma}:\partial^2_{\boldsymbol{W}\boldsymbol{\alpha}}\Psi\right)\right]:\nabla\times\left(\boldsymbol{W}\boldsymbol{\gamma}\dot{\theta}\right)\\
&+\theta\nabla\times\left[\rho\partial^2_{\boldsymbol{\alpha}\boldsymbol{W}}\Psi:\boldsymbol{W}\boldsymbol{\gamma}\dot{\theta}-\rho\partial^2_{\boldsymbol{\alpha}\boldsymbol{\alpha}}\Psi:\nabla\times\left(\boldsymbol{W}\boldsymbol{\gamma}\dot{\theta}\right)\right]:\boldsymbol{W}\boldsymbol{\gamma}\\
&\quad=-\nabla\cdot\boldsymbol{q}+\rho r+\Bigg[-\rho\partial_{\boldsymbol{W}}\Psi\left(\mathbb{1}-\theta\boldsymbol{\gamma}^T\right)+\theta(\rho\partial_{\boldsymbol{W}}\Psi-\nabla\times\rho\partial_{\boldsymbol{\alpha}}\Psi):\boldsymbol{W}\mathbb{G}-\theta\nabla\times(\rho\partial_{\boldsymbol{\alpha}}\Psi)\boldsymbol{\gamma}^T\\
&\qquad+\rho\theta\left(\partial^2_{\theta\boldsymbol{W}}\Psi+\boldsymbol{W}\boldsymbol{\gamma}:\partial^2_{\boldsymbol{W}\boldsymbol{W}}\Psi\right)\Bigg]:\left(\boldsymbol{\alpha}\times\boldsymbol{v}^d\right)+\Bigg\{-\rho\theta\boldsymbol{W}^T\left(\partial^2_{\theta\boldsymbol{W}}\Psi+\boldsymbol{W}\boldsymbol{\gamma}:\partial^2_{\boldsymbol{W}\boldsymbol{W}}\Psi\right)\\
&\qquad-\left[\rho\theta\left(\partial^2_{\theta\boldsymbol{\alpha}}\Psi+\boldsymbol{W}\boldsymbol{\gamma}:\partial^2_{\boldsymbol{W}\boldsymbol{\alpha}}\Psi\right):\boldsymbol{\alpha}\right]\mathbb{1}+\left[\rho\theta\left(\partial^2_{\theta\boldsymbol{\alpha}}\Psi+\boldsymbol{W}\boldsymbol{\gamma}:\partial^2_{\boldsymbol{W}\boldsymbol{\alpha}}\Psi\right)^T\boldsymbol{\alpha}\right]\\
&\qquad+\theta\left[-\rho(\boldsymbol{W}^T\partial_{\boldsymbol{W}}\Psi)\boldsymbol{\gamma}^T+\boldsymbol{W}^T\nabla\times(\rho\partial_{\boldsymbol{\alpha}}\Psi)\boldsymbol{\gamma}^T+\left(-\rho\boldsymbol{W}^T\partial_{\boldsymbol{W}}\Psi+\boldsymbol{W}^T\nabla\times\rho\partial_{\boldsymbol{\alpha}}\Psi\right):\boldsymbol{W}\mathbb{G}\right]\Bigg\}:\boldsymbol{L}\\
&\quad+\left[\rho\partial_{\boldsymbol{\alpha}}\Psi-\rho\theta\left(\partial^2_{\theta\boldsymbol{\alpha}}\Psi+\boldsymbol{W}\boldsymbol{\gamma}:\partial^2_{\boldsymbol{W}\boldsymbol{\alpha}}\Psi\right)\right]:\nabla\times\left(\boldsymbol{\alpha}\times\boldsymbol{v}^d\right)\\
&\quad+\Bigg\{\frac{\theta\dot{\rho}}{\rho}\nabla\times\rho\partial_{\boldsymbol{\alpha}}\Psi-\theta\nabla\times\Bigg[\dot{\rho}\partial_{\boldsymbol{\alpha}}\Psi+\rho\partial^2_{\boldsymbol{\alpha}\boldsymbol{W}}\Psi:\left(-\boldsymbol{W}\boldsymbol{L}+\boldsymbol{\alpha}\times\boldsymbol{v}^d\right)\\
&\qquad+\rho\partial^2_{\boldsymbol{\alpha}\boldsymbol{\alpha}}\Psi:\left(-\operatorname{tr}(\boldsymbol{L})\boldsymbol{\alpha}+\boldsymbol{\alpha}\boldsymbol{L}^T-\nabla\times(\boldsymbol{\alpha}\times\boldsymbol{v}^d)\right)\Bigg]-\theta\left(\nabla(\rho\partial_{\boldsymbol{\alpha}}\Psi)\boldsymbol{L}\right):\mathbf{X}\Bigg\}:\boldsymbol{W}\boldsymbol{\gamma}
\end{aligned}
\tag{2.67g}
$$

$$
\boldsymbol{q}=-\boldsymbol{K}\nabla\theta. \tag{2.67h}
$$

2.4.8.1 Boundary conditions

Naturally, the closure of Eq. (2.67) requires the specification of the initial and boundary conditions, presented in what follows.

The thermomechanical defect density transport, Eq. (2.67b), requires the specification

$$
(\boldsymbol{v}^d\cdot\hat{\boldsymbol{n}})\boldsymbol{\alpha}=\overline{\boldsymbol{F}}_{\alpha}\quad\text{on}\quad\partial\Omega_t^-, \tag{2.68}
$$

which is enough to ensure uniqueness, where $\overline{\boldsymbol{F}}_{\alpha}$ is a prescribed dislocation flux and $\partial\Omega_t^-$

corresponds to the part of $\partial\Omega_t$ where $\boldsymbol{v}^d \cdot \hat{\boldsymbol{n}} < 0$, i.e., only the inflow of defects into the body needs to be prescribed (Acharya, 2003).

The balance of linear momentum in Eq. (2.67e) requires the specification of standard velocity and traction rate boundary conditions on complementary parts of $\partial\Omega_t$ (R. Arora et al., 2020).

Finally, the temperature evolution Eq. (2.67g) is completed with

$$\begin{aligned} &\theta = \bar{\theta} && \text{on} \quad \partial\Omega_t^{\theta} \\ &\boldsymbol{q} \cdot \hat{\boldsymbol{n}} = \overline{q} && \text{on} \quad \partial\Omega_t^{q}, \end{aligned} \tag{2.69}$$

where $\bar{\theta}$ and $\overline{q}$ are prescribed quantities, $\partial\Omega_t^q \cap \partial\Omega_t^\theta = \emptyset$, and $\partial\Omega_t^q \cup \partial\Omega_t^\theta = \partial\Omega_t$.

2.4.8.2 Initial conditions

The defect transport Eq. (2.67b) is solved considering a given initial defect density $\boldsymbol{\alpha}_0$, i.e. $\boldsymbol{\alpha}(\boldsymbol{x}, 0) = \boldsymbol{\alpha}_0(\boldsymbol{x})$.

The balance of linear momentum Eq. (2.67e) requires the specification of an initial material velocity profile $\boldsymbol{v}_0$, i.e.
$\boldsymbol{v}(\boldsymbol{x}, 0) = \boldsymbol{v}_0(\boldsymbol{x})$.

Furthermore, the temperature evolution Eq. (2.67g) requires the specification of an initial temperature profile in the body, that is, $\theta(\boldsymbol{x}, 0) = \theta_0(\boldsymbol{x})$ for a given θ_0.

2.5 Geometric linearisation

In this section, we geometrically linearise the model, i.e. develop it in a small deformation framework (but large temperature changes are allowed). In the small deformation case, $\boldsymbol{W}$ can be approximated as

$$\boldsymbol{W} = \boldsymbol{F}^{e-1} = (\mathbb{1} + \boldsymbol{U}^e)^{-1} \approx \mathbb{1} - \boldsymbol{U}^e, \tag{2.70}$$

where $\boldsymbol{U}^e$ is the elastic distortion tensor, with $\|\boldsymbol{U}^e\| \ll 1$. In the present small deformation setting, the superposed dot denotes a partial derivative with respect to t, and we assume that $\dot{\rho} = 0$ and $\rho/\rho_0 \approx 1$.

We also assume $\boldsymbol{v} = \dot{\boldsymbol{u}}$, where $\boldsymbol{u}$ is the displacement field. Then, using Eq. (2.70), the velocity gradient $\boldsymbol{L}$ given by Eq. (2.26) can be approximated as

$$\boldsymbol{L} = \nabla\dot{\boldsymbol{u}} = \dot{\boldsymbol{U}}^e + \boldsymbol{\alpha} \times \boldsymbol{v}^d + \boldsymbol{\gamma}\dot{\theta}. \tag{2.71}$$

where in this case $\boldsymbol{\gamma} = \sum_{i=1}^{3} d_i(\theta)\hat{\boldsymbol{e}}_i \otimes \hat{\boldsymbol{e}}_i$. Without loss of generality, we can define $\dot{\boldsymbol{U}}^p := \boldsymbol{\alpha} \times \boldsymbol{v}^d$

as the plastic distortion rate and $\dot{\boldsymbol{\varepsilon}}^{\theta} := \boldsymbol{\gamma}\dot{\theta}$ as the thermal strain rate in the small deformation formulation. Integrating Eq. (2.71) in time, we get

$$\nabla \boldsymbol{u} = \boldsymbol{U}^{e} + \boldsymbol{U}^{p} + \boldsymbol{\varepsilon}^{\theta}, \tag{2.72}$$

where a time-independent tensor field is ignored. This expression is the well-known additive decomposition of the displacement gradient tensor that is relevant in the small deformation case.

Considering Eq. (2.70), the definition of the Burgers vector in Eq. (2.17) becomes

$$\boldsymbol{b} = \oint_{c} \boldsymbol{U}^{e} \mathbf{d}\boldsymbol{x} = \int_{s} (\nabla \times \boldsymbol{U}^{e}) \hat{\boldsymbol{n}} \, \mathrm{d}s = \int_{s} \boldsymbol{\alpha} \hat{\boldsymbol{n}} \, \mathrm{d}s, \tag{2.73}$$

where s in an arbitrary closed surface in Ω, whose boundary and unit normal are c and $\hat{\boldsymbol{n}}$, respectively, and the second equality is obtained through Stokes' theorem. The thermomechanical defect density is now defined as

$$\boldsymbol{\alpha} = \nabla \times \boldsymbol{U}^{e}, \tag{2.74}$$

for which we obtain the evolution statement (Acharya, 2011, Upadhyay, 2020)

$$\begin{aligned} &\dot{\boldsymbol{\alpha}} = \nabla \times \dot{\boldsymbol{U}}^{e} \\ \implies &\dot{\boldsymbol{\alpha}} = -\nabla \times (\boldsymbol{\alpha} \times \boldsymbol{v}^{d}) - \nabla \times (\boldsymbol{\gamma}\dot{\theta}) \end{aligned} \tag{2.75}$$

where Eq. (2.71) was used. These expressions are very similar to the ones derived in Upadhyay, 2020, except for one important detail, which is addressed in section 2.6.3.

In the geometrically linear setting, the additive decomposition of the displacement gradient (Eq. (2.72)) allows for considering the Helmholtz free energy density as $\Psi \equiv \Psi(\boldsymbol{\varepsilon}^{e}, \boldsymbol{\alpha}) = \Psi(\boldsymbol{\varepsilon} - \boldsymbol{\varepsilon}^{p} - \boldsymbol{\varepsilon}^{\theta}, \boldsymbol{\alpha}) = \Psi(\boldsymbol{\varepsilon} - \boldsymbol{\varepsilon}^{p}, \theta, \boldsymbol{\alpha})$, with $\boldsymbol{\varepsilon} = \mathrm{sym}(\nabla \boldsymbol{u})$ and $\boldsymbol{\varepsilon}^{e,p} = \mathrm{sym}(\boldsymbol{U}^{e,p})$, such that

$$\dot{\Psi} = \partial_{(\boldsymbol{\varepsilon} - \boldsymbol{\varepsilon}^{p})} \Psi : (\dot{\boldsymbol{\varepsilon}} - \dot{\boldsymbol{\varepsilon}}^{p}) + \partial_{\theta} \Psi \, \dot{\theta} + \partial_{\boldsymbol{\alpha}} \Psi : \dot{\boldsymbol{\alpha}}. \tag{2.76}$$

Considering $\boldsymbol{\sigma} : \boldsymbol{L} = \boldsymbol{\sigma} : \boldsymbol{\varepsilon}$ in the global dissipation (Eq. (2.37)), as well as replacing Eq. (2.76) and Eq. (2.75) for $\dot{\Psi}$ and $\dot{\boldsymbol{\alpha}}$, respectively, and using Eqs. (F.3) and (F.4) allows for the definition of the following constitutive relations:

$$\boldsymbol{\sigma} = \rho \partial_{(\boldsymbol{\varepsilon} - \boldsymbol{\varepsilon}^{p})} \Psi \tag{2.77a}$$

$$\eta = -\partial_{\theta} \Psi + \frac{1}{\rho} \nabla \times (\rho \partial_{\boldsymbol{\alpha}} \Psi) : \boldsymbol{\gamma} \tag{2.77b}$$

$$\boldsymbol{v}^{d} = \frac{1}{\boldsymbol{B}} \left[(\boldsymbol{\sigma} + \nabla \times \rho \partial_{\boldsymbol{\alpha}} \Psi)^{T} \boldsymbol{\alpha} \right] : \mathbf{X} \tag{2.77c}$$

$$\boldsymbol{q} = \boldsymbol{K} \nabla \theta. \tag{2.77d}$$

For the temperature evolution equation, in the small-strains case, Eq. (2.48) becomes

$$\rho\left[\partial_{(\boldsymbol{\varepsilon}-\boldsymbol{\varepsilon}^p)}\Psi:(\dot{\boldsymbol{\varepsilon}}-\dot{\boldsymbol{\varepsilon}}^p)+\partial_\theta\Psi\dot{\theta}+\partial_{\boldsymbol{\alpha}}\Psi:\dot{\boldsymbol{\alpha}}+\dot{\theta}\eta+\theta\dot{\eta}\right]=\boldsymbol{\sigma}:\dot{\boldsymbol{\varepsilon}}-\nabla\cdot\boldsymbol{q}+\rho r. \tag{2.78}$$

Now, by taking the derivative of Eq. (2.77b) with respect to time, we get

$$\begin{aligned}\dot{\eta}=&-\partial^2_{\theta(\boldsymbol{\varepsilon}-\boldsymbol{\varepsilon}^p)}\Psi:(\dot{\boldsymbol{\varepsilon}}-\dot{\boldsymbol{\varepsilon}}^p)-\partial^2_{\theta\theta}\Psi\dot{\theta}-\partial^2_{\theta\boldsymbol{\alpha}}\Psi:\dot{\boldsymbol{\alpha}}\\&+\frac{1}{\rho}\nabla\times\left(\rho\partial^2_{\boldsymbol{\alpha}(\boldsymbol{\varepsilon}-\boldsymbol{\varepsilon}^p)}\Psi:(\dot{\boldsymbol{\varepsilon}}-\dot{\boldsymbol{\varepsilon}}^p)+\rho\partial^2_{\boldsymbol{\alpha}\theta}\Psi\dot{\theta}+\rho\partial^2_{\boldsymbol{\alpha}\boldsymbol{\alpha}}\Psi:\dot{\boldsymbol{\alpha}}\right):\boldsymbol{\gamma}.\end{aligned} \tag{2.79}$$

Inserting Eq. (2.79) into Eq. (2.78) gives

$$\begin{aligned}&\rho\partial_{(\boldsymbol{\varepsilon}-\boldsymbol{\varepsilon}^p)}\Psi:(\dot{\boldsymbol{\varepsilon}}-\dot{\boldsymbol{\varepsilon}}^p)+\rho\partial_{\boldsymbol{\alpha}}\Psi:\dot{\boldsymbol{\alpha}}-\rho\theta\partial^2_{\theta(\boldsymbol{\varepsilon}-\boldsymbol{\varepsilon}^p)}\Psi:(\dot{\boldsymbol{\varepsilon}}-\dot{\boldsymbol{\varepsilon}}^p)-\rho\theta\partial^2_{\theta\theta}\Psi\dot{\theta}-\rho\theta\partial^2_{\theta\boldsymbol{\alpha}}\Psi:\dot{\boldsymbol{\alpha}}\\&\quad+\theta\nabla\times\left[\rho\partial^2_{\boldsymbol{\alpha}(\boldsymbol{\varepsilon}-\boldsymbol{\varepsilon}^p)}\Psi:(\dot{\boldsymbol{\varepsilon}}-\dot{\boldsymbol{\varepsilon}}^p)+\rho\partial^2_{\boldsymbol{\alpha}\theta}\Psi\dot{\theta}+\rho\partial^2_{\boldsymbol{\alpha}\boldsymbol{\alpha}}\Psi:\dot{\boldsymbol{\alpha}}\right]:\boldsymbol{\gamma}+\dot{\theta}\nabla\times(\rho\partial_{\boldsymbol{\alpha}}\Psi):\boldsymbol{\gamma}\\&=-\nabla\cdot\boldsymbol{q}+\boldsymbol{\sigma}:\dot{\boldsymbol{\varepsilon}}+\rho r\end{aligned} \tag{2.80}$$

Collecting the $\dot{\theta}$ terms on the left-hand side and using Eq. (2.77a)

$$\begin{aligned}&\left(\nabla\times\rho\partial_{\boldsymbol{\alpha}}\Psi:\boldsymbol{\gamma}-\rho\theta\partial^2_{\theta\theta}\Psi\right)\dot{\theta}+\theta\nabla\times\left(\rho\partial^2_{\boldsymbol{\alpha}\theta}\Psi\dot{\theta}\right):\boldsymbol{\gamma}=\boldsymbol{\sigma}:\dot{\boldsymbol{\varepsilon}}^p-\rho\partial_{\boldsymbol{\alpha}}\Psi:\dot{\boldsymbol{\alpha}}-\nabla\cdot\boldsymbol{q}+\rho r\\&+\rho\theta\partial^2_{\theta(\boldsymbol{\varepsilon}-\boldsymbol{\varepsilon}^p)}\Psi:(\dot{\boldsymbol{\varepsilon}}-\dot{\boldsymbol{\varepsilon}}^p)+\rho\theta\partial^2_{\theta\boldsymbol{\alpha}}\Psi:\dot{\boldsymbol{\alpha}}-\theta\nabla\times\left[\rho\partial^2_{\boldsymbol{\alpha}(\boldsymbol{\varepsilon}-\boldsymbol{\varepsilon}^p)}\Psi:(\dot{\boldsymbol{\varepsilon}}-\dot{\boldsymbol{\varepsilon}}^p)+\rho\partial^2_{\boldsymbol{\alpha}\boldsymbol{\alpha}}\Psi:\dot{\boldsymbol{\alpha}}\right]:\boldsymbol{\gamma}\end{aligned} \tag{2.81}$$

Using Eq. (2.75) for $\dot{\boldsymbol{\alpha}}$ and writing $\dot{\boldsymbol{\varepsilon}}-\dot{\boldsymbol{\varepsilon}}^p=\dot{\boldsymbol{\varepsilon}}^e+\boldsymbol{\gamma}\dot{\theta}$ from Eq. (2.71), we have

$$\begin{aligned}&\left(\nabla\times\rho\partial_{\boldsymbol{\alpha}}\Psi:\boldsymbol{\gamma}-\rho\theta\partial^2_{\theta\theta}\Psi\right)\dot{\theta}+\theta\nabla\times\left(\rho\partial^2_{\boldsymbol{\alpha}\theta}\Psi\dot{\theta}\right):\boldsymbol{\gamma}=\boldsymbol{\sigma}:\dot{\boldsymbol{\varepsilon}}^p+\rho\theta\partial^2_{\theta(\boldsymbol{\varepsilon}-\boldsymbol{\varepsilon}^p)}\Psi:(\dot{\boldsymbol{\varepsilon}}^e+\boldsymbol{\gamma}\dot{\theta})\\&\quad+\rho(\partial_{\boldsymbol{\alpha}}\Psi-\theta\partial^2_{\theta\boldsymbol{\alpha}}\Psi):\nabla\times(\boldsymbol{\alpha}\times\boldsymbol{v}^d+\boldsymbol{\gamma}\dot{\theta})-\nabla\cdot\boldsymbol{q}+\rho r\\&\quad-\theta\nabla\times\left[\rho\partial^2_{\boldsymbol{\alpha}(\boldsymbol{\varepsilon}-\boldsymbol{\varepsilon}^p)}\Psi:(\dot{\boldsymbol{\varepsilon}}^e+\boldsymbol{\gamma}\dot{\theta})-\rho\partial^2_{\boldsymbol{\alpha}\boldsymbol{\alpha}}\Psi:\nabla\times(\boldsymbol{\alpha}\times\boldsymbol{v}^d+\boldsymbol{\gamma}\dot{\theta})\right]:\boldsymbol{\gamma}\end{aligned} \tag{2.82}$$

Rearranging terms, and considering $\boldsymbol{\sigma}:\dot{\boldsymbol{\varepsilon}}^p=\boldsymbol{\sigma}:\dot{\boldsymbol{U}}^p=\boldsymbol{\sigma}:\left(\boldsymbol{\alpha}\times\boldsymbol{v}^d\right)$, we arrive at

$$\begin{aligned}&\left[\left(\nabla\times\rho\partial_{\boldsymbol{\alpha}}\Psi-\rho\theta\partial^2_{\theta(\boldsymbol{\varepsilon}-\boldsymbol{\varepsilon}^p)}\Psi\right):\boldsymbol{\gamma}-\rho\theta\partial^2_{\theta\theta}\Psi\right]\dot{\theta}+\theta\nabla\times\left(\rho\partial^2_{\boldsymbol{\alpha}\theta}\Psi\dot{\theta}\right):\boldsymbol{\gamma}\\&\quad-\rho\left(\partial_{\boldsymbol{\alpha}}\Psi+\theta\partial^2_{\theta\boldsymbol{\alpha}}\Psi\right):\nabla\times(\boldsymbol{\gamma}\dot{\theta})+\theta\nabla\times\left[\rho\partial^2_{\boldsymbol{\alpha}(\boldsymbol{\varepsilon}-\boldsymbol{\varepsilon}^p)}\Psi:\boldsymbol{\gamma}\dot{\theta}-\rho\partial^2_{\boldsymbol{\alpha}\boldsymbol{\alpha}}\Psi:\nabla\times(\boldsymbol{\gamma}\dot{\theta})\right]:\boldsymbol{\gamma}\\&=\boldsymbol{\sigma}:\left(\boldsymbol{\alpha}\times\boldsymbol{v}^d\right)+\rho\theta\partial^2_{\theta(\boldsymbol{\varepsilon}-\boldsymbol{\varepsilon}^p)}\Psi:\dot{\boldsymbol{\varepsilon}}^e-\nabla\cdot\boldsymbol{q}+\rho r\\&\quad+\left\{\rho(\partial_{\boldsymbol{\alpha}}\Psi-\theta\partial^2_{\theta\boldsymbol{\alpha}}\Psi):\nabla\times(\boldsymbol{\alpha}\times\boldsymbol{v}^d)+\theta\nabla\times\left[\rho\partial^2_{\boldsymbol{\alpha}\boldsymbol{\alpha}}\Psi:\nabla\times(\boldsymbol{\alpha}\times\boldsymbol{v}^d)\right]:\boldsymbol{\gamma}\right\}\\&\quad-\theta\nabla\times\left(\rho\partial^2_{\boldsymbol{\alpha}(\boldsymbol{\varepsilon}-\boldsymbol{\varepsilon}^p)}\Psi:\dot{\boldsymbol{\varepsilon}}^e\right):\boldsymbol{\gamma}\end{aligned} \tag{2.83}$$

where the left-hand side represents the heat storage, with coefficients depending on the thermodynamic driving force of $\boldsymbol{\alpha}$, thermoelastic coupling, heat capacity and coupling between $\boldsymbol{\alpha}$ and θ or $(\boldsymbol{\varepsilon}-\boldsymbol{\varepsilon}^p)$; on the right-hand side, from left to right, we have plastic work, thermoelastic effect, heat diffusion, heat source, heat generation due to thermomechanical defect density evolution

and a coupled term between $\boldsymbol{\alpha}$ and deformation evolution. Eq. (2.83) retains the same structure as Eq. (2.62) in terms of the derivatives of θ involved, so that the analysis in Appendix D also applies to this case.

The equations of the geometrically linearised theory are grouped and presented in the set below. As in Section 2.4.8, we direct the reader to Appendix E.2 for an approach to solving for $\boldsymbol{U}^e$ using the Stokes-Helmholtz decomposition.

Kinematics and dislocation density evolution

$$\dot{\boldsymbol{U}}^e = \nabla\dot{\boldsymbol{u}} - \boldsymbol{\alpha}\times\boldsymbol{v}^d - \boldsymbol{\gamma}\dot{\theta} \tag{2.84a}$$

$$\dot{\boldsymbol{\alpha}} = -\nabla\times\left(\boldsymbol{\alpha}\times\boldsymbol{v}^d + \boldsymbol{\gamma}\dot{\theta}\right) \tag{2.84b}$$

$$\boldsymbol{v}^d = \frac{1}{\boldsymbol{B}}\left[(\boldsymbol{\sigma} + \nabla\times\rho\partial_{\boldsymbol{\alpha}}\Psi)^T\boldsymbol{\alpha}\right] : \mathbf{X} \tag{2.84c}$$

Mechanical equilibrium

$$\nabla\cdot\boldsymbol{\sigma} + \rho\boldsymbol{b}_f = \rho\ddot{\boldsymbol{u}} \tag{2.84d}$$

$$\boldsymbol{\sigma} = \rho\partial_{(\boldsymbol{\varepsilon}-\boldsymbol{\varepsilon}^p)}\Psi \tag{2.84e}$$

Temperature evolution

$$\begin{aligned}
&\left[\left(\nabla\times\rho\partial_{\boldsymbol{\alpha}}\Psi - \rho\theta\partial^2_{\theta(\boldsymbol{\varepsilon}-\boldsymbol{\varepsilon}^p)}\Psi\right) : \boldsymbol{\gamma} - \rho\theta\partial^2_{\theta\theta}\Psi\right]\dot{\theta} + \theta\nabla\times\left(\rho\partial^2_{\boldsymbol{\alpha}\theta}\Psi\dot{\theta}\right) : \boldsymbol{\gamma} \\
&\quad - \rho\left(\partial_{\boldsymbol{\alpha}}\Psi + \theta\partial^2_{\theta\boldsymbol{\alpha}}\Psi\right) : \nabla\times(\boldsymbol{\gamma}\dot{\theta}) + \theta\nabla\times\left[\rho\partial^2_{\boldsymbol{\alpha}(\boldsymbol{\varepsilon}-\boldsymbol{\varepsilon}^p)}\Psi : \boldsymbol{\gamma}\dot{\theta} - \rho\partial^2_{\boldsymbol{\alpha}\boldsymbol{\alpha}}\Psi : \nabla\times(\boldsymbol{\gamma}\dot{\theta})\right] : \boldsymbol{\gamma} \\
&= \boldsymbol{\sigma} : \left(\boldsymbol{\alpha}\times\boldsymbol{v}^d\right) + \rho\theta\partial^2_{\theta(\boldsymbol{\varepsilon}-\boldsymbol{\varepsilon}^p)}\Psi : \dot{\boldsymbol{\varepsilon}}^e - \nabla\cdot\boldsymbol{q} + \rho r \\
&\quad + \left\{\rho(\partial_{\boldsymbol{\alpha}}\Psi - \theta\partial^2_{\theta\boldsymbol{\alpha}}\Psi) : \nabla\times(\boldsymbol{\alpha}\times\boldsymbol{v}^d) + \theta\nabla\times\left[\rho\partial^2_{\boldsymbol{\alpha}\boldsymbol{\alpha}}\Psi : \nabla\times(\boldsymbol{\alpha}\times\boldsymbol{v}^d)\right] : \boldsymbol{\gamma}\right\} \\
&\quad - \theta\nabla\times\left(\rho\partial^2_{\boldsymbol{\alpha}(\boldsymbol{\varepsilon}-\boldsymbol{\varepsilon}^p)}\Psi : \dot{\boldsymbol{\varepsilon}}^e\right) : \boldsymbol{\gamma}
\end{aligned} \tag{2.84f}$$

$$\boldsymbol{q} = -\boldsymbol{K}\nabla\theta. \tag{2.84g}$$

2.5.1 Boundary conditions

Standard displacement and traction boundary conditions on complementary parts of the boundary are necessary to solve for the equilibrium Eq. (2.84d).

To solve for $\boldsymbol{\alpha}$ and θ, the required boundary conditions are similar to Eqs. (2.68) and (2.69).

2.5.2 Initial conditions

Similarly to Section 2.4.8.2, the defect transport Eq. (2.84b) is solved considering a given initial defect density $\boldsymbol{\alpha}_0$, i.e. $\boldsymbol{\alpha}(\boldsymbol{x},0)=\boldsymbol{\alpha}_0(\boldsymbol{x})$.

The balance of linear momentum Eq. (2.84d) requires the specification of an initial displacement and velocity $\boldsymbol{u}_0$ and $\dot{\boldsymbol{u}}_0$, respectively, such that $\boldsymbol{u}(\boldsymbol{x},0)=\boldsymbol{u}_0(\boldsymbol{x})$ and $\dot{\boldsymbol{u}}(\boldsymbol{x},0)=\dot{\boldsymbol{u}}_0(\boldsymbol{x})$.

Furthermore, the temperature evolution Eq. (2.84f) requires the specification of an initial temperature profile in the body, that is, $\theta(\boldsymbol{x},0)=\theta_0(\boldsymbol{x})$ for a given θ_0.

2.6 Some examples for a given Helmholtz free energy density expressions

2.6.1 Finite deformation: Saint-Venant-Kirchoff model with defect core energy

Consider the following expression that models a Saint-Venant-Kirchhoff material and allows for large deformations and temperature changes while specifying a quadratic dislocation core energy term (R. Arora and Acharya, 2020a):

$$\Psi(\boldsymbol{W},\theta,\boldsymbol{\alpha})=\frac{1}{2\rho_0}\boldsymbol{E}:\mathbb{C}:\boldsymbol{E}+c_\varepsilon\left[\Delta\theta-\theta\ln\left(\frac{\theta}{\theta_0}\right)\right]+\frac{\xi}{2\rho_0}\boldsymbol{\alpha}:\boldsymbol{\alpha}, \tag{2.85}$$

where $\boldsymbol{E}=\frac{1}{2}(\boldsymbol{C}^e-\mathbb{1})$ is the Green-Lagrange strain tensor, $\boldsymbol{C}^e=\boldsymbol{W}^{-T}\boldsymbol{W}^{-1}$ is the right Cauchy-Green deformation tensor, and ρ_0 is the mass density for a reference state, $J=\det(\boldsymbol{W}^{-1})$, and ξ is a material constant with dimensions stress$\times$length^2. The expression in Eq. (2.85) captures the stored elastic energy in the first term, the thermal contribution in the second term, and the energy stored in dislocation cores (Acharya, 2010, Acharya and Tartar, 2011) in the third term.

For the Ψ expression in Eq. (2.85), we show the partial derivatives with respect to its arguments in Appendix G. Using these, the set in Eq. (2.67) becomes:

Kinematics and dislocation density evolution

$$\dot{\boldsymbol{W}}+\boldsymbol{W}\boldsymbol{L}=\boldsymbol{\alpha}\times\boldsymbol{v}^d+\boldsymbol{W}\boldsymbol{\gamma}\dot{\theta} \tag{2.86a}$$

$$\mathring{\boldsymbol{\alpha}}=-\nabla\times\left(\boldsymbol{\alpha}\times\boldsymbol{v}^d+\boldsymbol{Y}\dot{\theta}\right),\quad \mathring{\boldsymbol{\alpha}}=\operatorname{tr}(\boldsymbol{L})\boldsymbol{\alpha}+\dot{\boldsymbol{\alpha}}-\boldsymbol{\alpha}\boldsymbol{L}^T \tag{2.86b}$$

$$\boldsymbol{v}^d=\frac{1}{B}\left\{\left[\boldsymbol{\sigma}_H+\xi\left(\nabla\times\frac{\rho}{\rho_0}\boldsymbol{\alpha}\right)^T\boldsymbol{W}\right]\boldsymbol{W}^{-1}\boldsymbol{\alpha}\right\}:\mathbf{X} \tag{2.86c}$$

Mass density evolution

$$\dot{\rho}+\nabla\cdot(\rho\boldsymbol{v})=0 \tag{2.86d}$$

Mechanical equilibrium

$$\nabla \cdot \boldsymbol{\sigma} + \rho \boldsymbol{b}_f = \rho \dot{\boldsymbol{v}} \tag{2.86e}$$

$$\boldsymbol{\sigma} = \frac{\rho}{\rho_0} \boldsymbol{W}^{-1} (\mathbb{C} : \boldsymbol{E}) \boldsymbol{W}^{-T} + \frac{\rho}{\rho_0} \xi \left[\boldsymbol{\alpha}^T \boldsymbol{\alpha} - \left(\boldsymbol{\alpha} : \boldsymbol{\alpha} \right) \mathbb{1} \right] \tag{2.86f}$$

Temperature evolution

$$\begin{aligned}
&\left\{ \left[\xi \nabla \times \frac{\rho}{\rho_0} \boldsymbol{\alpha} (\mathbb{1} + \theta \boldsymbol{\gamma}^T) - \rho \theta \boldsymbol{W} \boldsymbol{\gamma} : \mathbb{A} - \theta \boldsymbol{W}^{-T} \boldsymbol{\sigma}_H \boldsymbol{\gamma}^T - \theta (\boldsymbol{W}^{-T} \boldsymbol{\sigma}_H - \xi \nabla \times \frac{\rho}{\rho_0} \boldsymbol{\alpha}) : \boldsymbol{W} \mathbb{G} \right] : \boldsymbol{W} \boldsymbol{\gamma} \right. \\
&\qquad \left. + \rho c_\varepsilon \right\} \dot{\theta} - \xi \frac{\rho}{\rho_0} \boldsymbol{\alpha} : \nabla \times \left(\boldsymbol{W} \boldsymbol{\gamma} \dot{\theta} \right) - \xi \theta \nabla \times \left[\frac{\rho}{\rho_0} \mathrm{tr} \left(\nabla \times \left(\boldsymbol{W} \boldsymbol{\gamma} \dot{\theta} \right) \right) \mathbb{1} \right] : \boldsymbol{W} \boldsymbol{\gamma} \\
&= -\nabla \cdot \boldsymbol{q} + \rho r + \left[\boldsymbol{W}^{-T} \boldsymbol{\sigma}_H \left(\mathbb{1} - \theta \boldsymbol{\gamma}^T \right) - \theta \left(\boldsymbol{W}^{-T} \boldsymbol{\sigma}_H + \xi \nabla \times \frac{\rho}{\rho_0} \boldsymbol{\alpha} \right) : \boldsymbol{W} \mathbb{G} - \xi \theta \nabla \times \left(\frac{\rho}{\rho_0} \boldsymbol{\alpha} \right) \boldsymbol{\gamma}^T \right. \\
&\qquad \left. + \rho \theta \boldsymbol{W} \boldsymbol{\gamma} : \mathbb{A} \right] : \left(\boldsymbol{\alpha} \times \boldsymbol{v}^d \right) + \left\{ - \rho \theta \boldsymbol{W}^T (\boldsymbol{W} \boldsymbol{\gamma} : \mathbb{A}) + \theta \left[\boldsymbol{\sigma}_H \boldsymbol{\gamma}^T + \xi \boldsymbol{W}^T \nabla \times \left(\frac{\rho}{\rho_0} \boldsymbol{\alpha} \right) \boldsymbol{\gamma}^T \right. \right. \\
&\qquad \left. \left. + \left(\boldsymbol{\sigma}_H + \xi \boldsymbol{W}^T \nabla \times \frac{\rho}{\rho_0} \boldsymbol{\alpha} \right) : \boldsymbol{W} \mathbb{G} \right] \right\} : \boldsymbol{L} + \xi \frac{\rho}{\rho_0} \boldsymbol{\alpha} : \nabla \times \left(\boldsymbol{\alpha} \times \boldsymbol{v}^d \right) \\
&\quad + \left\{ \xi \theta \frac{\dot{\rho}}{\rho} \nabla \times \frac{\rho}{\rho_0} \boldsymbol{\alpha} - \theta \nabla \times \left[\xi \frac{\dot{\rho}}{\rho_0} \boldsymbol{\alpha} - \xi \frac{\rho}{\rho_0} \mathrm{tr} \Big(\mathrm{tr}(\boldsymbol{L}) \boldsymbol{\alpha} - \boldsymbol{\alpha} \boldsymbol{L}^T + \nabla \times (\boldsymbol{\alpha} \times \boldsymbol{v}^d) \Big) \mathbb{1} \right] \right. \\
&\qquad \left. - \xi \theta \left[\nabla \left(\frac{\rho}{\rho_0} \boldsymbol{\alpha} \right) \boldsymbol{L} \right] : \mathbf{X} \right\} : \boldsymbol{W} \boldsymbol{\gamma}
\end{aligned} \tag{2.86g}$$

$$\boldsymbol{q} = -\boldsymbol{K} \nabla \theta, \tag{2.86h}$$

where $\boldsymbol{\sigma}_H$ is given by Eq. (G.2) and $\mathbb{A} := \partial^2_{\boldsymbol{W}\boldsymbol{W}} \Psi$ by Eq. (G.3).

2.6.2 Small deformation: Saint-Venant-Kirchoff model with defect core energy

Considering Eq. (2.70), we take the same expression for Ψ from Section 2.6, which then becomes

$$\Psi(\boldsymbol{\varepsilon}^e, \theta, \boldsymbol{\alpha}) = \frac{1}{2\rho_0} \boldsymbol{\varepsilon}^e : \mathbb{C} : \boldsymbol{\varepsilon}^e + c_\varepsilon \left[\Delta\theta - \theta \ln \left(\frac{\theta}{\theta_0} \right) \right] + \frac{\xi}{2\rho_0} \boldsymbol{\alpha} : \boldsymbol{\alpha}. \tag{2.87}$$

From Eq. (2.72), we have that

$$\boldsymbol{\varepsilon}^e = \boldsymbol{\varepsilon} - \boldsymbol{\varepsilon}^p - \boldsymbol{\varepsilon}^\theta$$

such that we can write Eq. (2.87) as

$$\Psi(\boldsymbol{\varepsilon}-\boldsymbol{\varepsilon}^p,\theta,\boldsymbol{\alpha})=\frac{1}{2\rho_0}(\boldsymbol{\varepsilon}-\boldsymbol{\varepsilon}^p):\mathbb{C}:(\boldsymbol{\varepsilon}-\boldsymbol{\varepsilon}^p)-\frac{\Delta\theta}{\rho_0}\boldsymbol{\beta}:(\boldsymbol{\varepsilon}-\boldsymbol{\varepsilon}^p)+c_\varepsilon\left[\Delta\theta-\theta\ln\left(\frac{\theta}{\theta_0}\right)\right]+\frac{\xi}{2\rho_0}\boldsymbol{\alpha}:\boldsymbol{\alpha}, \tag{2.88}$$

where $\boldsymbol{\beta}:=\mathbb{C}:\boldsymbol{\gamma}$, and the term in $(\Delta\theta)^2$ is neglected, the thermal contribution to Ψ being considered in the third term on the right-hand side. Using Eqs. (2.77a), (E.11) and (G.6), we write the constitutive equation for the stress tensor as

$$\boldsymbol{\sigma}=\mathbb{C}:(\boldsymbol{\varepsilon}-\boldsymbol{\varepsilon}^p)-\Delta\theta\boldsymbol{\beta}:(\boldsymbol{\varepsilon}-\boldsymbol{\varepsilon}^p) \tag{2.89}$$

The constitutive expression for the dislocation velocity is given by Eqs. (2.77c) and (G.4):

$$\boldsymbol{v}^d=\frac{1}{B}\left\{\left[\boldsymbol{\sigma}+\xi(\nabla\times\boldsymbol{\alpha})^T\right]\boldsymbol{\alpha}\right\}:\mathbf{X}. \tag{2.90}$$

Kinematics and dislocation density evolution

$$\dot{\boldsymbol{U}}^e=\nabla\dot{\boldsymbol{u}}-\boldsymbol{\alpha}\times\boldsymbol{v}^d-\boldsymbol{\gamma}\dot{\theta} \tag{2.91a}$$

$$\dot{\boldsymbol{\alpha}}=-\nabla\times\left(\boldsymbol{\alpha}\times\boldsymbol{v}^d+\boldsymbol{\gamma}\dot{\theta}\right) \tag{2.91b}$$

$$\boldsymbol{v}^d=\frac{1}{B}\left\{\left[\boldsymbol{\sigma}+\xi(\nabla\times\boldsymbol{\alpha})^T\right]\boldsymbol{\alpha}\right\}:\mathbf{X} \tag{2.91c}$$

Mechanical equilibrium

$$\nabla\cdot\boldsymbol{\sigma}+\rho\boldsymbol{b}_f=\rho\ddot{\boldsymbol{u}} \tag{2.91d}$$

$$\boldsymbol{\sigma}=\mathbb{C}:(\boldsymbol{\varepsilon}-\boldsymbol{\varepsilon}^p)-\Delta\theta\boldsymbol{\beta}:(\boldsymbol{\varepsilon}-\boldsymbol{\varepsilon}^p)=\mathbb{C}:[\nabla(\boldsymbol{u}-\boldsymbol{z})+\boldsymbol{\zeta}] \tag{2.91e}$$

Temperature evolution

$$\begin{aligned}&\left[(\xi\nabla\times\boldsymbol{\alpha}+\theta\boldsymbol{\beta}):\boldsymbol{\gamma}+\rho c_\varepsilon\right]\dot{\theta}-\xi\boldsymbol{\alpha}:\nabla\times(\boldsymbol{\gamma}\dot{\theta})-\xi\theta\nabla\times\left[\mathrm{tr}\left(\nabla\times\left(\boldsymbol{\gamma}\dot{\theta}\right)\right)\mathbb{1}\right]:\boldsymbol{\gamma}\\&\quad=\boldsymbol{\sigma}:(\boldsymbol{\alpha}\times\boldsymbol{v}^d)-\theta\boldsymbol{\beta}:\dot{\boldsymbol{\varepsilon}}^e-\nabla\cdot\boldsymbol{q}+\rho r+\xi\boldsymbol{\alpha}:\nabla\times\left(\boldsymbol{\alpha}\times\boldsymbol{v}^d\right)\\&\qquad+\xi\theta\nabla\times\left[\mathrm{tr}\left(\nabla\times\left(\boldsymbol{\alpha}\times\boldsymbol{v}^d\right)\right)\mathbb{1}\right]:\boldsymbol{\gamma}\end{aligned} \tag{2.91f}$$

$$\boldsymbol{q}=-\boldsymbol{K}\nabla\theta. \tag{2.91g}$$

2.6.3 Comparison with the model proposed by Upadhyay, 2020

In Eq. (2.75), the term $\dot{\boldsymbol{\alpha}}^p = -\nabla\times(\boldsymbol{\alpha}\times\boldsymbol{v}^d)$ represents the evolution of the line-character of the thermomechanical defect and is directly associated with the evolution of the dislocation ensemble with velocity $\boldsymbol{v}^d$. On the other hand, $\boldsymbol{S}^\theta = -\nabla\times(\boldsymbol{\gamma}\dot{\theta})$ contains the contribution of the incompatibility of the transient temperature field to the evolution of the defect character (Burgers vector). The evolution statement in Eq. (2.75) is similar to the one derived in Upadhyay, 2020 (Eq. 3.25_3). However, a notable difference lies in the equation for $\dot{\boldsymbol{\alpha}}^p$. In Upadhyay, 2020, $\boldsymbol{\alpha}^p$ was introduced as being the density of dislocation lines in the body, independent of the areal density $\boldsymbol{S}^\theta$ (defined there as $\boldsymbol{\alpha}^\theta$), and thus its evolution was given by $\dot{\boldsymbol{\alpha}}^p = -\nabla\times(\boldsymbol{\alpha}^p\times\boldsymbol{v}^d)$. In this work, in $\dot{\boldsymbol{\alpha}}^p$ the whole thermomechanical defect $\boldsymbol{\alpha}$ is transported with velocity $\boldsymbol{v}^d$, while $\boldsymbol{S}^\theta$ acts as a source term for $\boldsymbol{\alpha}$, i.e., there is no clear separation between a dislocation line and a "thermal" line-type defect. Such a description seems to be better suited to describe the dislocation density state in a body involving transient thermal gradients since an experimental observation of this state could not allow for a clear distinction of the contribution due to thermal effects.

In Upadhyay, 2020, the total strain tensor was additively decomposed into a sum of elastic, plastic, and thermal parts, as $\boldsymbol{\varepsilon} = \boldsymbol{\varepsilon}^e + \boldsymbol{\varepsilon}^p + \boldsymbol{\varepsilon}^\theta$, with $\boldsymbol{\varepsilon}^\theta = \boldsymbol{\gamma}\Delta\theta$. The Helmholtz free energy was taken as $\hat{\Psi} = \hat{\Psi}(\boldsymbol{\varepsilon}^e) \equiv \hat{\Psi}(\boldsymbol{\varepsilon} - \boldsymbol{\varepsilon}^p, \theta)$, such that the dependence of Ψ on internal variables, such as $\boldsymbol{\alpha}$, was not studied. To establish a comparison, we consider the same expression for $\hat{\Psi}$, i.e.

$$\hat{\Psi}(\boldsymbol{\varepsilon}-\boldsymbol{\varepsilon}^p,\theta) = \frac{1}{2\rho_0}(\boldsymbol{\varepsilon}-\boldsymbol{\varepsilon}^p) : \mathbb{C} : (\boldsymbol{\varepsilon}-\boldsymbol{\varepsilon}^p) - \frac{\Delta\theta}{\rho_0}\boldsymbol{\beta} : (\boldsymbol{\varepsilon}-\boldsymbol{\varepsilon}^p) + c_\varepsilon\left[\Delta\theta - \theta\ln\left(\frac{\theta}{\theta_0}\right)\right], \quad (2.92)$$

such that the dissipation can be written from Eq. (2.37)

$$D := \int_{\Omega_t}\left[-\rho\left(\partial_{(\boldsymbol{\varepsilon}-\boldsymbol{\varepsilon}^p)}\hat{\Psi} : (\dot{\boldsymbol{\varepsilon}}-\dot{\boldsymbol{\varepsilon}}^p) + \partial_\theta\hat{\Psi}\,\dot{\theta} + \eta\dot{\theta}\right) - \frac{1}{\theta}\boldsymbol{q}\cdot\nabla\theta + \boldsymbol{\sigma} : \boldsymbol{L}\right]\mathrm{d}v \geq 0. \quad (2.93)$$

Noting that $\boldsymbol{\sigma} : \boldsymbol{L} = \boldsymbol{\sigma} : \dot{\boldsymbol{\varepsilon}}$, we arrive at the following constitutive relations based on Eq. (2.93)

$$\boldsymbol{\sigma} = \rho\partial_{(\boldsymbol{\varepsilon}-\boldsymbol{\varepsilon}^p)}\hat{\Psi} \quad (2.94a)$$

$$\eta = -\partial_\theta\hat{\Psi} \quad (2.94b)$$

$$\boldsymbol{v}^d = \frac{1}{B}(\boldsymbol{\sigma}\boldsymbol{\alpha}) : \mathbf{X} \quad (2.94c)$$

$$\boldsymbol{q} = -\boldsymbol{K}\nabla\theta, \quad (2.94d)$$

which corresponds to what was obtained in Upadhyay, 2020. Note that, in our model, we do not explicitly introduce a plastic distortion tensor. Instead, plasticity arises from the motion and generation of dislocations, which could be expressed in terms of a plastic (slip) distortion rate in the form $\dot{\boldsymbol{U}}^p = \boldsymbol{\alpha}\times\boldsymbol{v}^d$ from Eq. (2.71). We have that $\boldsymbol{\sigma} : \dot{\boldsymbol{U}}^p = \boldsymbol{\sigma} : \dot{\boldsymbol{\varepsilon}}^p = \boldsymbol{\sigma} : (\boldsymbol{\alpha}\times\boldsymbol{v}^d)$, which leads to the definition in Eq. (2.94c).

From Eq. (2.94b), we have

$$\dot{\eta} = -\partial^2_{\theta(\boldsymbol{\varepsilon}-\boldsymbol{\varepsilon}^p)}\hat{\Psi} : (\dot{\boldsymbol{\varepsilon}} - \dot{\boldsymbol{\varepsilon}}^p) - \partial^2_{\theta\theta}\hat{\Psi}\dot{\theta},$$

with which, by following a similar procedure from Section 2.4.6, the temperature evolution equation is obtained as

$$-\rho\theta\partial^2_{\theta\theta}\hat{\Psi}\dot{\theta} = -\nabla\cdot\boldsymbol{q} + \rho\theta\partial^2_{\theta(\boldsymbol{\varepsilon}-\boldsymbol{\varepsilon}^p)}\hat{\Psi} : (\dot{\boldsymbol{\varepsilon}} - \dot{\boldsymbol{\varepsilon}}^p) + \boldsymbol{\sigma} : \dot{\boldsymbol{\varepsilon}}^p + \rho r. \tag{2.95}$$

Considering the expression in Eq. (2.92), we get

$$\rho c_{\varepsilon}\dot{\theta} = -\nabla\cdot\boldsymbol{q} - \theta\boldsymbol{\beta} : (\dot{\boldsymbol{\varepsilon}} - \dot{\boldsymbol{\varepsilon}}^p) + \boldsymbol{\sigma} : \dot{\boldsymbol{\varepsilon}}^p + \rho r. \tag{2.96}$$

The equation set of the model in this case is

$$\boldsymbol{\varepsilon}^e = \boldsymbol{\varepsilon} - \boldsymbol{\varepsilon}^p - \boldsymbol{\varepsilon}^\theta \tag{2.97a}$$
$$\dot{\boldsymbol{\alpha}} = -\nabla\times\left(\boldsymbol{\alpha}\times\boldsymbol{v}^d + \boldsymbol{\gamma}\dot{\theta}\right) \tag{2.97b}$$
$$\boldsymbol{v}^d = \frac{1}{B}(\boldsymbol{\sigma}\boldsymbol{\alpha}) : \mathbf{X} \tag{2.97c}$$
$$\nabla\cdot\boldsymbol{\sigma} = \rho\ddot{\boldsymbol{u}} \tag{2.97d}$$
$$\boldsymbol{\sigma} = \mathbb{C} : (\boldsymbol{\varepsilon} - \boldsymbol{\varepsilon}^p) - \boldsymbol{\beta}\Delta\theta \tag{2.97e}$$
$$\rho c_{\varepsilon}\dot{\theta} = -\nabla\cdot\boldsymbol{q} - \theta\boldsymbol{\beta} : (\dot{\boldsymbol{\varepsilon}} - \dot{\boldsymbol{\varepsilon}}^p) + \boldsymbol{\sigma} : \dot{\boldsymbol{\varepsilon}}^p + \rho r, \tag{2.97f}$$

and is completed with the boundary and initial conditions in Sections 2.5.1 and 2.5.2. Hence, under a similar assumption of the form of Ψ, the present model reduces to the theory proposed in Upadhyay, 2020. The main difference stems from the additive decomposition of the strain tensor into elastic, plastic and thermal parts in the latter, leading to the introduction of the areal densities $\boldsymbol{\alpha}^p$ and $\boldsymbol{\alpha}^\theta$ which are independent of each other, as mentioned at the beginning of this section. From this definition, each density has its evolution statement, with $\dot{\boldsymbol{\alpha}}^\theta = -\nabla\times(\dot{\overline{\boldsymbol{\gamma}\theta}})$. In the present model, however, without considering a multiplicative decomposition of the deformation gradient, which lies in the introduction of thermal and plastic distortion tensors, the evolution of the thermomechanical defect density (Eq. (2.97b)) comprises both thermal and dislocation line slip effects, without distinction, due to an indistinguishable contribution of thermal gradients and dislocation lines to the incompatibility in $\boldsymbol{W}$ (Eq. (2.17)).

2.7 Conclusion

In this work, a fully nonlinear model of field dislocations thermomechanics is proposed. The motivation behind its development arose from the need for a continuum framework capable of computing the evolution of dislocations based on a physical conservation argument under any thermomechanical boundary conditions while allowing for large deformations. It expands on previous work on the isothermal field dislocation mechanics model (Acharya, 2001, Acharya,

2004, R. Arora et al., 2020) and the small-strain thermal field dislocation mechanics with its numerical implementation (Upadhyay, 2020, Lima-Chaves and Upadhyay, 2024).

Although not adopting the standard multiplicative decomposition of the deformation gradient into multiple components, as is customary in elastoplasticity models, the additive decomposition of the velocity gradient into elastic, plastic, and thermal parts is recovered, purely as a result of the conservation of the Burgers vector (Acharya and Zhang, 2015), from which the evolution statement for the dislocation density tensor is also derived. Based on the standard conservation laws from continuum mechanics (mass, linear and angular momenta, and energy), the remaining governing equations are presented.

A central point of the model is the kinematical assumption of the contribution of a transient heterogeneous temperature field as a source term to the evolution of the thermomechanical defect character (which comprises dislocations and a line-type defect that arises through the incompatibility in thermal strains). Considering a Helmholtz free energy density Ψ dependent on the inverse elastic distortion tensor $\boldsymbol{W}$, temperature θ and thermomechanical defect density $\boldsymbol{\alpha}$, it is shown that the resulting expression of the fraction of plastic work converted into heat (Eq. (2.65)) is a function of the material type and strain rates. This fraction was introduced in the experimental work of Taylor and Quinney, 1934, and has been shown to depend on the material type and the loading conditions (Rittel et al., 2017), with such dependence emerging in the present model as a consequence of the evolution of the thermomechanical defect density obtained from the conservation of the Burgers vector. Moreover, the temperature evolution equation is shown to allow for solutions in the form of dispersive waves with finite propagation speed, despite using Fourier's law of heat conduction as the constitutive assumption of the heat flux vector. Well-posedness of the equation is shown in a linearised setting. Along with the expected decay for a range of wavenumbers, the solution also admits well-posed growth, which can be the source of spatial patterning resulting from the growth of some Fourier components.

Considering Ψ for a Saint-Venant-Kirchhoff material, the set of fully coupled equations of the model is presented. A linearisation of the model is also shown, which allows a comparison with the small deformation theory presented in Upadhyay, 2020. The main difference is shown to come from the additive decomposition of the strain tensor in that work into elastic, plastic, and thermal parts, which results in separate evolution statements for dislocations $\dot{\boldsymbol{\alpha}}^p$ and "thermal" defects $\dot{\boldsymbol{\alpha}}^\theta$. The present framework, however, by not explicitly introducing a plastic distortion tensor, upon linearization results in a single expression for the thermomechanical defect density $\dot{\boldsymbol{\alpha}}$ (Eq. (2.97b)) that comprises both dislocation line evolution and thermal effects.

Prospective work includes the numerical implementation of the proposed model in a finite element framework to (i) study the model capabilities, (ii) verify the approach through comparison with experimentally-obtained conversion rates of plastic work into heat (e.g. in Nieto-Fuentes et al., 2018, Rittel et al., 2017) during deformation, and (iii) apply the theory to study dislocation thermomechanics under extreme processing conditions, as in the context of metal additive manufacturing.

3 Finite element implementation of the small deformation TFDM

In this chapter, the finite element approximation of TFDM is discussed. This work was published in Lima-Chaves and Upadhyay, 2024, from which the following content is extracted.

3.1 Abstract

The small deformation formulation of the thermal field dislocation mechanics model (Upadhyay, 2020) is numerically implemented using the finite element method. The implementation consists of solving a first-order div-curl system to obtain an incompatible plastic distortion from a prescribed polar dislocation density along with three governing partial differential equations (PDE): the dislocation transport equation (a first-order hyperbolic PDE), the static equilibrium equation (an elliptic PDE), and the temperature evolution equation (a parabolic PDE). A combination of continuous Galerkin (for the elliptic and parabolic PDEs) and discontinuous Galerkin (for the hyperbolic PDE) space discretizations and Runge-Kutta time discretizations are used to implement these equations in a staggered algorithm and obtain stable solutions at (quasi-)optimal convergence rates. The implementation is verified by comparing the simulation-predicted temperature evolution of a moving edge dislocation with an analytical solution. Next, the contribution of plastic dissipation and thermoelastic effect to the temperature evolution during the motion of an edge and a screw dislocation, annihilation of two edge dislocations and expansion of a dislocation loop are studied in detail. In the case of a moving edge dislocation, contrary to existing literature, the thermoelastic effect is demonstrated to have a more significant contribution to temperature evolution than plastic dissipation for the studied traction boundary condition and dislocation velocity expression. In the dislocation loop expansion case, the role of free surfaces on temperature evolution is highlighted. As the loop approaches the free surfaces, plastic dissipation is found to have an increasing contribution to temperature evolution due to the growing impact of image stresses.

3.2 Introduction

The thermal field dislocation mechanics (TFDM) model (Upadhyay, 2020) is a fully coupled dislocation thermomechanics model designed in a small deformation setting to study dislocation evolution under any thermomechanical boundary conditions. TFDM finds its roots in the isothermal field dislocation mechanics (FDM) (Acharya, 2001, Acharya, 2003), which is a thermodynamically rigorous model capable of predicting internal stresses due to dislocations, dislocation annihilation, dislocation dynamics in the presence of inertia, considering nonlinear elasticity and/or elastic anisotropy. FDM itself is based on previous works on continuously distributed dislocations (Mura, 1963, Willis, 1967, Kosevich, 1979). TFDM is able to tackle the aforementioned problems and go beyond the scope of FDM to solve the fully coupled thermomechanical initial boundary value problem with the particular aim of studying those processes that induce strong temperature gradients and heating/cooling rates, such as metal additive manufacturing, welding, quenching, etc.

This paper aims to propose a numerical implementation of the TFDM model using the finite element method (FEM), verify it and present some applications. In the TFDM model, the elastic/plastic incompatibility introduced by a prescribed polar dislocation density is expressed by a first-order div-curl system, which is solved using a least squares finite element method (LSFEM) proposed in Roy and Acharya, 2005 and further employed in Roy and Acharya, 2006 and R. Arora et al., 2020. This approach avoids the issue of having more equations than unknowns when using the conventional continuous Galerkin approach. The static equilibrium equation is an elliptic PDE that is solved by a continuous Galerkin (CG) approximation (Roy and Acharya, 2005). At the core of the model lies the dislocation transport equation, which is a first-order hyperbolic advection-reaction-type PDE (more generally, it is a first-order transport equation, which may not remain hyperbolic in some simpler situations, e.g., in Acharya and Tartar, 2011), arising from the statement of conservation of Burgers vector (see Acharya, 2011). Different approaches to solve this equation can be found in the literature, for instance, a 3D weighted CG/LSFEM scheme (Varadhan et al., 2006), a 3D fast Fourier transform approach with spectral filters (Djaka et al., 2015) and a 2D high-resolution Godunov-type solver scheme (Morin et al., 2019). However, the hyperbolic nature of this PDE leads to solutions for the dislocation density that present discontinuities, hence, discontinuous function spaces are better suited to approximate the solution than continuous approaches. In this regard, Upadhyay and Bleyer, 2021 proposed a time-explicit 3-dimensional Runge-Kutta discontinuous Galerkin (RKDG) scheme that allows for stable dislocation transport with (quasi)-optimal convergence rates, and is the adopted approach in this work. The temperature evolution equation is a parabolic PDE and is solved using a semi-implicit time discretization and a CG space discretization. Owing to the coupled character of the model, in which the stress state and the dislocation activity contribute as heat sources for the temperature evolution of the body, the thermoelastic effect and the plastic dissipation due to dislocation motion are considered when computing the temperature field. To avoid dealing with many degrees of freedom in a monolithic scheme, the FE implementation of these equations is done using a staggered approach.

The structure of this paper is the following: the TFDM model is briefly described in Section 3.3; the approximation of the model using the FEM is described in Section 3.4, in which an algorithm is also proposed; in Section 3.5, the main results of this work are discussed, including the comparison of the model-predicted temperature evolution with the one obtained from an analytical solution; then, the temperature profiles generated by the motion of an edge and a screw dislocation, dislocation annihilation and loop expansion are studied in detail; the concluding remarks are presented in Section 3.6.

3.3 The TFDM model

In the following, the governing equations and the initial and boundary conditions of the TFDM model (Upadhyay, 2020) are briefly recalled, followed by a non-dimensionalization of the problem.

3.3.1 Field equations of TFDM

Consider a simply connected body $\Omega \subset \mathcal{E}^3$, where $\mathcal{E}^3$ is the three-dimensional Euclidean point space, whose boundary is $\partial\Omega$. A small deformation hypothesis is considered and the model is assumed to operate at the length scale where individual line defects can be distinguished. In this setting, the equation set of the TFDM model is[1] (Upadhyay, 2020):

$$\boldsymbol{U}^p = \nabla \boldsymbol{z}^p + \boldsymbol{\chi}^p \quad \text{in} \quad \Omega \times [0, t_F] \tag{3.1a}$$
$$\boldsymbol{\alpha}^p = -\nabla \times \boldsymbol{\chi}^p \quad \text{in} \quad \Omega \times [0, t_F] \tag{3.1b}$$
$$\nabla \cdot \boldsymbol{\chi}^p = 0 \quad \text{in} \quad \Omega \times [0, t_F] \tag{3.1c}$$
$$\nabla \cdot \nabla \dot{\boldsymbol{z}}^p = \nabla \cdot (\boldsymbol{\alpha}^p \times \boldsymbol{v}) \quad \text{in} \quad \Omega \times (0, t_F] \tag{3.1d}$$
$$\dot{\boldsymbol{U}}^p = \boldsymbol{\alpha}^p \times \boldsymbol{v} \quad \text{in} \quad \Omega \times [0, t_F] \tag{3.1e}$$
$$\dot{\boldsymbol{\alpha}}^p = -\nabla \times (\boldsymbol{\alpha}^p \times \boldsymbol{v}) \quad \text{in} \quad \Omega \times (0, t_F] \tag{3.1f}$$
$$\boldsymbol{v} = \frac{1}{B}\boldsymbol{f} \quad \text{in} \quad \Omega \times [0, t_F] \tag{3.1g}$$

$$\nabla \cdot \boldsymbol{\sigma} = 0 \quad \text{in} \quad \Omega \times [0, t_F] \tag{3.1h}$$
$$\boldsymbol{\sigma} = \mathbb{C} : (\nabla \boldsymbol{u} - \boldsymbol{U}^p) - \boldsymbol{\beta}\Delta\theta \quad \text{in} \quad \Omega \times [0, t_F] \tag{3.1i}$$

$$\rho c_\varepsilon \dot{\theta} = -\nabla \cdot \boldsymbol{q} + \boldsymbol{\sigma} : \dot{\boldsymbol{U}}^p - \theta\boldsymbol{\beta} : (\nabla \dot{\boldsymbol{u}} - \dot{\boldsymbol{U}}^p) + \rho r \quad \text{in} \quad \Omega \times (0, t_F] \tag{3.1j}$$
$$\boldsymbol{q} = -\boldsymbol{K}\nabla\theta \quad \text{in} \quad \Omega \times [0, t_F], \tag{3.1k}$$

where t_F is the total simulation time. The first set of Equations (3.1a) to (3.1g) are the kinematic equations of the model. The Stokes-Helmholtz decomposition is used in Eq. (3.1a) to uniquely decompose the plastic distortion tensor $\boldsymbol{U}^p$ into the sum of a compatible ($\nabla \boldsymbol{z}^p$, curl-free) and an

[1] The mathematical notation used is shown in Appendix A

incompatible ($\boldsymbol{\chi}^p$, divergence-free) part (Acharya and Roy, 2006). Eq. (3.1b) expresses the plastic incompatibility due to the presence of dislocations through a geometry statement. Together with Eq. (3.1c), these equations allow for the unique determination of $\boldsymbol{\chi}^p$ given the polar dislocation density tensor $\boldsymbol{\alpha}^p$, and ensure that $\boldsymbol{\chi}^p = 0$ whenever $\boldsymbol{\alpha}^p = 0$. Eq. (3.1g) is a constitutive relationship for the dislocation velocity field $\boldsymbol{v}$ as a function of its driving force $\boldsymbol{f} = (\boldsymbol{\sigma}\boldsymbol{\alpha}^p) : \mathbf{X}$, where $\boldsymbol{\sigma}$ is the Cauchy stress tensor, and $1/\boldsymbol{B}$ is the dislocation mobility coefficient. In the case of a single dislocation, $\boldsymbol{f}$ reduces to the Peach-Koehler force exerted on a dislocation line (Peach and Koehler, 1950). Eq. (3.1d) gives the evolution of the compatible part of the plastic distortion tensor, which stores the information of the plastic deformation history from the start of the simulation. Eq. (3.1e) accounts for the plastic slip distortion in the body due to dislocation motion. Eq. (3.1f) arises from the conservation of Burgers vector in the body (see Acharya, 2011). It represents the transport of dislocation lines and naturally accounts for dislocation annihilation. The conservation of the Burgers vector results in the Nye's tensor $\boldsymbol{\alpha} = \boldsymbol{\alpha}^p + \boldsymbol{\alpha}^\theta$ (Upadhyay, 2020). In this relation, $\boldsymbol{\alpha}^\theta$ is the thermal defect density tensor, which arises due to incompatibilities in the thermal strain field ($\boldsymbol{\epsilon}^\theta := \boldsymbol{\gamma}\Delta\theta$), and is defined as $\boldsymbol{\alpha}^\theta := -\nabla \times (\boldsymbol{\gamma}\Delta\theta)$, where $\boldsymbol{\gamma}$ is the positive-definite thermal expansion tensor (considered isotropic in this work i.e., $\boldsymbol{\gamma} = \gamma\mathbb{1}$) and $\Delta\theta = \theta - \theta_0$ is the temperature field deviation from a reference temperature θ_0. The outcomes of this decomposition of Nye's tensor are not explored in the present work.

The governing equation Eq. (3.1h) is the static mechanical equilibrium equation neglecting body forces. Eq. (3.1i) is the Neumann-Duhamel's constitutive equation for $\boldsymbol{\sigma}$ in thermoelasticity, which reduces to the 3D Hooke's law under isothermal condition at θ_0. $\mathbb{C}$ is the fourth-order stiffness tensor, which, considering isotropic elasticity, is expressed as $\mathbb{C}_{ijkl} = \lambda\delta_{ij}\delta_{kl} + \mu(\delta_{ik}\delta_{jl} + \delta_{il}\delta_{jk})$, where λ and μ are the first and second Lamé parameters, respectively; note that the model and its numerical implementation are capable of handling anisotropic elasticity without any changes to the implementation. $\boldsymbol{u}$ is the total displacement vector, and $\boldsymbol{\beta} = \mathbb{C} : \boldsymbol{\gamma}$ is the second-order thermal moduli tensor.

Finally, the conservation of energy expressed by the first law of thermodynamics gives rise to the temperature evolution governing Eq. (3.1j). It is coupled with dislocation activity and elasticity through the second and third terms on the right-hand side, respectively. ρ is the material density, c_ε is the specific heat capacity at constant strain, $\boldsymbol{q}$ is the heat flux vector, and r is an internal heat source term. The heat flux $\boldsymbol{q}$ is constitutively specified through the generalized Fourier's law in Eq. (3.1k), where $\boldsymbol{K}$ is the second order thermal conductivity tensor. All the material properties are temperature-dependent. Note that the constitutive relations of the TFDM model are deduced from material frame indifference and the requirement that the global dissipation rate D is non-negative, where D is expressed as

$$D = \int_\Omega \boldsymbol{\sigma} : \dot{\boldsymbol{U}}^p \, dV - \int_\Omega \frac{1}{\theta}(\boldsymbol{q} \cdot \nabla\theta) \, dV \geq 0. \tag{3.2}$$

3.3.2 Boundary and initial conditions

The theory is closed with the prescription of initial and boundary conditions (BCs) for the fields in Eq. (3.1). The BCs are given as follows:

$$\boldsymbol{\chi}^p \hat{\boldsymbol{n}} = 0 \quad \text{on} \quad \partial\Omega \times [0, t_F] \tag{3.3a}$$
$$(\nabla \dot{\boldsymbol{z}}^p - \boldsymbol{\alpha}^p \times \boldsymbol{v}) \hat{\boldsymbol{n}} = 0 \quad \text{on} \quad \partial\Omega \times (0, t_F] \tag{3.3b}$$
$$(\boldsymbol{v} \cdot \hat{\boldsymbol{n}})\, \boldsymbol{\alpha}^p = 0 \quad \text{on} \quad \partial\Omega^- \times (0, t_F] \tag{3.3c}$$

$$\boldsymbol{u} = \bar{\boldsymbol{u}} \quad \text{on} \quad \partial\Omega^u \times [0, t_F] \tag{3.3d}$$
$$\boldsymbol{\sigma} \hat{\boldsymbol{n}} = \bar{\boldsymbol{t}} \quad \text{on} \quad \partial\Omega^t \times [0, t_F] \tag{3.3e}$$

$$\theta = \bar{\theta} \quad \text{on} \quad \partial\Omega^\theta \times [0, t_F] \tag{3.3f}$$
$$\boldsymbol{q} \cdot \hat{\boldsymbol{n}} = \bar{q} \quad \text{on} \quad \partial\Omega^q \times [0, t_F], \tag{3.3g}$$

where $\partial\Omega^u \cup \partial\Omega^t = \partial\Omega$, $\partial\Omega^u \cap \partial\Omega^t = \emptyset$, $\partial\Omega^\theta \cup \partial\Omega^q = \partial\Omega$ and $\partial\Omega^\theta \cap \partial\Omega^q = \emptyset$. The overbars in Equations (3.3d) to (3.3g) indicate prescribed values. Equations (3.3a) and (3.3b) allow for the unique determination of the plastic distortion tensor $\boldsymbol{U}^p$ given $\boldsymbol{\alpha}^p$ and $\boldsymbol{v}$. In Eq. (3.3c), $\partial\Omega^-$ represents the inflow part of $\partial\Omega$, for which $\boldsymbol{v} \cdot \hat{\boldsymbol{n}} < 0$ (Acharya, 2003). Note that from Eq. (3.1d), only $\nabla \boldsymbol{z}^p$ (and not $\boldsymbol{z}^p$) is required here to obtain a unique $\boldsymbol{U}^p$. Thus, $\dot{\boldsymbol{z}}^p$ is arbitrarily specified at one point of the body, without loss of generality. Eq. (3.3c) implies that dislocations are not allowed to enter or leave the body through the boundaries. Equations (3.3d) and (3.3e) are the displacement and traction BCs for the static mechanical equilibrium Eq. (3.1h), and Eqs. (3.3f) and (3.3g) correspond to the imposed temperature field and heat flux on the boundary, required to solve the temperature evolution Eq. (3.1j).

The initial ($t = 0$) conditions are

$$\boldsymbol{z}^p(\bullet, 0) = 0 \quad \text{in} \quad \Omega \tag{3.4a}$$
$$\boldsymbol{\alpha}^p(\bullet, 0) = \boldsymbol{\alpha}^p_0(\bullet) \quad \text{in} \quad \Omega \tag{3.4b}$$
$$\theta(\bullet, 0) = \theta_0(\bullet) \quad \text{in} \quad \Omega, \tag{3.4c}$$

where $\boldsymbol{\alpha}^p_0$ and θ_0 are prescribed values.

3.3.3 Nondimensionalization

Similar to Zhang et al., 2015, the following dimensionless variables are introduced:

$$\begin{aligned}\tilde{\theta} = \frac{\theta}{\theta_0}\,; \quad \tilde{t} = \frac{v_s}{l_c}t\,; \quad \tilde{\boldsymbol{x}} = \frac{1}{l_c}\boldsymbol{x}\,; \quad \tilde{\boldsymbol{\sigma}}^{eq} = \frac{1}{\mu}\boldsymbol{\sigma}\,; \quad \tilde{\boldsymbol{v}} = \frac{1}{v_s}\boldsymbol{v}\,; \quad \tilde{\boldsymbol{\alpha}}^p = l_c\boldsymbol{\alpha}^p; \quad \dot{\tilde{\boldsymbol{U}}}^p = \tilde{\boldsymbol{\alpha}}^p \times \tilde{\boldsymbol{v}} \\ \tilde{\boldsymbol{u}} = \frac{1}{l_c}\boldsymbol{u}\,; \quad \tilde{\boldsymbol{K}} = \frac{1}{\rho c_\varepsilon v_s l_c}\boldsymbol{K}\,; \quad \tilde{\boldsymbol{\sigma}}^{th} = \frac{1}{\rho c_\varepsilon \theta_0}\boldsymbol{\sigma}\,; \quad \tilde{\boldsymbol{\beta}} = \frac{1}{\rho c_\varepsilon}\boldsymbol{\beta}\,; \quad \tilde{r} = \frac{l_c}{v_s c_\varepsilon \theta_0}r,\end{aligned} \tag{3.5}$$

where v_s is the shear wave propagation speed, l_c is a characteristic length of the problem (e.g., the Burgers vector magnitude), μ is computed for a given Young's modulus E and Poisson ratio ν, and $\boldsymbol{\sigma}^{eq}$ and $\boldsymbol{\sigma}^{th}$ are the dimensionless stress tensors considered when solving Equations (3.1h) and (3.1j), respectively. The governing equations in Eq. (3.1) can thus be written in a dimensionless form as

$$\tilde{\nabla}\cdot\tilde{\boldsymbol{\sigma}}^{eq} = 0 \qquad \text{in} \quad \tilde{\Omega}\times[0,\tilde{t}_F] \tag{3.6a}$$

$$\dot{\tilde{\theta}} = \tilde{\nabla}\cdot(\tilde{\boldsymbol{K}}\tilde{\nabla}\tilde{\theta}) + \tilde{\boldsymbol{\sigma}}^{th} : \dot{\tilde{\boldsymbol{U}}}^p - \tilde{\theta}\tilde{\boldsymbol{\beta}} : (\tilde{\nabla}\dot{\tilde{\boldsymbol{u}}} - \dot{\tilde{\boldsymbol{U}}}^p) + \tilde{r} \qquad \text{in} \quad \tilde{\Omega}\times(0,\tilde{t}_F] \tag{3.6b}$$

$$\dot{\tilde{\boldsymbol{\alpha}}}^p = -\tilde{\nabla}\times(\tilde{\boldsymbol{\alpha}}^p\times\tilde{\boldsymbol{v}}) \qquad \text{in} \quad \tilde{\Omega}\times(0,\tilde{t}_F], \tag{3.6c}$$

where the superposed dot indicates time derivative with respect to $\tilde{t}$, $\tilde{\Omega}$ is the nondimensional domain, and $\tilde{t}_F = \frac{v_s}{l_c}t_F$.

Henceforth, all the variables are considered in their dimensionless form. The superposed tilde is dropped for convenience unless the distinction between dimensional and dimensionless variables is explicitly made.

3.4 Finite element formulation and algorithm

In this section, the approximation of the TFDM model using the FEM is presented. The variational forms of the governing equations in Eq. (3.6) and plastic distortion in Equations (3.1b) to (3.1d) are introduced, and the algorithm is presented at the end.

3.4.1 Evolution of $\boldsymbol{\alpha}^p$

The dislocation density transport, Eq. (3.1f), is solved using a time-explicit Runge-Kutta Discontinuous Galerkin (RKDG) scheme, which was proposed in Upadhyay and Bleyer, 2021.

Consider the discretization of Ω into a mesh Ω_h, whose boundary is $\partial\Omega_h$. Henceforth, the subscript h indicates the projection of a given variable onto the mesh Ω_h i.e., $\boldsymbol{\alpha}^p_h := \Pi\boldsymbol{\alpha}^p$, where Π is the projection operator. Consider the tensor function space $\mathcal{V}^\alpha_h = \{\boldsymbol{\eta} \in [\mathcal{P}^1_D(\Omega_h)]^{3\times3}\}$, where $\mathcal{P}^1_D$ denotes the space of piecewise continuous linear polynomials defined over Ω_h and the superscript 3 corresponds to the space dimension. The variational formulation for the space discretization of Eq. (3.1f) reads (Upadhyay and Bleyer, 2021): for all test functions $\delta\boldsymbol{\alpha}_h \in \mathcal{V}^\alpha_h$, find $\boldsymbol{\alpha}^p_h \in \mathcal{V}^\alpha_h$ such

that

$$\int_{\Omega_h} \dot{\boldsymbol{\alpha}}_h^p : \boldsymbol{\delta\alpha}_h \, dV + a_h^{upw}(\boldsymbol{\alpha}_h^p, \boldsymbol{\delta\alpha}_h) \, dV = 0, \quad \forall t \in (0, t_F], \tag{3.7}$$

where $a_h^{upw}(\boldsymbol{\alpha}_h^p, \boldsymbol{\delta\alpha}_h)$ is the upwind DG bilinear form, defined as:

$$\begin{aligned} a_h^{upw}(\boldsymbol{\alpha}_h^p, \boldsymbol{\delta\alpha}_h) := & \int_{\Omega_h} (\boldsymbol{\alpha}_h^p \boldsymbol{\mu}) : \boldsymbol{\delta\alpha}_h \, dV + \int_{\Omega_h} [(\nabla_h \boldsymbol{\alpha}_h^p)\boldsymbol{v} - (\nabla_h \cdot \boldsymbol{\alpha}_h^p) \otimes \boldsymbol{v}] : \boldsymbol{\delta\alpha}_h \, dV \\ & + \int_{\partial\Omega_h} (\boldsymbol{v} \cdot \hat{\boldsymbol{n}})^{\ominus} \boldsymbol{\alpha}_h^p : \boldsymbol{\delta\alpha}_h \, dS - \sum_{F \in \mathcal{F}_h^i} \int_F (\boldsymbol{v} \cdot \hat{\boldsymbol{n}}_F) [\![\boldsymbol{\alpha}_h^p]\!] : \{\{\boldsymbol{\delta\alpha}_h\}\} \, dS \\ & + \sum_{F \in \mathcal{F}_h^i} \int_F \frac{C_\alpha}{2} |\boldsymbol{v} \cdot \hat{\boldsymbol{n}}_F| [\![\boldsymbol{\alpha}_h^p]\!] : [\![\boldsymbol{\delta\alpha}_h]\!] \, dS, \end{aligned} \tag{3.8}$$

where $\boldsymbol{\mu} := (\nabla \cdot \boldsymbol{v}) \mathbb{1} - (\nabla \boldsymbol{v})^T$ and $C_\alpha \geq 0$ is a user-specified parameter that penalizes the jumps in the trial and test functions across mesh interfaces. A parametric study conducted in Upadhyay and Bleyer, 2021 concluded that for Eq. (3.8), the optimal value for the penalty factor is $C_\alpha = 1$, which is the value adopted in this work. ∇_h denotes the broken gradient operator, which is the gradient defined within each element of the mesh, but not at the interfaces between elements. $\mathcal{F}_h^i$ denotes the collection of the interfaces in the mesh and $\hat{\boldsymbol{n}}_F$ are interface normals. $x^{\ominus} := \frac{1}{2}(|x| - x)$ denotes the negative part of a real number x. The operators $\{\{\boldsymbol{\eta}\}\}$ and $[\![\boldsymbol{\eta}]\!]$ represent the average and the jump, respectively, of a second-order tensor $\boldsymbol{\eta}$, acting individually on each component of $\boldsymbol{\eta}$. Note that the dislocation velocity vector $\boldsymbol{v}$ is assumed to be dependent on $\boldsymbol{\alpha}^p$ of the previous time step, which allows treating Eq. (3.7) as linear on $\boldsymbol{\alpha}^p$.

The time discretization of Eq. (3.7) is performed using a time-explicit strong stability preserving (SSP) RK scheme. A superscript between parenthesis (n) indicates the value of a variable at time t^n, and the superscript $(n+1)$ at time $t + \Delta t$, where Δt is a constant time-step. The s-stage RK scheme for the dislocation transport is written as (Upadhyay and Bleyer, 2021)

$$\begin{aligned} \boldsymbol{\alpha}_h^{p(n,0)} &= \boldsymbol{\alpha}_h^{p(n)} \\ \int_{\Omega_h} \boldsymbol{\alpha}_h^{p(n,i)} : \boldsymbol{\delta\alpha}_h \, dV &= \sum_{j=0}^{i-1} \left(\int_{\Omega_h} d^{ij} \boldsymbol{\alpha}_h^{p(n,j)} : \boldsymbol{\delta\alpha}_h \, dV - \Delta t \, g^{ij} a_h^{upw}(\boldsymbol{\alpha}_h^{p(n,j)}, \boldsymbol{\delta\alpha}_h) \right) \\ \boldsymbol{\alpha}_h^{p(n+1)} &= \boldsymbol{\alpha}_h^{p(n,s)}, \end{aligned} \tag{3.9}$$

where $[d^{ij}]_{1 \leq i \leq s, 0 \leq j \leq i-1}$ and $[g^{ij}]_{1 \leq i \leq s, 0 \leq j \leq i-1}$ are lower triangular matrices. In this work, 2-stage and 3-stage SSPRK schemes are used. The matrices for SSPRK2 are:

$$d = \begin{bmatrix} 1 & \\ 1/2 & 1/2 \end{bmatrix}, \quad g = \begin{bmatrix} 1 & \\ 0 & 1/2 \end{bmatrix}.$$

For SSPRK3, the following matrices are used:

$$d = \begin{bmatrix} 1 & & \\ 1/2 & 1/2 & \\ 1/3 & 1/3 & 1/3 \end{bmatrix}, \quad g = \begin{bmatrix} 1 & & \\ 0 & 1/2 & \\ 0 & 0 & 1/3 \end{bmatrix}.$$

3.4.2 Computation of χ^p

Following Roy and Acharya, 2005, χ^p is computed using the LSFEM. The tensor function space considered is $\mathcal{V}_h^\chi = \{\boldsymbol{\eta} \in [\mathcal{P}^1(\Omega_h)]^{3\times 3}\}$, where $\mathcal{P}^1$ denotes the space of linear continuous polynomials in Ω_h. The variational form of Equations (3.1b) and (3.1c) is written as: for all $\boldsymbol{\delta\chi}_h \in \mathcal{V}_h^\chi$, find $\chi_h^p \in \mathcal{V}_h^\chi$ such that

$$\begin{aligned} \int_{\Omega_h} (\nabla \times \chi_h^p) : (\nabla \times \boldsymbol{\delta\chi}_h)\, dV + \int_{\Omega_h} (\nabla \cdot \chi_h^p) \cdot (\nabla \cdot \boldsymbol{\delta\chi}_h)\, dV + \frac{C_\chi}{h} \int_{\partial\Omega_h} (\chi_h^p \hat{\boldsymbol{n}}) \cdot (\boldsymbol{\delta\chi}_h \hat{\boldsymbol{n}})\, dS \\ = -\int_{\Omega_h} \boldsymbol{\alpha}_h^p : (\nabla \times \boldsymbol{\delta\chi}_h)\, dV. \end{aligned} \tag{3.10}$$

In Eq. (3.10), the third term on the left-hand side weakly enforces the boundary condition 3.3a. C_χ is a penalty factor and h is a mesh size parameter. Numerical tests show that, while increasing C_χ increases the accuracy of the approximation of Eq. (3.3a), it also considerably increases computational cost due to the bad conditioning of the system matrix corresponding to the assembly of the bilinear form (left-hand side) of Eq. (3.10). In the current implementation, $C_\chi = 100$ is found to be an adequate compromise for the aforementioned problem.

3.4.3 Evolution of $\boldsymbol{z}^p$

A continuous Galerkin space discretization and a forward Euler time discretization are used to update $\boldsymbol{z}^p$. Consider the vector function space $\mathcal{V}_h^z = \{\boldsymbol{\eta} \in [\mathcal{P}^2(\Omega_h)]^3 \,|\, \boldsymbol{\eta}(0,\bullet) = 0\}$, where $\mathcal{P}^2$ corresponds to the space of continuous quadratic polynomials in Ω_h. Then, for each time step t^{n+1}, the variational form of Eq. (3.1d) is written as: for all $\boldsymbol{\delta z}_h \in \mathcal{V}_h^z$, find $\boldsymbol{z}_h^{p(n+1)} \in \mathcal{V}_h^z$ such that

$$\int_\Omega \nabla \boldsymbol{z}_h^{p(n+1)} : \nabla \boldsymbol{\delta z}_h\, dV = \Delta t \int_\Omega (\boldsymbol{\alpha}_h^{p(n)} \times \boldsymbol{v}^{(n)}) : \nabla \boldsymbol{\delta z}_h\, dV + \int_\Omega \nabla \boldsymbol{z}_h^{p(n)} : \nabla \boldsymbol{\delta z}_h\, dV, \tag{3.11}$$

with $\dot{\boldsymbol{z}}_h^p(0,\bullet) = 0$ being taken into account in the definition of $\mathcal{V}_h^z$ (also see argument after Eq. (3.3b)).

3.4.4 Computation of $\boldsymbol{u}$

The static equilibrium equation Eq. (3.6a) is solved to obtain $\boldsymbol{u}$ using a continuous Galerkin approach. Consider the vector function spaces $\mathcal{V}_h^u = \{\boldsymbol{\eta} \in [\mathcal{P}^2(\Omega_h)]^3 \,|\, \boldsymbol{\eta} = \bar{\boldsymbol{u}} \text{ on } \partial\Omega_u\}$ and $\mathcal{V}_{h,0}^u =$

$\{\boldsymbol{\eta} \in [\mathcal{P}^2(\Omega_h)]^3 \,|\, \boldsymbol{\eta} = 0 \text{ on } \partial\Omega_u\}$. The variational formulation of Eq. (3.6a) is written as: for all $\boldsymbol{\delta u}_h \in \mathcal{V}^u_{h,0}$, find $\boldsymbol{u}_h \in \mathcal{V}^u_h$ such that

$$\int_\Omega \Big(\mathbb{C} : \nabla \boldsymbol{u}_h\Big) : \nabla \boldsymbol{\delta u}_h \, dV = \int_{\partial\Omega^t} \bar{\boldsymbol{t}} \cdot \boldsymbol{\delta u}_h \, dS + \int_\Omega \Big\{ [\mathbb{C} : (\nabla \boldsymbol{z}^p_h + \boldsymbol{\chi}^p_h)] + \boldsymbol{\beta} \Delta\theta_h \Big\} : \nabla \boldsymbol{\delta u}_h \, dV \quad (3.12)$$

3.4.5 Evolution of θ

The temperature evolution Eq. (3.6b) is solved using a semi-implicit scheme in time, and a continuous Galerkin discretization in space. Consider the finite-dimensional function spaces $\mathcal{V}^\theta_h = \{\eta \in \mathcal{P}^2(\Omega_h) \,|\, \eta = \bar{\theta} \text{ on } \partial\Omega_\theta\}$ and $\mathcal{V}^\theta_{h,0} = \{\eta \in \mathcal{P}^2(\Omega_h) \,|\, \eta = 0 \text{ on } \partial\Omega_\theta\}$. The variational formulation of the temperature evolution reads: for all $\delta\theta \in \mathcal{V}^\theta_{h,0}$, find $\theta_h \in \mathcal{V}^\theta_h$ such that

$$\begin{aligned} \frac{1}{\Delta t} \int_\Omega \Big(\theta^{(n+1)}_h - \theta^{(n)}_h\Big) \delta\theta \, dV + \int_\Omega \Big[\boldsymbol{K} \nabla \theta^{(n+1)}_h\Big] \cdot \nabla(\delta\theta) \, dV + \int_\Omega \theta^{(n+1)} \boldsymbol{\beta} : \Big(\nabla \dot{\boldsymbol{u}}^{(n)}_h - \dot{\boldsymbol{U}}^{p(n)}_h\Big) \delta\theta \, dV \\ = - \int_{\partial\Omega^q} \bar{q} \, \delta\theta \, dS + \int_\Omega \Big(\boldsymbol{\sigma}^{th(n)}_h : \dot{\boldsymbol{U}}^{p(n)}_h\Big) \delta\theta \, dV + \int_\Omega r^{(n)} \delta\theta \, dV \end{aligned} \quad (3.13)$$

The scheme is semi-implicit in time because $\boldsymbol{\sigma}^{th(n)}_h$, $\nabla \dot{\boldsymbol{u}}^{(n)}_h$ and $\dot{\boldsymbol{U}}^{p(n)}_h$ are dependent on θ but they enter as known data in this equation.

3.4.6 Small-strains TFDM-FE algorithm

The variational Eqs. (3.9) to (3.13) are implemented using the Python front-end of the FEniCS library (Logg et al., 2012), which is an open-source PDE solver via the FEM. The implemented algorithm is shown in Alg. 1. A staggered approach is used to solve Eqs. (3.9) to (3.13).

3.5 Results and discussion

3.5.1 Temperature evolution due to dislocation motion: comparison between TFDM-FE and analytical solution

A comparison is performed between the analytical solution of the temperature field generated due to the motion of a dislocation, derived in Gurrutxaga-Lerma, 2017, and the temperature field computed through Eq. (3.13), to verify the dislocation activity-temperature evolution coupling of the TFDM model. The analytical expression was obtained by solving the two-dimensional heat equation uncoupled from elasticity and considering that the dislocation acts as a singular (point) heat source according to $q_d = b\tau v \, \delta(x - vt)\delta(y)$. In this expression, q_d is the heat generated by the moving dislocation, b is the magnitude of the Burgers vector, τ is the resolved shear stress applied on the dislocation, v is the dislocation glide speed, and the delta functions account for the

Algorithm 1: Quasi-static, small deformation TFDM-FE algorithm

Data: FE mesh, and simulation and material parameters

Result: $\boldsymbol{\alpha}^p$, $\boldsymbol{\chi}^p$, $\boldsymbol{z}^p$, $\boldsymbol{u}$, θ

begin

  assign $\boldsymbol{\alpha}_0^p$, θ_0, $\boldsymbol{z}_0^p = 0$, $\bar{\boldsymbol{t}}$, $\overline{\boldsymbol{u}}$, $\bar{q}$, $\overline{\theta}$, Δt, t_F

  $\boldsymbol{\chi}_0^p \longleftarrow$ solve Eq. (3.10)

  $\boldsymbol{u}_0 \longleftarrow$ solve Eq. (3.12)

  $\boldsymbol{\sigma}_0 \longleftarrow \mathbb{C} : (\nabla \boldsymbol{u}_0 - \boldsymbol{\chi}_0^p)$

  $\boldsymbol{v}_0 \longleftarrow f(\boldsymbol{\sigma}_0, \boldsymbol{\alpha}_0^p)$

  while $t < t_F$ **do**

    $\boldsymbol{\alpha}^{p(n+1)} \longleftarrow$ solve Eq. (3.9)

    $\boldsymbol{\chi}^{p(n+1)} \longleftarrow$ solve Eq. (3.10)

    $\boldsymbol{z}^{p(n+1)} \longleftarrow$ solve Eq. (3.11)

    $\boldsymbol{u}^{(n+1)} \longleftarrow$ solve Eq. (3.12)

    $\boldsymbol{\sigma}^{(n+1)} \longleftarrow \mathbb{C} : \left(\nabla(\boldsymbol{u}^{(n+1)} - \boldsymbol{z}^{p(n+1)}) - \boldsymbol{\chi}^{p(n+1)} \right) - \boldsymbol{\beta} \Delta\theta^{(n)}$

    $\nabla \dot{\boldsymbol{u}}^{(n+1)} \longleftarrow \frac{1}{\Delta t} \left(\nabla \boldsymbol{u}^{(n+1)} - \nabla \boldsymbol{u}^{(n)} \right)$

    $\dot{\boldsymbol{U}}^{p(n+1)} \longleftarrow \boldsymbol{\alpha}^{p(n+1)} \times \boldsymbol{v}^{(n)}$

    $\theta^{(n+1)} \longleftarrow$ solve Eq. (3.13)

    $\boldsymbol{v}^{(n+1)} \longleftarrow f\left(\boldsymbol{\sigma}^{(n+1)}, \boldsymbol{\alpha}^{p(n+1)} \right)$

    update temperature-dependent material parameters

    $t \longleftarrow t + \Delta t$

  end

motion of the dislocation on the $y = 0$ plane. The resolved shear stress τ is related to v through the mobility law (Gurrutxaga-Lerma, 2017)

$$\tau = \frac{d_0 v}{b} \frac{1}{1 - \frac{v^2}{v_s^2}}, \tag{3.14}$$

where d_0 is the low-speed drag coefficient, and v_s is the shear wave propagation velocity in the material. The main requirement for the adoption of this relation is that, for low speeds, the slope of $\tau(v)$ agrees with the observed linear viscous drag coefficient, and that it saturates as v approaches v_s. In Gurrutxaga-Lerma, 2017, a constant v, and consequently, a constant τ are assumed. The body is assumed to be initially at a homogeneous temperature θ_0. The resulting analytical expression for the temperature difference profile $\Delta\theta$ at a given time t in the bulk of a body reads

$$\Delta\theta(x, y, t) = \frac{1}{4\pi K} \frac{v^2 d_0}{1 - \frac{v^2}{v_s^2}} \int_0^t \frac{exp\left(-\frac{(x - x_c - vt')^2 + (y - y_c)^2}{4\kappa_v (t - t')}\right)}{t - t'} dt', \tag{3.15}$$

where K is the magnitude of thermal conductivity, κ_v is the thermal diffusivity at constant deformation, and (x_c, y_c) denotes the initial position of the dislocation.

Eq. (3.15) is numerically implemented using a C++ algorithm, considering a (1×1) µm^2 domain, discretized by a regular 5000×5000 grid. The integral term is computed by a composite Simpson rule, with the time interval divided into 1000 steps. The values of the coefficients considered in Eq. (3.15) are shown in Table 3.1.

The TFDM-FE simulation is conducted on a $(1 \times 1 \times 1000)$ µm^3 domain in the (x, y, z) directions, respectively. An edge dislocation whose Burgers and line vectors are parallel to $\hat{\mathbf{e}}_1$ and $\hat{\mathbf{e}}_3$, respectively, is embedded at the centre of the domain such that $\boldsymbol{\alpha}^p = \alpha^p_{13} \hat{\mathbf{e}}_1 \otimes \hat{\mathbf{e}}_3$. The initial dislocation density is assumed to be

$$\alpha^{p(0)}_{13} = \phi_0 \, exp\left(-\frac{(x - x_c)^2 + (y - y_c)^2}{2r_c^2}\right), \tag{3.16}$$

corresponding to a Gaussian profile. In this expression, ϕ_0 is a parameter that controls the magnitude of the dislocation density, x_c and y_c represent the initial position of the centre of the dislocation core, and r_c controls the dislocation core spread. To simulate a single dislocation in the model, ϕ_0 must be set such that $\int_S \phi_0 \, dS = b$, where S is an arbitrary open surface whose bounding curve encloses the dislocation line, and whose normal is, in this case, parallel to the $\hat{\boldsymbol{e}}_3$ direction. Since different discretizations of a domain lead to different integral measures, the values for ϕ_0 are usually unique to each mesh, to keep the surface integral constant. The dislocation is assumed to be moving with a constant speed $v_0 > 0$ along the x-direction, such that $\boldsymbol{v} = v_0 \hat{\mathbf{e}}_1$ (as also assumed in Gurrutxaga-Lerma, 2017).

The domain is considerably elongated in the z direction and discretized by a single element. This is done to approximate the simulation to a 2D setting using the native 3D FE implementation of the TFDM model. The (x, y) planes are discretized by a mesh that is structured and fine on the region where dislocation motion occurs, and unstructured and coarse elsewhere, as seen in Fig. H.1.

Table 3.1: Material parameters for Al and other coefficients used in Eq. (3.15) and in the FE simulations

K (W/(m K))	d_0 (Pa · s)	v_s (m/s)	x_c (µm)	y_c (µm)	κ_v (m^2/s)	γ (K^{-1})
205	2×10^{-5}	2980	0.5	0.5	9.7×10^{-5}	2.2×10^{-5}
E (GPa)	ν (-)	ρ (kg/m^3)	l_c (nm)	θ_0 (K)	c_ϵ (J/(kg K))	b (nm)
63.2	0.32	2700	1	298	782.74	0.286

For the dislocation density evolution, Eq. (3.9) is solved using the SSPRK3 scheme. Concerning the temperature evolution, since the coupling with elasticity was ignored during the derivation of the analytical solution Eq. (3.15) in Gurrutxaga-Lerma, 2017, the thermoelastic coupling term in the heat equation is neglected in the FE simulations in this comparison, and the equilibrium equation is not solved. Hence, displacement and traction boundary conditions are not needed, and a constant and homogeneous stress tensor $\boldsymbol{\sigma} = \tau(\hat{\boldsymbol{e}}_1 \otimes \hat{\boldsymbol{e}}_2 + \hat{\boldsymbol{e}}_2 \otimes \hat{\boldsymbol{e}}_1)$ is assigned, with τ given by Eq. (3.14). The boundary conditions assumed for the temperature evolution are $\theta = \theta_0$ on the planes $x = \{0, 1\}$ and $y = \{0, 1\}$, and zero heat flux on the planes $z = \{0, 1000\}$, with θ_0 given in Table 3.1. The initial setting is $\theta = \theta_0$ everywhere in Ω.

The temperature profiles predicted by the analytical solution (Eq. (3.15)) and the TFDM-FE simulation are compared for three dislocation velocities, $v_0 = \{0.01, 0.5, 0.99\}v_s$, at $t = 1.02\times 10^{-10}$ s. To facilitate the comparison, the analytical temperature profile is interpolated onto the FE mesh.

A mesh convergence analysis is performed to verify the influence of the FE discretization on the temperature profile. The element sizes used in the structured region of the mesh are $h = \{0.5, 1, 2\}$ nm. The corresponding values of ϕ_0 and r_c for the initial dislocation density Eq. (3.16) are $\phi_0 = \{1.1269\times10^{-2}, 2.8279\times10^{-3}, 7.0112\times10^{-4}\}$ and $r_c = \{2, 4, 8\}$ nm. This analysis is performed for $v = 0.99\, v_s$, since this is the case for which the highest temperature change is calculated. The usual Courant-Friedrichs-Lewy (CFL) condition imposes the following constraint on the time step of the time-explicit RKDG scheme

$$\Delta t \leq \eta \frac{h}{v}, \tag{3.17}$$

where $\eta = 0.5$ is a user-defined parameter. Considering $h = 0.5$ and $v = 0.99$, $\Delta\tilde{t}_{CFL} = 2.5\times10^{-1}$.

The time step chosen is $\Delta\tilde{t} = 10^{-2}$, which corresponds to $\Delta t = 3.36 \times 10^{-15}$ s, taking into account the relations in Eq. (3.5) and the values in Table 3.1.

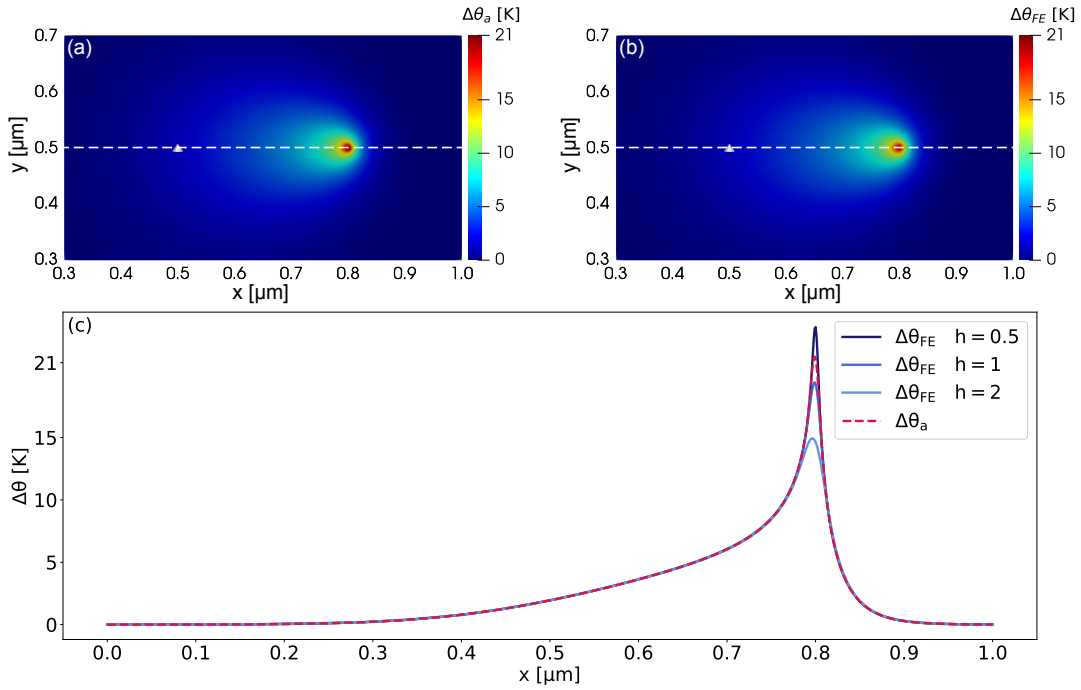

Figure 3.1: (a) Temperature field computed with the analytical solution ($\Delta\theta_a$); (b) Temperature field computed with the TFDM model ($\Delta\theta_{FE}$) for $h = 1$ nm and $r_c = 4$ nm. The white triangles in (a) and (b) indicate the dislocation core position at $t = 0$; (c) Line plots of the temperature profiles at $y = 0.5$ µm (dashed lines on (a) and (b)) computed analytically and with the FE implementation for different mesh sizes.

The resulting temperature profiles at $t = 1.02 \times 10^{-10}$ s for $v = 0.99\, v_s$ are presented in Fig. 3.1a and b. The line plot in Fig. 3.1c shows that the temperature profiles match almost exactly outside the dislocation core region. For the $h = 2$ mesh, the mean deviation outside the core is 0.71% and the maximum deviation is 3.67% of the FE solution with respect to the analytical one. As expected, the former converges to the latter when the element size is decreased, i.e. for $h = 0.5$, the mean deviation is 0.067% and the maximum deviation is 0.36%. At the location of the dislocation core, the FE simulation does not match the analytical result. This difference is due to the dislocation core being considered as singular in the analytical solution Eq. (3.15) whereas it is spread over a finite region in the FE simulation Eq. (3.16).

The same simulations are performed for $h = 1$ and $v = \{0.01, 0.50\} v_s$, and a similar behaviour is observed i.e., the temperature profiles computed by the two approaches match outside the dislocation core.

3.5.2 Illustrative examples

In this section, the temperature evolution due to the transport of edge and screw dislocations, the annihilation of two oppositely-signed edge dislocations, and the expansion of a polygonal loop are studied.

3.5.2.1 Transport of edge and screw dislocations

In what follows, the temperature profile generated due to the motion of an edge and a screw dislocation are studied while taking into account the heterogeneity of the stress state around the dislocation core; note that in Section 3.5.1, the stress heterogeneity and coupling with elasticity were neglected for the comparison. The domain, temperature profile, and thermal boundary conditions are the same as in Section 3.5.1. The initial non-zero dislocation density components for the edge and screw dislocation simulations are $\alpha_{13}^{p(0)}$ and $\alpha_{33}^{p(0)}$, respectively, where both are given by Eq. (3.16). The SSPRK3 scheme is used to solve the dislocation transport Eq. (3.9). For the mechanical problem Eq. (3.12), $\boldsymbol{u} = 0$ is assigned to the plane $y = 0$. A constant dislocation velocity $\boldsymbol{v} = 0.01\,\hat{\boldsymbol{e}}_1$ is assigned. The corresponding constant traction τ given by Eq. (3.14) (around 2 MPa) is applied on the plane $y = 1$ along the x and z directions for the edge and screw dislocation simulations, respectively. Even though the dislocation velocity does not depend on stress, applying boundary traction ensures a non-negative global dissipation. The relevant parameters considered in this simulation are shown in Table 3.1.

The mesh size on the structured region where dislocation motion takes place is $h = 2$ nm. The CFL condition Eq. (3.17) in this case imposes a maximum time step of $\Delta\tilde{t}_{CFL} = 100$, and the chosen time step is $\Delta\tilde{t} = 10$ or $\Delta t = 3.36 \times 10^{-12}$ s. The simulation is run for 5500 time steps.

The simulation results for the edge dislocation are shown in Fig. 3.2. The temperature profiles during dislocation motion arise due to the thermoelastic effect, which is captured in the model through the third term on the left-hand side of Eq. (3.13). The stress tensor of the edge dislocation contains non-zero diagonal components, which in this case are compressive above the dislocation line and tensile below it (e.g., σ_{xx} profiles in Fig. 3.2). During dislocation motion along positive x-direction, above the dislocation line, the region ahead of it is being compressed ($\Delta\sigma < 0$), while the region behind it is being decompressed ($\Delta\sigma > 0$). This entails a local temperature increase and decrease in these regions, respectively. The opposite reasoning might be applied below the dislocation line, where the region ahead of it undergoes tension ($\Delta\sigma > 0$), while the region behind it is relaxed from tension ($\Delta\sigma < 0$), which promotes a local temperature decrease and increase in these regions, respectively. In Fig. 3.2e, the asymmetry in the extent of the temperature change ahead of and behind the dislocation line is explained by the accommodation of the constant reference temperature boundary condition when it approaches the surface on the right. The temperature variation due to a single edge dislocation moving at $0.01 v_s$ is of the order of 1 mK.

The temperature evolution due to the motion of a screw dislocation is shown in Fig. 3.3. Similar to the case of edge dislocation, localized cooling and heating also occur. However, the temperature

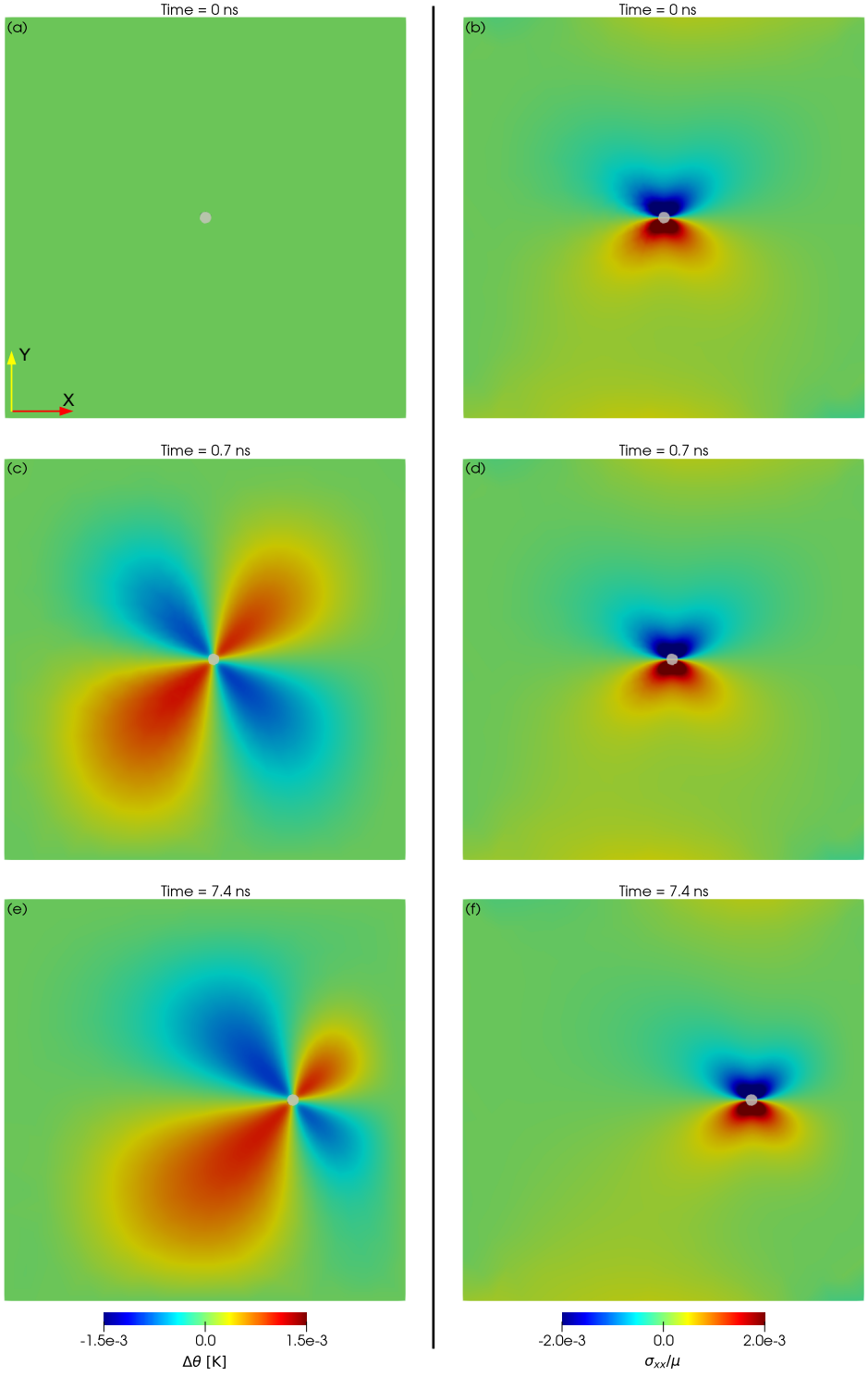

Figure 3.2: Temperature field generated around the core of an edge dislocation due to its motion in a (1×1) µm^2 domain. The white circles indicate the position of the dislocation core and are localized by the threshold $\left(\alpha^p_{ij}\alpha^p_{ij}\right)^{1/2} > 10^{-4}$. (a), (c) and (e) show the temperature profile evolution and (b), (d), and (f) the σ_{xx} component of the stress tensor evolution, with the corresponding colour bars at the bottom of each column.

profile evolution is different, and so are the magnitudes of the temperature changes around the core of the edge and the screw dislocations, with a difference of approximately one order of magnitude. To understand this difference, consider the two sources of temperature evolution in Eq. (3.1j), the thermoelastic effect, $\theta\boldsymbol{\beta} : (\nabla\dot{\boldsymbol{u}} - \dot{\boldsymbol{U}}^p) = \theta\beta_{ij}\left((\nabla\dot{u})_{ij} - \dot{U}^p_{ij}\right)$, and the plastic dissipation, $\boldsymbol{\sigma} : \dot{\boldsymbol{U}}^p = \sigma_{ij}\dot{U}^p_{ij}$ (other sources are not taken into account). For isotropic elasticity, the tensor $\boldsymbol{\beta}$ is given by $\beta_{ij} = \gamma(3\lambda + 2\mu)\,\delta_{ij}$. Thus, the thermoelastic source is expressed as

$$\theta\gamma(3\lambda + 2\mu)(\nabla\dot{u})_{ii}\,, \tag{3.18}$$

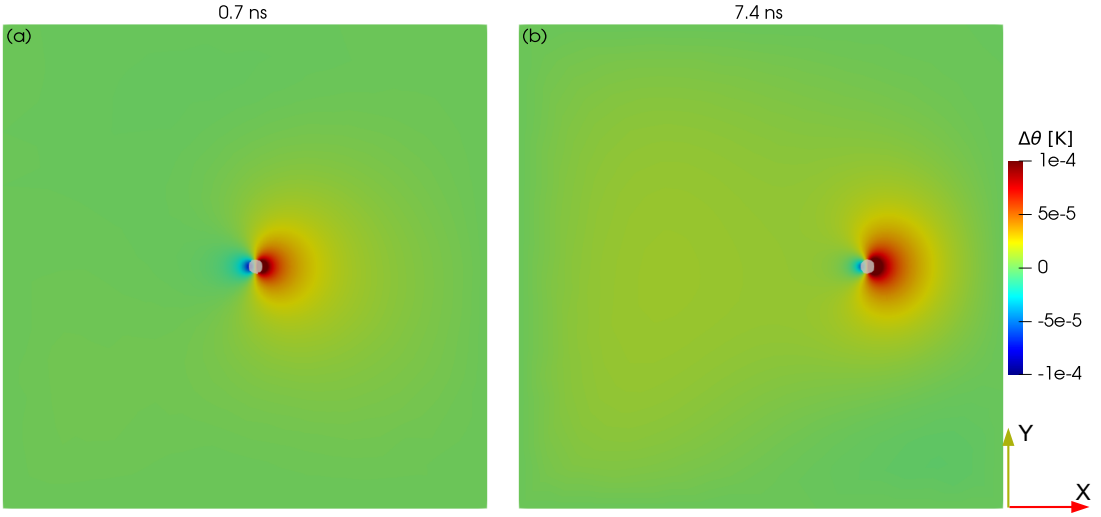

Figure 3.3: (a) - (b): Temperature field generated around the core of a screw dislocation due to its motion in a (1×1) µm^2 domain. The white circles indicate the position of the dislocation core and are localized by the threshold $\left(\alpha^p_{ij}\alpha^p_{ij}\right)^{1/2} > 10^{-4}$. The same colour bar applies to all surface plots.

since $\dot{U}^p_{ii} = 0$. For the screw dislocation α^p_{33}, the only nonzero component of the plastic distortion tensor rate is $\dot{U}^{p,S}_{32} = \alpha^p_{33}v_1$; note that the superscript 'S' corresponds to screw. The plastic dissipation in this case is $\sigma^S_{32}\alpha^p_{33}v_1$. Note that, since α^p_{33} and v_1 are strictly positive (see Eq. (3.16)), the sign of the plastic dissipation is dictated by the sign of σ^S_{32}. The closed-form solution for σ^S_{32} is (Hirth and Lothe, 1982)

$$\sigma^S_{32} = \frac{\mu b}{2\pi}\frac{x - x_c}{(x - x_c)^2 + (y - y_c)^2}\,,$$

showing that, for $x < x_c$, i.e. on the left of the dislocation line, $\sigma^S_{32} < 0$, whereas $\sigma^S_{32} > 0$ for $x > x_c$, which also applies for the plastic dissipation, as can be seen in Fig. 3.4a. With the choice of a constant dislocation velocity $\boldsymbol{v}$, a locally negative plastic dissipation is obtained at $x < x_c$, since $\text{sign}(\dot{U}^{p,S}_{32}) = \text{sign}(\sigma^S_{32}) = \text{sign}(x - x_c)$ for $\alpha^P_{33} > 0$ and $v_1 = \text{constant} > 0$. It is to be noted that, in the physical situation, for which $\boldsymbol{v}$ is a function of the stress state in the body as in Eq. (3.1g), the

plastic dissipation would be non-negative everywhere in Ω. In the present case, however, the non-negativity of the global dissipation is ensured at all times, even with a constant $\boldsymbol{v}$. The components of the total displacement of the screw dislocation α^p_{33} are $\boldsymbol{u}^S = [0, 0, u_3(x, y)] \implies (\nabla \dot{u}^S)_{ii} = 0$. Thus, the thermoelastic source in Eq. (3.18) is zero for the screw dislocation (see Fig. 3.4c). In that case, plastic dissipation is the only source of heat driving the temperature evolution, giving rise to the specific profile shown in Fig. 3.3b and c. The dislocation motion occurs in the direction of positive plastic dissipation, such that the heat accumulation in front of the dislocation line results in a more substantial temperature increase than the decrease located behind the line, ultimately resulting in an average temperature increase of the body.

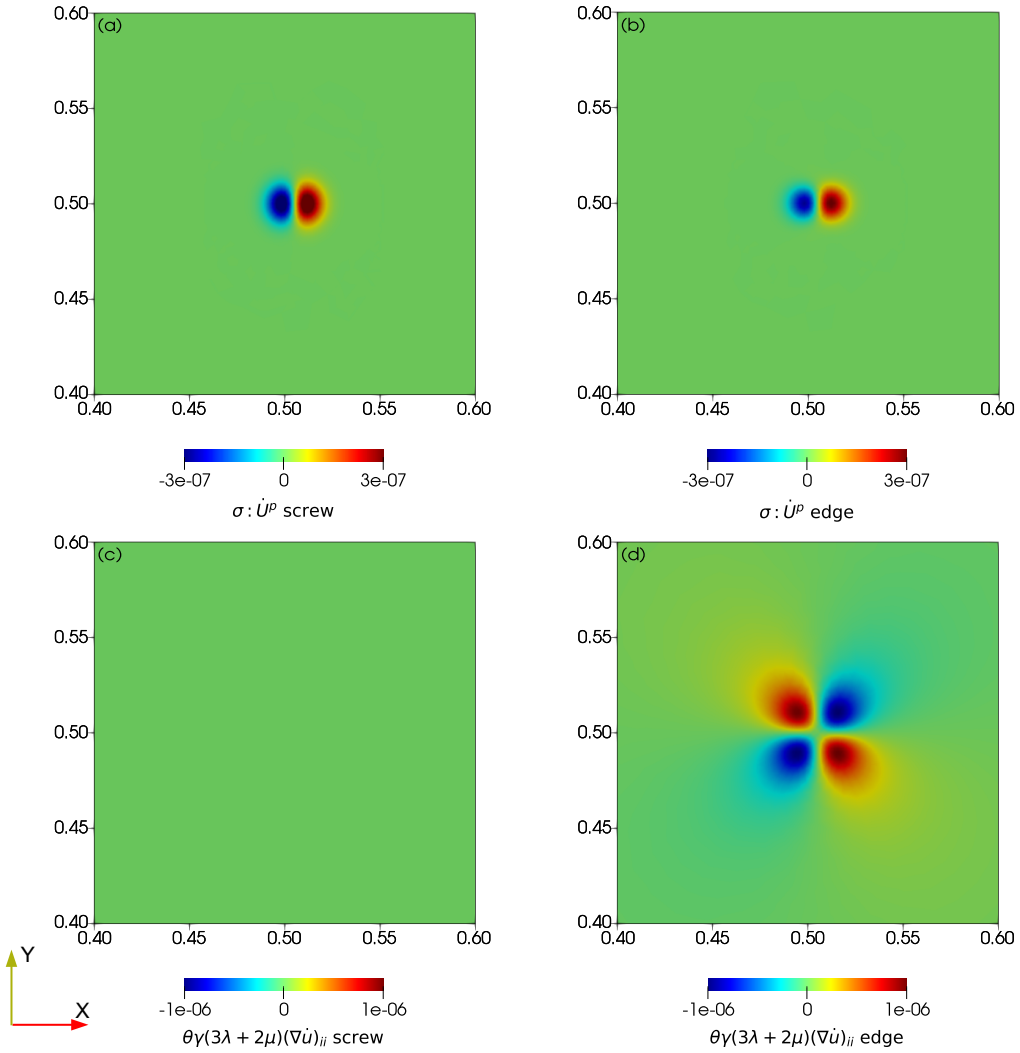

Figure 3.4: Different sources of heat for edge and screw dislocations. The dimensions are in µm, and the plots are zoomed in the centre of the (1×1) µm^2 shown in Figs. 3.2 and 3.3. Plastic dissipation due to the motion of (a) a screw dislocation and (b) an edge dislocation. Thermoelastic heat source generated by the motion of (c) a screw dislocation and (d) an edge dislocation.

For the edge dislocation α^p_{13}, the nonzero component of the plastic distortion tensor rate is $\dot{U}^{p,E}_{12} =$

$\alpha^p_{13} v_1$, which results in the plastic dissipation $\sigma^E_{12}\alpha^p_{13} v_1$; note that the superscript 'E' corresponds to edge. Similar to the screw dislocation case, the sign of the plastic dissipation is determined by the stress component σ^E_{12}, which results in the profile shown in Fig. 3.4b. The components of the total displacement of the edge dislocation α^p_{13} are $\boldsymbol{u}^E = [u_1(x,y), u_2(x,y), 0] \implies (\nabla \dot{u}^E)_{ii} \neq 0$. Thus, for the edge dislocation, the thermoelastic source of heat (Eq. (3.18)) also plays a role in the temperature evolution and is shown in Fig. 3.4d. The thermoelastic source has an antisymmetric profile about the x and y axis, which gives rise to the temperature profile in Fig. 3.2c and e, and translates the thermoelastic effect mentioned earlier in this section. The magnitude of the thermoelastic source is around three times greater than that of the plastic dissipation source for the edge dislocation. Moreover, thermoelastic heating is not restricted to the location where plasticity is taking place (dislocation core), which implies that the temperature evolution around the core of the edge dislocation is mainly due to the thermoelastic effect. This also explains the difference between the temperature profiles of the edge and screw dislocations, since, for the latter, only plastic dissipation promotes temperature evolution around the core, resulting in a smaller temperature variation due to the smaller magnitude of the dissipation source when compared to the thermoelastic one, predominant for the edge dislocation. Note that, since the thermoelastic source is antisymmetric, it produces the same magnitude of heating and cooling around the core of the edge dislocation. However, the plastic dissipation also contributes to the temperature evolution, through a mechanism similar to the one described for the screw dislocation. Thus, the motion of the edge dislocation also results in an average increase of the temperature in the domain.

This result is in contrast to the conclusion in Gurrutxaga-Lerma, 2017. There, the problem of temperature evolution due to a moving dislocation is treated analytically in two parts. In the first one, the temperature increase due to dislocation motion is computed using Eq. (3.1j), considering plastic dissipation as the only heat source, i.e. with the two last terms neglected. The analytical solution from this part is the one used for model verification in Section 3.5.1, in which a temperature increase of the order of $\sim 10^1$ K is obtained due to dislocation motion at $v = 0.99 v_s$. In the second part, the thermomechanical effects during dislocation motion are studied. To that end, the coupled thermo-elastodynamic system is solved assuming $\dot{\boldsymbol{U}}^p = 0$ and neglecting the second and fourth terms on the right-hand side of Eq. (3.1j); the elastodynamic equilibrium equation is given by $\nabla \cdot \boldsymbol{\sigma} = \rho \ddot{\boldsymbol{u}}$. In this case, the elastic strain tensor considered does not take into account the incompatibility introduced by the dislocation. Hence, the temperature increase obtained at 0.1 ns after the injection of an edge dislocation is of the order of $\sim 10^{-11}$ K, and the thermoelastic effect is said to have a negligible effect on temperature evolution in comparison to heat dissipated due to dislocation motion. However, the present work considers the incompatibility of the elastic/plastic distortions introduced by the presence of the dislocation, as expressed in Eq. (3.1b). This results in a different expression for $\nabla \dot{\boldsymbol{u}}$ in Eq. (3.1j) that explicitly considers dislocation motion. The consequence is that the contribution of the thermoelastic term to temperature evolution is more significant than plastic dissipation for the edge dislocation case illustrated here.

3.5.2.2 Annihilation of two oppositely signed edge dislocations

The problem of the annihilation of two oppositely signed dislocations was studied by R. Arora et al., 2020 in a finite deformation and isothermal setting. Here, the interest is to extend the analysis to a non-isothermal case (but under the small deformation assumption), to study the interaction of the temperature fields generated by the two moving dislocations. Consider two edge dislocations of opposite signs, whose initial dislocation density is given by

$$\alpha_{13}^{p(0)} = \begin{cases} \phi_0 & |x - x_1^c| \leq r_c \text{ and } |y - y_1^c| \leq r_c \\ -\phi_0 & |x - x_2^c| \leq r_c \text{ and } |y - y_2^c| \leq r_c \\ 0 & \text{otherwise,} \end{cases} \tag{3.19}$$

where (x_1^c, y_1^c) and (x_2^c, y_2^c) are the positions of the centre of each edge dislocation core, and ϕ_0 and r_c are defined as for Eq. (3.16). A structured and refined mesh is used in the region where dislocation motion occurs, with an element size of $h = 1$ nm. The values of the constants in Eq. (3.19) are $(x_1^c, y_1^c) = (0.31, 0.50)$ µm, $(x_2^c, y_2^c) = (0.69, 0.50)$ µm, $r_c = 6$ nm and $\phi_0 = 1.7\times10^{-3}$.

The dislocation velocity field considered is

$$\boldsymbol{v} = \Big(0.01\text{sign}(\alpha_{13}^p)\Big)\hat{\boldsymbol{e}}_1, \tag{3.20}$$

such that the dislocation lines will move towards each other with a constant speed of $0.01v_s$. The SSPRK3 scheme is used to compute the dislocation density evolution. The boundary conditions and initial temperature profile are the same as those used in Section 3.5.2.1, and the parameters in Table 3.1 are also adopted here. The CFL condition Eq. (3.17) imposes a maximum time step of $\Delta\tilde{t}_{CFL} = 50$, such that the time step considered is $\Delta\tilde{t} = 5$, or $\Delta t = 1.68\times10^{-11}$ s, and the simulation is run for 5800 time steps.

The simulation results are shown in Fig. 3.5 with the initial condition shown in Fig. 3.5a. In Fig. 3.5b, a temperature profile similar to the one in Fig. 3.2e is observed, which is mainly driven by the thermoelastic source of heat Eq. (3.18). As shown in Fig. H.2a and b, the thermoelastic heat sources are the same for both dislocation lines, which leads to similar temperature profiles. Upon approximation, regions of opposite $\Delta\theta$ sign tend to neutralize each other, as in Fig. 3.5b. The curves depicted in Fig. 3.5d show that the contribution of the plastic dissipation to the temperature evolution increases as the dislocation lines approach each other, due to the increased stress values around the cores. This leads to a localized temperature increase in that region, since the positive parts of the plastic dissipation profile superpose between the dislocation lines (see Fig. S2c and d), hence the more substantial temperature increase shown in Fig. 3.5c when compared to the single dislocation case (Fig. 3.2c). Finally, after annihilation occurs, no more heat sources are left in the body, so it returns to the reference temperature.

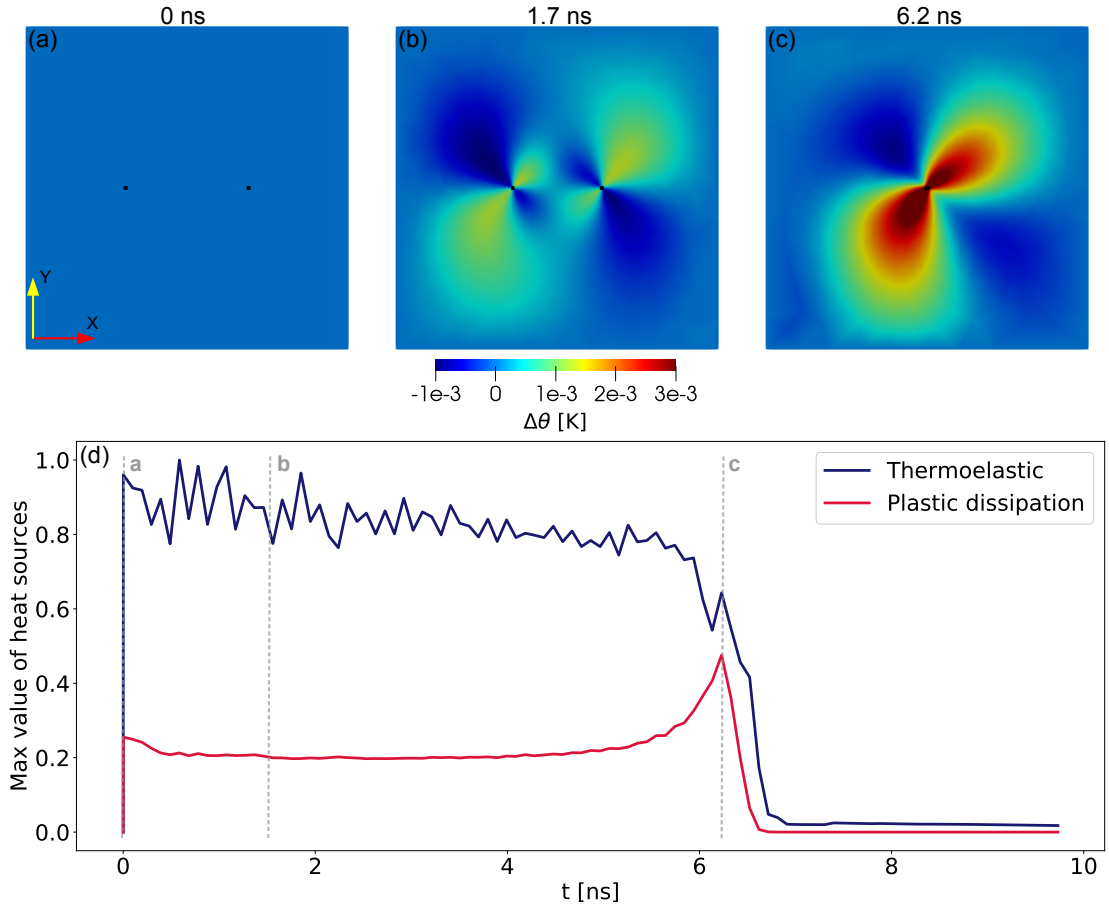

Figure 3.5: (a) - (c): Temperature field evolution during the annihilation of two oppositely signed edge dislocations in a (1×1) µm^2 domain. The black squares indicate the positions of the dislocation cores, localized by the threshold $\left(\alpha^p_{ij}\alpha^p_{ij}\right)^{1/2} > 10^{-3}$, and the colour bar applies to all surface plots. (d) Evolution of the maximum absolute value of the plastic dissipation and thermoelastic heat sources, normalized by the maximum value of the latter. The grey dashed lines indicate the times corresponding to the snapshots in (a) - (c).

3.5.2.3 Expansion of a polygonal dislocation loop

Consider a polygonal dislocation loop whose Burgers vector lies in the xy-plane, with density given by $\boldsymbol{\alpha}^p = \alpha^p_{11}\,\hat{\boldsymbol{e}}_1\otimes\hat{\boldsymbol{e}}_1 + \alpha^p_{12}\,\hat{\boldsymbol{e}}_1\otimes\hat{\boldsymbol{e}}_2$. The domain size is $(100\times100\times100)$ nm^3. The mesh is fine and structured (element size $h = 1.29$ nm) in a rectangular cuboid region of $(100\times100\times9)$ nm^3 centred at $(50,50,50)$ nm, and coarser and unstructured elsewhere, as shown in Fig. H.3.

The initial dislocation loop configuration is shown in Fig. 3.6a. The loop is centered at $(50,50,50)$ nm, and its side length is $L = l_c + 2w_c$, where $l_c = 10h$ is the length of the straight segments, and $w_c = 4h$ is the core width. The straight screw and edge segments have an initial density $\alpha^{p(0)}_{11} = \phi_0$ and $\alpha^{p(0)}_{12} = \phi_0$ on the bottom and on the right, and $\alpha^{p(0)}_{11} = -\phi_0$ and $\alpha^{p(0)}_{12} = -\phi_0$ on the

top and the left of the loop, respectively. On the corners of the loop, the initial densities are

$$\begin{aligned}\alpha_{11}^{p(0)} &= -\phi_0 \frac{y-(y_c+b)}{\sqrt{\Big(x-(x_c+a)\Big)^2+\Big(y-(y_c+b)\Big)^2}} \\ \alpha_{12}^{p(0)} &= \phi_0 \frac{x-(x_c+a)}{\sqrt{\Big(x-(x_c+a)\Big)^2+\Big(y-(y_c+b)\Big)^2}},\end{aligned} \tag{3.21}$$

where $(x_c, y_c) = (50, 50)$ nm are the coordinates of the centre of the loop, (a, b) are equal to (l_c, l_c), $(-l_c, l_c)$, $(-l_c, -l_c)$, $(l_c, -l_c)$ on the top right, top left, bottom left and bottom right corners of the loop, respectively, and $\phi_0 = 1.03 \times 10^{-1}$. The dislocation velocity is assigned to be normal to the line segments, with components on the xy-plane given by

$$\begin{aligned}v_1 &= v_0 \frac{\alpha_{12}^p}{\|\boldsymbol{\alpha}^p\|} \\ v_2 &= -v_0 \frac{\alpha_{11}^p}{\|\boldsymbol{\alpha}^p\|} \\ \|\boldsymbol{\alpha}^p\| &= \sqrt{\Big(\alpha_{11}^p\Big)^2+\Big(\alpha_{12}^p\Big)^2},\end{aligned} \tag{3.22}$$

where $v_0 = 0.01 v_s$ is constant. With these choices, the plastic distortion rate is

$$\dot{\boldsymbol{U}}^p = \dot{U}_{13}^p \hat{\boldsymbol{e}}_1 \otimes \hat{\boldsymbol{e}}_3, \quad \dot{U}_{13}^p = (\boldsymbol{\alpha}^p \times \boldsymbol{v})_{13} = \alpha_{11}^p v_2 - \alpha_{12}^p v_1 = -\frac{v_0}{\|\boldsymbol{\alpha}^p\|}\left((\alpha_{11}^p)^2 + (\alpha_{12}^p)^2\right), \tag{3.23}$$

such that the dissipative heat source in Eq. (3.1j) becomes $\sigma_{13}\dot{U}_{13}^p$. Since, from Eq. (3.23), $\dot{U}_{13}^p \leq 0$, the sign of the dissipative heat source will depend on the sign of σ_{13}.

The SSPRK2 scheme is used to compute the dislocation density evolution. The mechanical boundary conditions are $\boldsymbol{u} = 0$ on the $z = 0$ plane, and a traction $t = -1$ GPa along the x-direction is applied on the $z = 100$ plane. For this simulation, using Eq. (3.14) for the boundary traction value results in a negative global dissipation (Eq. (3.2)). This is due to the fact that the dislocation velocity is uncoupled from the stress state. However, setting $t = -1$ GPa ensures that the global dissipation is non-negative. A constant temperature $\theta = \theta_0$ is imposed on all boundaries. The parameters shown in Table 3.1 are also used here. The CFL condition (Eq. (3.17)) allows for a maximum time step of $\Delta\tilde{t}_{CFL} = 64.5$ and the time step used is $\Delta\tilde{t} = 1$ or $\Delta t = 3.36 \times 10^{-13}$ s.

Due to the arbitrariness of the applied traction value, no quantitative information can be extracted from the temperature values, and only the temperature normalized with respect to its maximum value is studied (see Fig. 3.6). Thus, the results qualitatively illustrate the zones where heating and cooling occur during loop expansion. During expansion, the sign of σ_{13} changes across the dislocation loop segments, with $\sigma_{13} > 0$ inside the loop, and $\sigma_{13} < 0$ outside of it. At the start of the expansion, $|\sigma_{13}|$ is greater in the interior than in the exterior part of the loop due to the

proximity of the loop segments. This results in local cooling just inside the loop and local heating just outside the loop (Fig. 3.6b). As the loop continues to expand, $|\sigma_{13}|$ in the exterior of the loop increases due to the increasing proximity between the loop and the domain boundaries, which gives rise to increasing image stresses. This results in a continuous increase of the positive part of the dissipative heat source $\sigma_{13}\dot{U}^p_{13} > 0$ (Fig. 3.6e), which promotes temperature increase both inside and outside the loop (Fig. 3.6c and d); the negative part of the dissipation heat source has an order of magnitude lower contribution to the temperature than the positive dissipation part, which explains why temperature increases.

Contrary to what was observed in the single edge dislocation case (Section 3.5.2.1), the contribution of thermoelasticity to the temperature evolution is less significant than the one from plastic dissipation (Fig. 3.6e). This can be understood as follows. The dislocation loop is composed of two screw segments and two edge segments, the latter being the only ones for which the thermoelastic heat source is non-zero. Moreover, this heat source depends on $\nabla\dot{\boldsymbol{u}}$ (Eq. (3.18)). Hence, if the applied traction is kept constant, then its value will not affect $\nabla\dot{\boldsymbol{u}}$ and the thermoelastic heat source, which only changes due to dislocation motion. However, the applied traction directly impacts the dissipative heat source through $\boldsymbol{\sigma}$. Since the applied traction has a high magnitude of 1 GPa, its contribution to plastic dissipation results in this heat source term having a significantly higher contribution than the thermoelastic heat source. Consequently, plastic dissipation has a greater impact on the temperature evolution for this loop expansion simulation.

3.6 Conclusion and perspectives

This paper presents the FE approximation of the TFDM (thermal field dislocation mechanics) model (Upadhyay, 2020). The variational formulations of the TFDM governing equations are presented and a staggered numerical algorithm for their resolution is proposed. In addition to all the possibilities of the isothermal FDM model, the TFDM model allows for explicitly modelling the influence of dislocation activity on the temperature profile evolution of a body as well as the influence of temperature and heat flux boundary conditions on dislocation evolution.

The TFDM-FE model is verified by comparison with an analytical solution of the temperature profile generated due to the motion of a single edge dislocation in a constant homogeneous stress field neglecting the dislocation self-stress. A remarkable agreement is obtained between the analytical and numerical solutions outside the dislocation core. The solutions differ within the dislocation core due to the difference in the manner in which the dislocations are treated in the analytical solution (singular defect) and the TFDM-FE model (a finite non-zero polar density). A mesh convergence analysis demonstrated the improvement of the match between the two approaches.

Following this verification, the model is applied to study the transport of edge and screw dislocations, dislocation annihilation and expansion of a polygonal loop. In all these simulations, the heterogeneity of the stress state around the core of the dislocations is considered. The analysis of

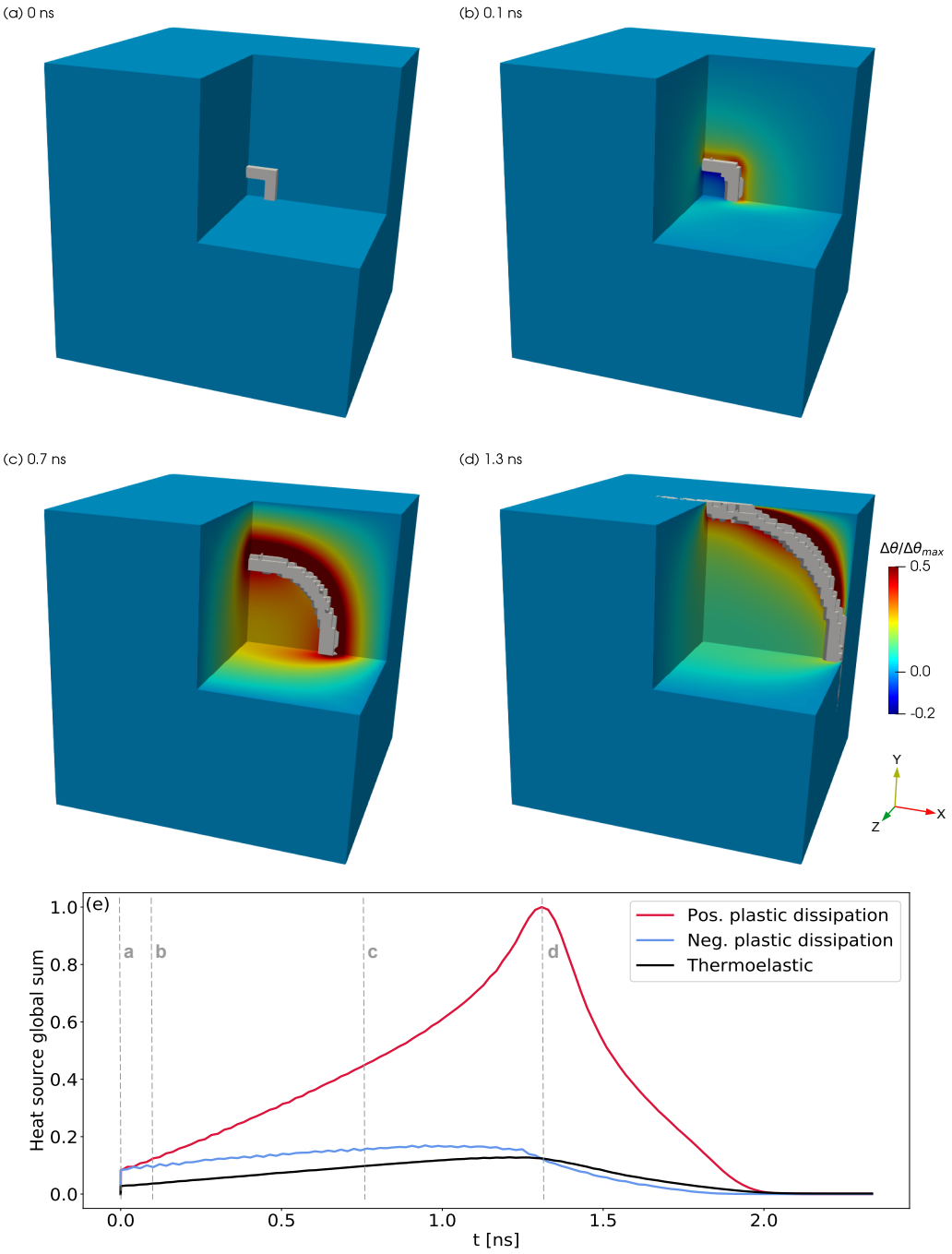

Figure 3.6: (a) - (d) Temperature field evolution on the planes $x = 50$ nm, $y = 50$ nm, and $z = 50$ nm during the expansion of a polygonal dislocation loop in a $(100 \times 100 \times 100)$ nm^3 domain. The loop is shown in grey and is localized by the threshold $\left(\alpha^p_{ij}\alpha^p_{ij}\right)^{1/2} > 10^{-2}$. The temperature is normalized with respect to its maximum value, and the same colour bar applies to all surface plots. (e) Sum over the domain of the absolute values of the thermoelastic and plastic dissipation heat sources' evolution during the loop expansion simulation. The positive and negative components of the dissipative term are plotted separately, and all curves are normalized by the maximum value of the positive plastic dissipation. The grey dashed lines indicate the times corresponding to the snapshots in (a) - (d)

the temperature profile evolution during the motion of an edge and a screw dislocation showed that the thermoelastic coupling and the plastic dissipation contribute differently according to the dislocation type. For an edge dislocation studied here, the thermoelastic effect is found to have the highest contribution to temperature evolution, whereas plastic dissipation is the only active heat source during transport of a screw dislocation. The dislocation annihilation reveals an increasing influence of plastic dissipation on the temperature evolution due to the increase in the stresses near the dislocation cores as the dislocations approach each other. An increasing influence of plastic dissipation also occurs in the dislocation loop expansion case due to the increasing effect of image stresses from domain boundaries.

4 Conclusion

4.1 Summary of the research findings

The primary objectives of this research were the following: to develop a continuum finite deformation theory that allows for solving initial boundary value problems of dislocation thermomechanics, taking into account the contribution of dislocation activity to temperature evolution, as well as the impact of thermomechanical boundary conditions on the evolution of dislocations; and to numerically implement the geometrically linearised version of the theory, which coincides with the work presented in Upadhyay, 2020, using the finite element method. The main results obtained corresponding to each of these objectives are summarised in the following sections.

4.1.1 Thermomechanical theory of field dislocations

The proposed theory, fully based on conservation laws, incorporates a novel kinematics for the thermo-elastoplasticity based on dislocation mechanics while accounting for geometrical nonlinearities. The evolution of the dislocation density is coupled with the transient temperature field through a source term that accounts for incompatibilities in thermal strains and results in the introduction of a more gerenal thermomechanical defect density $\boldsymbol{\alpha}$, which contains contributions from both dislocation lines and incompatibilities in thermal strains (Eq. (2.20)). The theory requires the definition of neither a global reference configuration nor a multiplicative decomposition of the deformation gradient tensor $\boldsymbol{F}$ resulting from it. The kinematics of the model is fully based on the conservation of Burgers vector, which yields the widely accepted additive decomposition of the spatial velocity gradient tensor into elastic, plastic and thermal parts (Eq. (2.26)). Only observable fields serve as the basis for the theory, namely elastic distortion tensor, temperature, and thermomechanical defect density, with plasticity directly arising as a consequence of the evolution of the latter.

Considering $\boldsymbol{\alpha}$ (with its evolution coupled with the temperature evolution) as a state variable in the definition of the Helmholtz free energy of the system results in a new structure of the temperature evolution equation (Eq. (2.62)) that allows for solutions in the form of dispersive

waves with finite propagation speed, despite adopting Fourier's law as the constitutive statement for the heat flux vector. A linear analysis of a simplified version of the equation that keeps its core structure (in terms of the partial derivatives involved) revealed that it allows for spatial patterning in the temperature field to arise, stemming from well-posed linear instabilities. The theory also allows the definition of a Taylor-Quinney factor that is dependent on the strain rate and material, the plastic contribution stemming directly from the evolution of the thermomechanical defect density (Eq. (2.65)). Upon geometric linearisation, the theory reduces to the small deformation framework proposed in Upadhyay, 2020, up to a difference of the $\boldsymbol{\alpha}$ evolution statement.

This research contributes to the scope of continuum models of dislocation mechanics by adding the capability of accounting for the interplay between temperature evolution and dislocation activity on the solid state, while also handling finite deformations, elastic and thermal anisotropy, and intertial effects. It is expected that the proposed theory will aid in understanding the evolution of dislocation structures in bodies during any kind of thermomechanical processes, including but not limited to metal additive manufacturing, forging, welding, quenching, etc.

4.1.2 Numerical implementation of the TFDM theory

The geometric linearisation of the proposed finite deformation theory of dislocation thermomechanics was shown to reduce to the small deformation TFDM theory proposed in Upadhyay, 2020. The latter was numerically implemented using the FEniCS open source library designed for solving partial differential equations through the finite element method. The implementation consists of five variational equations (Eqs. (3.7) and (3.10) to (3.13)) that are solved in a staggered algorithm. The required inputs are the finite element mesh, simulation and material parameters (which may be temperature dependent), as well as initial and boundary conditions, with possible outputs being the time evolution of the dislocation density, the plastic distortion tensor (split into compatible and incompatible parts), the total displacement, and the temperature field.

The numerical approach is verified against an analytical calculation of the temperature field generated due to the motion of a single dislocation considering a homogeneous stress state. Remarkable agreement is obtained outside the dislocation core region, which is shown to improve with refinement of the finite element mesh. Following this verification, examples are shown that illustrate some of the capabilities of the implemented theory. That is, the temperature evolution is studied in the case of transport of a single edge and screw dislocations, annihilation of two edge dislocations, and expansion of a polygonal dislocation loop, all considering the heretogeneity of the stress state in the vicinity of the dislocation cores. The model allows for highlighting the different heat sources active depending on the dislocation type, as well as accounting for the impact of stress interaction between dislocations and image effects close to free surfaces on the temperature evolution.

The Python codes will be made available to the community and are structured in a way that allows for rather straightforward additions to it as well as coupling with other approaches to enrich the

possible predictions. For instance, the stress-strain constitutive relation can be easily changed; crystal anisotropy can be straightforwardly incorporated through the expression of the stiffness tensor; different dislocation mobility laws can be provided, etc.

4.2 Recommendations for future research

For future studies, the proposed finite deformation theory of dislocation thermomechanics would greatly benefit from a numerical implementation of its PDEs using, e.g., the finite element method. The work by R. Arora et al., 2020 on the finite element approximation of finite deformation mesoscale FDM could serve as a foundational basis. Furthermore, the Runge-Kutta discontinuous Galerkin approach, successfully applied to the dislocation density transport equation by Upadhyay and Bleyer, 2021 and in the present work, could be considered for implementing the thermomechanical defect evolution in equation Eq. (2.20).

To incorporate crystallography into the proposed theory, one could consider the phase field crystal (PFC) approach (Elder et al., 2002), which provides a continuum framework for the mesoscale description of crystalline phases of different symmetries. PFC relies on a non-convex energy functional of a scalar phase field and its gradients, with lattice symmetry dependent on the form of this functional. Acharya and Viñals, 2020 proposed a coupling between PFC and FDM, and Upadhyay and Viñals, 2024 made the first contribution towards a numerical implementation of the coupled theory. The phase field in PFC includes a compact and localised description of dislocation cores that can be transferred to the dislocation density tensor in FDM while keeping its topological properties. Extending the coupling proposed by Acharya and Viñals, 2020 to the theory presented here would involve accounting for the contribution of incompatible thermal strains to the kinematics of thermomechanical line defects (Eqs. (2.20) and (2.25)) and for the temperature dependence of the free energy density of the system.

Future efforts should also focus on upscaling the theory developed in this thesis to consider the impact of statistically stored dislocations (SSDs) on plastic deformation, which is crucial for studying dislocation thermomechanics at the μm scale and above. The coarse-grained theory would allow for a more in-depth understanding of the evolution of dislocation structures during thermomechanical processes involving strong transient temperature gradients, such as observed during metal AM in Gaudez et al., 2023. In dislocation mechanics, different routes have been proposed to bridge the gap between microscopic theory and its coarse-grained counterpart. Acharya and Roy, 2006 considers upscaling the microscopic FDM theory by applying a space-time averaging function to all fields, with closure obtained through phenomenological expressions for the dislocation velocity vector, dislocation nucleation tensor, and plastic strain rate due to SSDs. Another approach by Valdenaire et al., 2016 is based on a simplified 2D model with straight edge dislocation lines, where the coarse-graining procedure requires spatial and temporal convolution with ensemble averaging, resulting in scale-dependent local friction and back stresses influenced by dislocation correlations.

A Notation

Scalars are denoted with an italic font (e.g., r or θ). Vectors are denoted by a lowercase bold and italic Latin font (e.g., $\boldsymbol{q}$). Considering fixed Cartesian reference frames, the orthonormal basis vectors in Ω_r are denoted $\{\hat{\boldsymbol{e}}^r_I\}$, $I = 1,2,3$, while the orthonormal basis vectors in Ω_t are denoted $\{\hat{\boldsymbol{e}}_i\}$, $i = 1,2,3$. Lowercase (uppercase) indices refer to quantities in Ω_t (Ω_r). Points in Ω_t (Ω_r) are denoted $\boldsymbol{x}$ ($\boldsymbol{x}_r$). The second-order identity tensor is denoted $\mathbb{1}$, whose components are δ_{ij} (the Kronecker delta). The third-order Levi-Civita permutation tensor is denoted $\mathbf{X}$, with components e_{ijk} (the permutation symbol). Fourth-order tensors are denoted by double-stroke letters (e.g., $\mathbb{C}$). The null tensor is denoted 0 for any tensor order. Summation of repeated indices is implied unless otherwise stated. Consider the vectors $\boldsymbol{u}, \boldsymbol{v} \in \Omega_t$, as well as the tensors $\boldsymbol{\alpha}, \boldsymbol{B} \in \Omega_t$. Then, we define the following operations:

Tensor product:
$\boldsymbol{u} \otimes \boldsymbol{v} = u_i v_j \, \hat{\boldsymbol{e}}_i \otimes \hat{\boldsymbol{e}}_j$

Inner product:
$\boldsymbol{u} \cdot \boldsymbol{v} = u_i v_i$
$\boldsymbol{\alpha} : \boldsymbol{B} = \alpha_{ij} B_{ij}$

Cross product:
$\boldsymbol{u} \times \boldsymbol{v} = e_{ijk} u_j v_k \, \hat{\boldsymbol{e}}_i$
$\boldsymbol{\alpha} \times \boldsymbol{u} = e_{jkl} \alpha_{ik} u_l \, \hat{\boldsymbol{e}}_i \otimes \hat{\boldsymbol{e}}_j$

Tensor multiplication and action on vectors:
$\boldsymbol{\alpha}\boldsymbol{B} = \alpha_{ij} B_{jk} \, \hat{\boldsymbol{e}}_i \otimes \hat{\boldsymbol{e}}_k$
$\boldsymbol{\alpha}\boldsymbol{u} = \alpha_{ij} u_j \, \hat{\boldsymbol{e}}_i$
$\boldsymbol{v}\boldsymbol{B} = v_i B_{ij} \, \hat{\boldsymbol{e}}_j$

Double-dot product:
$\mathbf{X} : \boldsymbol{\alpha} = e_{ijk} \alpha_{jk} \, \hat{\boldsymbol{e}}_i$
$\mathbb{C} : \boldsymbol{\alpha} = \mathbb{C}_{ijkl} \alpha_{kl} \, \hat{\boldsymbol{e}}_i \otimes \hat{\boldsymbol{e}}_j$

Differential operators on Ω_t (comma indicates differentiation with respect to a given coordinate):
$\nabla \boldsymbol{u} = \operatorname{grad} \boldsymbol{u} = u_{i,j} \, \hat{\boldsymbol{e}}_i \otimes \hat{\boldsymbol{e}}_j$
$\nabla \boldsymbol{\alpha} = \operatorname{grad} \boldsymbol{\alpha} = \alpha_{ij,k} \, \hat{\boldsymbol{e}}_i \otimes \hat{\boldsymbol{e}}_j \otimes \hat{\boldsymbol{e}}_k$
$\nabla \cdot \boldsymbol{u} = \operatorname{div} \boldsymbol{u} = u_{i,i}$
$\nabla \cdot \boldsymbol{\alpha} = \operatorname{div} \boldsymbol{\alpha} = \alpha_{ij,j} \, \hat{\boldsymbol{e}}_i$
$\nabla \times \boldsymbol{u} = \operatorname{curl} \boldsymbol{u} = e_{ijk} u_{k,j} \, \hat{\boldsymbol{e}}_i$
$\nabla \times \boldsymbol{\alpha} = \operatorname{curl} \boldsymbol{\alpha} = e_{jkl} \alpha_{il,k} \, \hat{\boldsymbol{e}}_i \otimes \hat{\boldsymbol{e}}_j$,

A *two-point tensor* is defined as $\boldsymbol{W} = W_{Ij} \hat{\boldsymbol{e}}^r_I \otimes \hat{\boldsymbol{e}}_j$ or $\boldsymbol{F} = F_{iJ} \hat{\boldsymbol{e}}_i \otimes \hat{\boldsymbol{e}}^r_J$.

The *material time derivative* in Ω_t is denoted by a superposed dot $\dot{\square}$. $\det(\square)$ and $\operatorname{tr}(\square)$ indicate

the *determinant* and the *trace* of a tensor, respectively. The *symmetric* and *skew-symmetric* parts of a tensor are denoted by sym(□) and skew(□), respectively. The Frobenius norm of a second-order tensor is denoted by $\|\boldsymbol{B}\| := (\boldsymbol{B} : \boldsymbol{B})^{1/2}$.

B Invariance requirements of Y

Consider a point in Ω_t expressed as $\boldsymbol{x}(\boldsymbol{x}_r, t)$, with $\boldsymbol{x}_r \in \Omega_r$. A rigid body motion of Ω_t can be expressed as

$$\boldsymbol{x}^*(\boldsymbol{x}, t) = \boldsymbol{Q}(t)\boldsymbol{x}(\boldsymbol{x}_r, t) + \boldsymbol{c}(t) \tag{B.1}$$

for any proper rotation tensor $\boldsymbol{Q}$ and translation vector c. A one-to-one mapping $\boldsymbol{\chi}(\boldsymbol{x}_r, t)$ can be defined between Ω_r and Ω_t, with the corresponding inverse $\boldsymbol{\chi}^{-1}(\boldsymbol{x}, t)$ (Willis, 1967). Considering a rotated configuration Ω_t^*, this allows us to write:

$$\boldsymbol{F}^{e*} = \boldsymbol{Q}\boldsymbol{F}^e \tag{B.2a}$$
$$\boldsymbol{W}^* = \boldsymbol{W}\boldsymbol{Q}^T. \tag{B.2b}$$

For the transformation of $\boldsymbol{\alpha}$, we have the requirement that

$$\boldsymbol{\alpha}\hat{\boldsymbol{n}} = \boldsymbol{\alpha}^*\hat{\boldsymbol{n}}^* \quad \forall \hat{\boldsymbol{n}}, \hat{\boldsymbol{n}}^*, \tag{B.3}$$

with $\hat{\boldsymbol{n}}^* = \boldsymbol{Q}\hat{\boldsymbol{n}}$, which leads to

$$\boldsymbol{\alpha}\hat{\boldsymbol{n}} = \boldsymbol{\alpha}^*\boldsymbol{Q}\hat{\boldsymbol{n}} \implies (\boldsymbol{\alpha} - \boldsymbol{\alpha}^*\boldsymbol{Q})\hat{\boldsymbol{n}} = 0 \quad \forall \hat{\boldsymbol{n}} \iff \boldsymbol{\alpha}^* = \boldsymbol{\alpha}\boldsymbol{Q}^T. \tag{B.4}$$

Consistency with the evolution statement in Eq. (2.25) requires that

$$\begin{aligned}
&\dot{\boldsymbol{W}}^* + \boldsymbol{W}^*\boldsymbol{L}^* = \boldsymbol{\alpha}^* \times \boldsymbol{v}^{d*} + \boldsymbol{Y}^*\dot{\theta} \\
\implies &\dot{\overline{\boldsymbol{W}\boldsymbol{Q}^T}} + \boldsymbol{W}\boldsymbol{Q}^T\left(\dot{\boldsymbol{Q}}\boldsymbol{Q}^T + \boldsymbol{Q}\boldsymbol{L}\boldsymbol{Q}^T\right) = (\boldsymbol{\alpha}\boldsymbol{Q}^T) \times \boldsymbol{v}^{d*} + \boldsymbol{Y}^*\dot{\theta} \\
\implies &\dot{\boldsymbol{W}}\boldsymbol{Q}^T + \boldsymbol{W}\dot{\boldsymbol{Q}}^T + \boldsymbol{W}\boldsymbol{Q}^T\dot{\boldsymbol{Q}}\boldsymbol{Q}^T + \boldsymbol{W}\boldsymbol{L}\boldsymbol{Q}^T = (\boldsymbol{\alpha}\boldsymbol{Q}^T) \times \boldsymbol{v}^{d*} + \boldsymbol{Y}^*\dot{\theta} \\
\implies &\dot{\boldsymbol{W}} + \boldsymbol{W}\boldsymbol{L} + \boldsymbol{W}\dot{\boldsymbol{Q}}^T\boldsymbol{Q} + \boldsymbol{W}\boldsymbol{Q}^T\dot{\boldsymbol{Q}} = [(\boldsymbol{\alpha}\boldsymbol{Q}^T) \times \boldsymbol{v}^{d*}]\boldsymbol{Q} + \boldsymbol{Y}^*\boldsymbol{Q}\dot{\theta} \\
\implies &\dot{\boldsymbol{W}} + \boldsymbol{W}\boldsymbol{L} = [(\boldsymbol{\alpha}\boldsymbol{Q}^T) \times \boldsymbol{v}^{d*}]\boldsymbol{Q} + \boldsymbol{Y}^*\boldsymbol{Q}\dot{\theta}.
\end{aligned} \tag{B.5}$$

Assuming $\boldsymbol{v}^{d*} = \boldsymbol{Q}\boldsymbol{v}^{d}$ and $\boldsymbol{Y}^{*} = \boldsymbol{Y}\boldsymbol{Q}^{T}$, it can be shown that Eq. (B.5) leads to

$$\dot{\boldsymbol{W}} + \boldsymbol{W}\boldsymbol{L} = \boldsymbol{\alpha} \times \boldsymbol{v}^{d} + \boldsymbol{Y}\dot{\theta} \tag{B.6}$$

Hence, to comply with invariance requirements, under a rigid body motion $\boldsymbol{v}^{d}$ must transform as an objective vector, and $\boldsymbol{Y}$ must transform as a second-order two-point tensor as in Eq. (B.2b) (Acharya, 2004). To satisfy this invariance requirement of $\boldsymbol{Y}$, the simplest candidate is

$$\boldsymbol{Y} = \boldsymbol{W}\boldsymbol{\gamma}, \tag{B.7}$$

with $\boldsymbol{\gamma}$ being a tensor of thermal expansion coefficients defined in Ω_t that transforms under a rigid body motion as $\boldsymbol{\gamma}^{*} = \boldsymbol{Q}\boldsymbol{\gamma}\boldsymbol{Q}^{T}$, which would give $\boldsymbol{Y}^{*} = \boldsymbol{W}^{*}\boldsymbol{\gamma}^{*} = \boldsymbol{W}\boldsymbol{Q}^{T}\boldsymbol{Q}\boldsymbol{\gamma}\boldsymbol{Q}^{T} = \boldsymbol{W}\boldsymbol{\gamma}\boldsymbol{Q}^{T} = \boldsymbol{Y}\boldsymbol{Q}^{T}$.

C Ericksen's identity

The balance of angular momentum requires the symmetry of the Cauchy stress tensor $\boldsymbol{\sigma}$ (Eq. (2.30)). To analyze the consistency of the right-hand side of Eq. (2.41) as an expression for $\boldsymbol{\sigma}$, we require that Ψ be invariant under any rigid body motion (Acharya and Fressengeas, 2015, Ericksen, 1961), i.e.

$$\Psi^*(\boldsymbol{W}^*, \theta^*, \boldsymbol{\alpha}^*) = \Psi(\boldsymbol{W}, \theta, \boldsymbol{\alpha}) \tag{C.1}$$

for a motion given by Eq. (B.1).

Consider Ψ in an arbitrarily fixed state $(\boldsymbol{W}, \theta, \boldsymbol{\alpha})$, at a given instant of time t, and a specific rigid body motion for which $\boldsymbol{Q}(t) = \mathbb{1}$ and $\dot{\boldsymbol{Q}}(t) = \boldsymbol{P}$, where $\boldsymbol{P}$ is an arbitrarily fixed skew tensor. Next, noting that, under a rigid body motion, $\boldsymbol{W}$ and $\boldsymbol{\alpha}$ transform as in Eq. (B.2b) and Eq. (B.4), respectively, we compute the rate $\dot{\Psi}^*$ as

$$\begin{aligned} \dot{\Psi}^* &= \partial_{\boldsymbol{W}^*}\Psi^* : \dot{\overline{\boldsymbol{W}\boldsymbol{Q}^T}} + \partial_{\theta^*}\Psi^*\dot{\theta}^* + \partial_{\boldsymbol{\alpha}^*}\Psi^* : \dot{\overline{\boldsymbol{\alpha}\boldsymbol{Q}^T}} \\ &= \partial_{\boldsymbol{W}}\Psi : (\dot{\boldsymbol{W}} - \boldsymbol{W}\boldsymbol{P}) + \partial_{\theta}\Psi\dot{\theta} - \partial_{\boldsymbol{\alpha}}\Psi : (\dot{\boldsymbol{\alpha}} - \boldsymbol{\alpha}\boldsymbol{P}). \end{aligned} \tag{C.2}$$

Eq. (C.1) implies $\dot{\Psi}^* = \dot{\Psi}$, such that

$$\begin{aligned} &\left(\boldsymbol{W}^T\partial_{\boldsymbol{W}}\Psi + \boldsymbol{\alpha}^T\partial_{\boldsymbol{\alpha}}\Psi\right) : \boldsymbol{P} = 0 \\ \Longrightarrow\ &\frac{1}{2}\left[\boldsymbol{W}^T\partial_{\boldsymbol{W}}\Psi - (\partial_{\boldsymbol{W}}\Psi)^T\boldsymbol{W} + \boldsymbol{\alpha}^T\partial_{\boldsymbol{\alpha}}\Psi - (\partial_{\boldsymbol{\alpha}}\Psi)^T\boldsymbol{\alpha}\right] = 0 \end{aligned} \tag{C.3}$$

due to the arbitrariness of $\boldsymbol{P}$. The left-hand side of Eq. $(C.3)_2$ is equal to $-\text{skew}(\boldsymbol{\sigma}) = 0$, with $\boldsymbol{\sigma}$ given by Eq. (2.41), which is thus shown to be symmetric. Hence, Eq. (2.41) is consistent with the balance of the angular momentum Eq. (2.30), and also with the requirement of no dissipation due to material spin, given by $\text{skew}(\boldsymbol{L})$.

D Linear stability analysis of the temperature evolution equation

In this section, a 1-d, constant coefficient linear PDE is used to clarify the implications of the temperature evolution statement in Eq. (2.62). For that, we take into account the same temporal and spatial derivatives of θ present and consider

$$a\theta_t + b\theta_{tx} + c\theta_{txx} = d\theta_{xx} + g\theta \tag{D.1}$$

for $a, b, c, d, g \in \mathbb{R}$, and assume $a, d \geq 0$. The subscripts t and x indicate partial differentiation with respect to time and space, respectively, and the last term on the right-hand side incorporates the presence of source terms in Eq. (2.62) that depend linearly on θ. We take the ansatz of a plane-wave solution

$$\theta = \exp\Big(i(kx + \omega t)\Big) \tag{D.2}$$

considering $k \in \mathbb{R}^+$ and insert it into Eq. (D.1) to get

$$\begin{aligned} & ia\omega - b\omega k - ic\omega k^2 = -dk^2 + g \\ \implies & \omega(k) = \frac{dk^2 - g}{i(ck^2 - a) + bk} \frac{\Big[bk - i(ck^2 - a)\Big]}{\Big[bk - i(ck^2 - a)\Big]} \\ \implies & \omega(k) = \frac{(bdk^3 - bgk) - i(cdk^4 - cgk^2 - adk^2 + ag)}{(ck^2 - a)^2 + b^2k^2} \end{aligned} \tag{D.3}$$

which corresponds to the dispersion relation of the plane wave in Eq. (D.2). Denoting $\omega = \omega_R + i\omega_I$, with ω_R and ω_I the real and complex parts of ω, respectively, Eq. (D.2) becomes

$$\theta = \exp(-\omega_I t)\exp\Big(i(kx + \omega_R t)\Big), \tag{D.4}$$

hence showing that the stability of the solution is dependent on the behaviour of $\omega_I(k)$. Consider an initial condition as the superposition of waves with different k:

$$\theta_0(x) = \sum_k A_k \exp(ikx). \tag{D.5}$$

Small perturbations in the initial condition, $\delta\theta_0(x) = \sum_k \delta A_k \exp(ikx)$, may contain components with arbitrarily large k, such that, after some time t, the perturbed solution would be

$$\theta(x,t) + \delta\theta(x,t) = \sum_k (A_k + \delta A_k)\exp(-\omega_I t)\exp\Big(i(kx + \omega_R t)\Big). \tag{D.6}$$

If $\omega_I(k) \to -\infty$ when $k \to \infty$, then the arbitrarily large k in $\delta\theta_0$ would result in unbounded growth of Eq. (D.6) for arbitrarily small t, such that continuous dependence on initial data is not verified and thus the problem is ill-posed. More generally, for a given $M \gg 1$ and $\epsilon \ll 1$ arbitrarily fixed, ill-posed growth implies $\exp(|\omega(k)|\epsilon) \geq M$ for some k. In that case, $\omega(k)$ is an unbounded function of k. Hence, we define "well-posed growth" as growth in the solution (Eq. (D.4)) with time that does not attain arbitrary magnitudes in arbitrarily small time intervals with $\omega(k)$ thus being bounded as a function of k. To assess the boundedness of $\omega_I(k)$, we evaluate it on the limits $k \to \infty$ and $k \to 0$; for $k \in (0, \infty)$, we solve $\omega_I'(k) = 0$ to determine the critical values k^*, and show that $\omega(k^*)$ is bounded.

Case $d = 0$ From Eq. (D.3), we have that

$$\omega(k) = \frac{-bgk + i(cgk^2 - ag)}{(ck^2 - a)^2 + b^2k^2} \tag{D.7}$$

which corresponds to the dispersion relation in the adiabatic case. From Eq. (D.7), we see that the presence of the term in θ_{tx} in Eq. (D.1) leads to a wave-like solution for temperature evolution, with a non-zero real part of ω. In this case, from Eq. (D.7) we have that

$$\lim_{k\to\infty} \omega(k) = 0, \quad \lim_{k\to 0} \omega(k) = -i\frac{g}{a}, \tag{D.8}$$

which shows the boundedness of $\omega_I(k)$, thus guaranteeing well-posed growth for the limiting values of k. Now, taking the derivative of Eq. (D.7), we have

$$\omega_I'(k) = \frac{2gk\left[c\left(b^2k^2 + \left(a - ck^2\right)^2\right) + \left(a - ck^2\right)\left(b^2 - 2c\left(a - ck^2\right)\right)\right]}{\left[b^2k^2 + \left(a - ck^2\right)^2\right]^2}. \tag{D.9}$$

By solving $\omega_I'(k) = 0$, we find each k_i^*, $i = 1,..,5$, where $\omega_I(k)$ attains a maximum or a minimum, which gives

$$\begin{aligned}
&k_1^* = 0; \quad k_2^* = -\sqrt{\frac{ac^2 - b\sqrt{ac^3}}{c^3}}; \quad k_3^* = -k_2^*; \quad k_4^* = -\sqrt{\frac{ac^2 + b\sqrt{ac^3}}{c^3}}; \quad k_5^* = -k_4^* \\
&\omega_I\left(k_1^*\right) = -\frac{g}{a}; \quad \omega_I\left(k_2^*\right) = \frac{gc^{5/2}\sqrt{a}}{b\left(b\sqrt{ac^3} - 2ac^2\right)}; \quad \omega_I\left(k_3^*\right) = \omega_I\left(k_2^*\right); \\
&\omega_I\left(k_4^*\right) = \frac{gc^{5/2}\sqrt{a}}{b\left(b\sqrt{ac^3} + 2ac^2\right)}; \quad \omega_I\left(k_5^*\right) = \omega_I\left(k_4^*\right).
\end{aligned} \tag{D.10}$$

Hence, since all the extrema of ω_I are bounded, we conclude that the solution admits well-posed growth or decay. The values of k that will result in the growth or decay of the solution depend on the sign of the coefficients g and c and can be analysed from Eq. (D.7) by solving

$$\omega_I = \frac{cgk^2 - ag}{(ck^2 - a)^2 + b^2k^2} > 0 \implies g(ck^2 - a) > 0. \tag{D.11}$$

From this equation, the *decay* of the solution occurs for

$$\begin{aligned}
&g > 0, c > 0, k > \sqrt{\frac{a}{c}} \\
&g < 0, \begin{cases} c < 0, k \in \mathbb{R}^+, \\ c > 0, k < \sqrt{\frac{a}{c}} \end{cases},
\end{aligned} \tag{D.12}$$

whereas *well-posed growth* occurs for

$$\begin{aligned}
&g > 0, \begin{cases} c < 0, k \in \mathbb{R}^+, \\ c > 0, k < \sqrt{\frac{a}{c}} \end{cases} \\
&g < 0, c > 0, k > \sqrt{\frac{a}{c}}.
\end{aligned} \tag{D.13}$$

We highlight the fact that, considering the solution as a superposition of plane waves with different k, the wave components whose k lie in a growth region could give rise to a spatial patterning of the temperature profile.

The phase velocity of the adiabatic temperature wave is given by

$$v_p(k) = \frac{\omega_R}{k} = \frac{-bg}{(ck^2 - a)^2 + b^2k^2} \tag{D.14}$$

and is a function of the wavenumber k, such that the solution for θ is in the form of dispersive

waves.

Case $d \neq 0$ From Eq. (D.3), we have

$$\omega_R(k) = \frac{bdk^3 - bgk}{(ck^2 - a)^2 + b^2k^2} \quad \text{and} \quad \omega_I(k) = \frac{(a - ck^2)(dk^2 - g)}{(ck^2 - a)^2 + b^2k^2}. \tag{D.15}$$

Similar to the previous case, we are interested in analysing the boundedness of $\omega_I(k)$, and we have

$$\lim_{k\to-\infty} \omega_I(k) = -\frac{d}{c}, \quad \lim_{k\to 0} \omega_I(k) = -\frac{g}{a}, \tag{D.16}$$

which once again ensures well-posed growth of the solution for the limiting values of k. Deriving ω_I in Eq. (D.15) with respect to k gives

$$\omega_I'(k) = \frac{2k\left[\left(ck^2 - a\right)\left(b^2 - 2c\left(a - ck^2\right)\right)\left(dk^2 - g\right) + \left(b^2k^2 + \left(a - ck^2\right)^2\right)\left(c\left(g - dk^2\right) + d\left(a - ck^2\right)\right)\right]}{\left[\left(a - ck^2\right)^2 + b^2k^2\right]^2} \tag{D.17}$$

As before, solving $\omega_I'(k) = 0$ for k yields five critical points k_i^*, which results in bounded extrema $\omega_I\left(k_i^*\right)$, $i = 1,...,5$, therefore also implying well-posed growth or decay of the solution (the solutions are not shown here due to their considerable size). From Eq. (D.15), the conditions for growth or decay can be established by solving

$$(ck^2 - a)(dk^2 - g) < 0, \tag{D.18}$$

from which the *decay* of the solution occurs for

$$\begin{aligned}
&g > 0, \begin{cases} c < 0, k > \sqrt{\frac{g}{d}} \\ c > 0, \begin{cases} \sqrt{\frac{g}{d}} < k < \sqrt{\frac{a}{c}} & \text{if} \quad \frac{a}{c} > \frac{g}{d} \\ \sqrt{\frac{a}{c}} < k < \sqrt{\frac{g}{d}} & \text{if} \quad \frac{a}{c} < \frac{g}{d} \end{cases} \end{cases} \\
&g < 0, \begin{cases} c < 0, k \in \mathbb{R}^+ \\ c > 0, k > \sqrt{\frac{g}{d}} \end{cases}
\end{aligned} \tag{D.19}$$

whereas *well-posed growth* occurs for

$$g>0,\begin{cases} c<0,\ k<\sqrt{\frac{g}{d}} \\ c>0,\begin{cases} 0<k<\sqrt{\frac{g}{d}} & \text{or} \quad k>\sqrt{\frac{a}{c}} \quad \text{if} \quad \frac{a}{c}>\frac{g}{d} \\ 0<k<\sqrt{\frac{a}{c}} & \text{or} \quad k>\sqrt{\frac{g}{d}} \quad \text{if} \quad \frac{a}{c}<\frac{g}{d} \end{cases} \end{cases} \qquad \text{(D.20)}$$

$$g<0,\ c>0,\ k<\sqrt{\frac{g}{d}}$$

The phase velocity in this case is

$$v_p(k)=\frac{\omega_R}{k}=\frac{b(dk^2-g)}{(ck^2-a)^2+b^2k^2}, \qquad \text{(D.21)}$$

and the solution is again in the form of dispersive waves.

E The Stokes-Helmholtz decomposition of $\boldsymbol{W}$

E.1 Large deformations

It is sometimes convenient to adopt a Stokes-Helmholtz decomposition of $\boldsymbol{W}$ into incompatible (i.e., divergence-free) and compatible (i.e., curl-free) parts for solving problems, e.g. in dislocation statics, the equations of equilibrium and the incompatibility equation pose 12 equations in 9 variables, while having solutions (unique, in the linear case) despite its overdetermined appearance. Thus, we use

$$\boldsymbol{W} = \boldsymbol{\chi} + \nabla \boldsymbol{f} \tag{E.1}$$

where $\boldsymbol{f}$ is to be considered as the plastic position vector (Acharya and Roy, 2006). Now, given $\boldsymbol{\alpha}$, the following equation set allows for the unique determination of $\boldsymbol{\chi}$:

$$\nabla \times \boldsymbol{\chi} = -\boldsymbol{\alpha} \quad \text{in} \quad \Omega_t \tag{E.2a}$$
$$\nabla \cdot \boldsymbol{\chi} = 0 \quad \text{in} \quad \Omega_t \tag{E.2b}$$
$$\boldsymbol{\chi}\hat{\boldsymbol{n}} = 0 \quad \text{on} \quad \partial\Omega_t \tag{E.2c}$$

Note that Eq. (E.2) also ensures that $\boldsymbol{\chi} = 0$ whenever $\boldsymbol{\alpha} = 0$.

To compute the rate of the inverse elastic distortion gradient tensor $\dot{\boldsymbol{W}}$, we perform the analysis in a "relative" description (Acharya, 2004), in which we fix the body in a given configuration $\Omega_{t'}$ at time $t = t'$, and consider a motion from this configuration onwards, parametrised by a time-like variable τ. By denoting $\boldsymbol{x}(t')$ the points in $\Omega_{t'}$, we have that $\boldsymbol{x}_\tau(\tau = 0) = \boldsymbol{x}(t')$, $\boldsymbol{x}_\tau \in \Omega_\tau$. Let $\boldsymbol{F}_\tau$ be the deformation gradient associated with this motion, and ∇_τ the nabla operator in Ω_τ. Then, we can rewrite the decomposition in Eq. (E.1) as

$$\begin{aligned}
&\boldsymbol{W} = \boldsymbol{\chi} + (\nabla_\tau \boldsymbol{f})\boldsymbol{F}_\tau^{-1} \implies \boldsymbol{W}\boldsymbol{F}_\tau = \boldsymbol{\chi}\boldsymbol{F}_\tau + (\nabla_\tau \boldsymbol{f}) \\
\implies &\dot{\boldsymbol{W}}\boldsymbol{F}_\tau + \boldsymbol{W}\dot{\boldsymbol{F}}_\tau = \dot{\overline{\boldsymbol{\chi}\boldsymbol{F}_\tau}} + (\nabla_\tau \dot{\boldsymbol{f}}) \implies \dot{\boldsymbol{W}} + \boldsymbol{W}\dot{\boldsymbol{F}}_\tau\boldsymbol{F}_\tau^{-1} = \dot{\overline{\boldsymbol{\chi}\boldsymbol{F}_\tau}}\boldsymbol{F}_\tau^{-1} + (\nabla_\tau \dot{\boldsymbol{f}})\boldsymbol{F}_\tau^{-1} \\
\implies &\dot{\boldsymbol{W}} = \dot{\overline{\boldsymbol{\chi}\boldsymbol{F}_\tau}}\boldsymbol{F}_\tau^{-1} + (\nabla_\tau \dot{\boldsymbol{f}})\boldsymbol{F}_\tau^{-1} - \boldsymbol{W}\boldsymbol{L}.
\end{aligned} \tag{E.3}$$

Now, we can write

$$\dot{\overline{\boldsymbol{\chi}\boldsymbol{F}_\tau}} = \dot{\boldsymbol{\chi}}\boldsymbol{F}_\tau + \boldsymbol{\chi}\dot{\boldsymbol{F}}_\tau \implies \dot{\overline{\boldsymbol{\chi}\boldsymbol{F}_\tau}}\boldsymbol{F}_\tau^{-1} = \dot{\boldsymbol{\chi}} + \boldsymbol{\chi}\boldsymbol{L} \tag{E.4}$$

such that Eq. (E.3) becomes

$$\dot{\boldsymbol{W}} = \dot{\boldsymbol{\chi}} + \boldsymbol{\chi}\boldsymbol{L} + (\nabla_\tau \dot{\boldsymbol{f}})\boldsymbol{F}_\tau^{-1} - \boldsymbol{W}\boldsymbol{L} \tag{E.5}$$

At $\tau = 0$, Eq. (E.5) evaluates to

$$\dot{\boldsymbol{W}} = \dot{\boldsymbol{\chi}} + \boldsymbol{\chi}\boldsymbol{L} + \nabla\dot{\boldsymbol{f}} - \boldsymbol{W}\boldsymbol{L}. \tag{E.6}$$

which remains valid for any t, since the choice of t' is arbitrary.

As established in Acharya, 2004, $\nabla \boldsymbol{f}$ is related to the permanent deformation of the body. Thus, we would like $\nabla\dot{\boldsymbol{f}}$ to bear a dependence on the general defect evolution in the body, given by $\boldsymbol{\alpha}\times\boldsymbol{v}^d + \boldsymbol{\phi}^\theta$ (Eq. (2.20)). Considering Eq. (2.25), we can write Eq. (E.6) as

$$\begin{aligned}
&\dot{\boldsymbol{W}} + \boldsymbol{W}\boldsymbol{L} = \dot{\boldsymbol{\chi}} + \boldsymbol{\chi}\boldsymbol{L} + \nabla\dot{\boldsymbol{f}} = \boldsymbol{\alpha}\times\boldsymbol{v}^d + \boldsymbol{\phi}^\theta \\
\implies &\nabla\cdot\nabla\dot{\boldsymbol{f}} = \nabla\cdot(\boldsymbol{\alpha}\times\boldsymbol{v}^d + \boldsymbol{\phi}^\theta - \dot{\boldsymbol{\chi}} - \boldsymbol{\chi}\boldsymbol{L}) \quad \text{in} \quad \Omega_t
\end{aligned} \tag{E.7}$$

To obtain a unique solution for $\dot{\boldsymbol{f}}$, Eq. (E.7) requires the following boundary condition

$$(\nabla\dot{\boldsymbol{f}})\hat{\boldsymbol{n}} = (\boldsymbol{\alpha}\times\boldsymbol{v}^d + \boldsymbol{\phi}^\theta - \dot{\boldsymbol{\chi}} - \boldsymbol{\chi}\boldsymbol{L})\hat{\boldsymbol{n}} \quad \text{on} \quad \partial\Omega_t \tag{E.8}$$

where $\hat{\boldsymbol{n}}$ is the outward normal field to $\partial\Omega_t$. It can be shown that the evolution statement in Eq. (E.7) is compatible with dissipation requirements imposed by the second law of thermodynamics (Acharya, 2004, Acharya, 2011).

E.2 Small deformations

Considering Eq. (2.72), we write

$$\boldsymbol{U}^e = \nabla \boldsymbol{u} - \boldsymbol{U}^p - \boldsymbol{\varepsilon}^\theta. \tag{E.9}$$

By denoting $\boldsymbol{A}^{\|}$ the compatible part of a tensor $\boldsymbol{A}$, we have that

$$\boldsymbol{U}^{e\|} = \nabla \boldsymbol{u} - \boldsymbol{U}^{p\|} - \boldsymbol{\varepsilon}^{\theta\|}. \tag{E.10}$$

Hence, we decompose $\boldsymbol{U}^e$, $\boldsymbol{U}^p$ and $\boldsymbol{\varepsilon}^\theta$ into compatible and incompatible parts as

$$\boldsymbol{U}^e = \nabla(\boldsymbol{u} - \boldsymbol{z}) + \zeta; \quad \boldsymbol{U}^p = \nabla \boldsymbol{z}^p + \zeta^p; \quad \boldsymbol{\varepsilon}^\theta = \nabla \boldsymbol{z}^\theta + \zeta^\theta, \tag{E.11}$$

such that, considering Eqs. (E.9) and (E.10), we have the following:

$$\nabla \boldsymbol{z} = \nabla \boldsymbol{z}^p + \nabla \boldsymbol{z}^\theta \tag{E.12}$$

$$\boldsymbol{\zeta} = -\boldsymbol{\zeta}^p - \boldsymbol{\zeta}^\theta. \tag{E.13}$$

The vector $\boldsymbol{z}$ is the "plastic displacement" (Acharya and Roy, 2006) and $\boldsymbol{\zeta}$ is a divergence-free tensor, determined by solving the system

$$\left.\begin{aligned} &\nabla \times \boldsymbol{\zeta} = \boldsymbol{\alpha} \\ &\nabla \cdot \boldsymbol{\zeta} = 0 \end{aligned}\right\} \quad \text{in} \quad \Omega$$
$$\boldsymbol{\zeta}\hat{\boldsymbol{n}} = 0 \qquad \text{on} \quad \partial\Omega, \tag{E.14}$$

similarly to Eq. (E.2). In the small strains approximation, we have that $\boldsymbol{L} = \nabla \boldsymbol{v} = \nabla \dot{\boldsymbol{u}}$, such that, by using Eqs. (2.71) and (E.11), we can write

$$\begin{aligned} &\nabla \dot{\boldsymbol{u}} = \nabla(\dot{\boldsymbol{u}} - \dot{\boldsymbol{z}}) + \dot{\boldsymbol{\zeta}} + \boldsymbol{\alpha} \times \boldsymbol{v}^d + \boldsymbol{\gamma}\dot{\theta} \\ \Longrightarrow\ &\nabla \cdot \nabla \dot{\boldsymbol{z}} = \nabla \cdot (\boldsymbol{\alpha} \times \boldsymbol{v}^d + \boldsymbol{\gamma}\dot{\theta}) \quad \text{in} \quad \Omega, \end{aligned} \tag{E.15}$$

since, in the geometrically linear case, $\dot{\boldsymbol{\zeta}}$ is incompatible (i.e., $\nabla \cdot \dot{\boldsymbol{\zeta}} = 0$). Eq. (E.15) also requires the following boundary condition to ensure the uniqueness of the solution:

$$(\nabla \dot{\boldsymbol{z}})\hat{\boldsymbol{n}} = (\boldsymbol{\alpha} \times \boldsymbol{v}^d + \boldsymbol{\gamma}\dot{\theta})\hat{\boldsymbol{n}} \quad \text{on} \quad \partial\Omega. \tag{E.16}$$

F Derivation of global dissipation rate D

The following identities are used in the derivation:

$$\partial_{\boldsymbol{W}}\Psi : (\boldsymbol{W}\boldsymbol{L}) = \frac{\partial\Psi}{\partial W_{mn}} W_{mi} L_{in} = W_{mi}\frac{\partial\Psi}{\partial W_{mn}} L_{in} = \left(\boldsymbol{W}^T\partial_{\boldsymbol{W}}\Psi\right) : \boldsymbol{L}; \tag{F.1}$$

$$\partial_{\boldsymbol{\alpha}}\Psi : \left(\boldsymbol{\alpha}\boldsymbol{L}^T\right) = \frac{\partial\Psi}{\partial\alpha_{ij}}\alpha_{ip}L_{jp} = \left[(\partial_{\boldsymbol{\alpha}}\Psi)^T\boldsymbol{\alpha}\right] : \boldsymbol{L}; \tag{F.2}$$

$$\begin{aligned}\int_\Omega \boldsymbol{A} : \nabla\times\boldsymbol{B}\,\mathrm{d}v &= \int_\Omega A_{ij}\epsilon_{jkl}B_{il,k}\,\mathrm{d}v = \int_\Omega (A_{ij}\epsilon_{jkl}B_{il})_{,k}\,\mathrm{d}v - \int_\Omega A_{ij,k}\epsilon_{jkl}B_{il}\,\mathrm{d}v \\ &= -\int_{\partial\Omega} A_{ij}\epsilon_{jlk}B_{il}\hat{n}_k\,\mathrm{d}s + \int_\Omega \epsilon_{lkj}A_{ij,k}B_{il}\,\mathrm{d}v = -\int_{\partial\Omega}\boldsymbol{A} : (\boldsymbol{B}\times\hat{\boldsymbol{n}})\,\mathrm{d}s + \int_\Omega(\nabla\times\boldsymbol{A}) : \boldsymbol{B}\,\mathrm{d}v;\end{aligned} \tag{F.3}$$

$$\boldsymbol{A} : \left(\boldsymbol{\alpha}\times\boldsymbol{v}^d\right) = A_{ij}\epsilon_{jkl}\alpha_{ik}v_l^d = A_{ij}\alpha_{ik}\epsilon_{jkl}v_l^d = \left[(\boldsymbol{A}^T\boldsymbol{\alpha}) : \mathbf{X}\right]\cdot\boldsymbol{v}^d. \tag{F.4}$$

For completeness, we recall the global dissipation inequality Eq. (2.39):

$$\begin{aligned}D = &\int_{\Omega_t}\left(\boldsymbol{\sigma} : \boldsymbol{L} - \frac{1}{\theta}\boldsymbol{q}\cdot\nabla\theta\right)\mathrm{d}v + \int_{\Omega_t}\rho\boldsymbol{W}^T\partial_{\boldsymbol{W}}\Psi : \boldsymbol{L}\,\mathrm{d}v - \int_{\Omega_t}\rho\partial_{\boldsymbol{W}}\Psi : \left(\boldsymbol{\alpha}\times\boldsymbol{v}^d + \boldsymbol{W}\boldsymbol{\gamma}\dot{\theta}\right)\mathrm{d}v \\ &- \int_{\Omega_t}\rho\partial_{\boldsymbol{\alpha}}\Psi : \left[-\mathrm{tr}(\boldsymbol{L})\boldsymbol{\alpha} + \boldsymbol{\alpha}\boldsymbol{L}^T - \nabla\times\left(\boldsymbol{\alpha}\times\boldsymbol{v}^d + \boldsymbol{W}\boldsymbol{\gamma}\dot{\theta}\right)\right]\mathrm{d}v - \int_{\Omega_t}\rho\left(\partial_\theta\Psi + \eta\right)\dot{\theta}\,\mathrm{d}v \geq 0,\end{aligned} \tag{F.5}$$

After separating terms, we get

$$D = \int_{\Omega_t} \Big[\rho \boldsymbol{W}^T \partial_{\boldsymbol{W}} \Psi : \boldsymbol{W}\boldsymbol{L} - \rho \boldsymbol{W}^T \partial_{\boldsymbol{W}} \Psi : (\boldsymbol{\alpha} \times \boldsymbol{v}^d) - \rho \boldsymbol{W}^T \partial_{\boldsymbol{W}} \Psi : \boldsymbol{W}\boldsymbol{\gamma}\dot{\theta} - \rho \partial_\theta \Psi \dot{\theta} \\ - \rho \partial_{\boldsymbol{\alpha}} \Psi : (\boldsymbol{\alpha}\boldsymbol{L}^T) + \rho \mathrm{tr}(\boldsymbol{L}) \partial_{\boldsymbol{\alpha}} \Psi : \boldsymbol{\alpha} + \rho \partial_{\boldsymbol{\alpha}} \Psi : \nabla \times (\boldsymbol{\alpha} \times \boldsymbol{v}^d + \boldsymbol{W}\boldsymbol{\gamma}\dot{\theta}) - \rho\eta\dot{\theta} \Big] \mathrm{d}v \quad \text{(F.6)} \\ + \int_{\Omega_t} \left(\boldsymbol{\sigma} : \boldsymbol{L} - \frac{1}{\theta} \boldsymbol{q} \cdot \nabla\theta \right) \mathrm{d}v \geq 0.$$

By using Eqs. (F.1) to (F.4) in Eq. (F.6), and regrouping the terms in $\boldsymbol{L}$, $\dot{\theta}$, and $\boldsymbol{v}^d$, we obtain Eq. (2.40).

G Evaluation of the derivatives of Ψ for a Saint-Venant-Kirchhoff material

G.1 Large deformations

We make use of the following identity:

$$\frac{\partial W^{-1}_{il}}{\partial W_{mn}} = -W^{-1}_{im} W^{-1}_{nl} \left(\hat{\boldsymbol{e}}_i \otimes \hat{\boldsymbol{e}}_l \otimes \hat{\boldsymbol{e}}_m \otimes \hat{\boldsymbol{e}}_n \right), \tag{G.1}$$

which can be readily obtained from partial derivation with respect to $\boldsymbol{W}$ of $\boldsymbol{W}^{-1}\boldsymbol{W} = \mathbb{1}$. With this in hand, consider the following derivatives of Ψ (Eq. (2.85)):

$$\begin{aligned} \frac{1}{\rho}\boldsymbol{W}^{-T}\boldsymbol{\sigma}_H = \partial_{\boldsymbol{W}}\Psi = \frac{1}{2\rho_0}\partial_{\boldsymbol{W}}(\boldsymbol{E} : \mathbb{C} : \boldsymbol{E}) = \frac{1}{\rho_0}\frac{\partial E_{ij}}{\partial F^e_{pq}}\frac{\partial W^{-1}_{pq}}{\partial W_{mn}} C_{ijkl} E_{kl} \\ = -\frac{1}{\rho_0}(\boldsymbol{W}^{-T}\boldsymbol{W}^{-1})(\mathbb{C} : \boldsymbol{E})\boldsymbol{W}^{-T}; \end{aligned} \tag{G.2}$$

$$\begin{aligned} \partial^2_{\boldsymbol{W}\boldsymbol{W}}\Psi = \frac{\partial^2\Psi}{\partial W_{mn}\partial W_{rs}} = \frac{\partial}{\partial W_{rs}}\left(-\frac{1}{\rho_0} W^{-1}_{im} W^{-1}_{ik} \mathbb{C}_{kjpq} E_{pq} W^{-1}_{nj} \right) \\ = -\frac{1}{\rho_0}\mathbb{C}_{kjpq}\left(\frac{\partial W^{-1}_{im}}{\partial W_{rs}} W^{-1}_{ik} W^{-1}_{nj} E_{pq} + W^{-1}_{im}\frac{\partial W^{-1}_{ik}}{\partial W_{rs}} W^{-1}_{nj} E_{pq} + W^{-1}_{im} W^{-1}_{ik}\ \frac{\partial W^{-1}_{nj}}{\partial W_{rs}} E_{pq} \right. \\ \left. + W^{-1}_{im} W^{-1}_{ik} W^{-1}_{nj}\ \frac{\partial E_{pq}}{\partial F^e_{ab}}\frac{\partial W^{-1}_{ab}}{\partial W_{rs}} \right) \\ = \frac{1}{\rho_0}\mathbb{C}_{kjpq}\left(W^{-1}_{ir} W^{-1}_{sm} W^{-1}_{ik} W^{-1}_{nj} E_{pq} + W^{-1}_{im} W^{-1}_{ir} W^{-1}_{sk} W^{-1}_{nj} E_{pq} + W^{-1}_{im} W^{-1}_{ik}\ W^{-1}_{nr} W^{-1}_{sj} E_{pq} \right. \\ \left. + W^{-1}_{im} W^{-1}_{ik} W^{-1}_{nj}\ W^{-1}_{aq} W^{-1}_{ar} W^{-1}_{sp} + W^{-1}_{im} W^{-1}_{ik} W^{-1}_{nj} W^{-1}_{ap} W^{-1}_{ar} W^{-1}_{sq} \right); \end{aligned} \tag{G.3}$$

$$\partial_{\boldsymbol{\alpha}}\Psi = \frac{\xi}{\rho_0}\boldsymbol{\alpha} \implies \partial^2_{\boldsymbol{\alpha}\boldsymbol{\alpha}}\Psi = \frac{\xi}{\rho_0}\mathbb{1}\otimes\mathbb{1}; \tag{G.4}$$

$$\partial_\theta\Psi = -\frac{1}{\rho_0}\boldsymbol{\beta} : \boldsymbol{E} - c_\varepsilon \ln\frac{\theta}{\theta_0} \implies \partial^2_{\theta\theta}\Psi = -\frac{c_\varepsilon}{\theta}; \tag{G.5}$$

G.2 Small deformations

The following derivatives are given for the Ψ expression in Eq. (2.88):

For compactness, denote $\boldsymbol{A} \equiv (\boldsymbol{\varepsilon} - \boldsymbol{\varepsilon}^p)$. Then,

$$\begin{aligned}\partial_{\boldsymbol{A}}\Psi &= \frac{1}{2\rho_0}\frac{\partial}{\partial A_{mn}}\Big(A_{ij}\mathbb{C}_{ijkl}A_{kl}\Big) - \frac{\Delta\theta}{\rho_0}\beta_{ij}\frac{\partial A_{ij}}{\partial A_{mn}} = \frac{1}{2\rho_0}\Big(\delta_{im}\delta_{jn}\mathbb{C}_{ijkl}A_{kl} + A_{ij}\mathbb{C}_{ijkl}\delta_{km}\delta_{ln}\Big) - \frac{\Delta\theta}{\rho_0}\beta_{ij}\delta_{im}\delta_{jn} \\ &= \frac{1}{\rho_0}\mathbb{C} : \boldsymbol{A} - \frac{\Delta\theta}{\rho_0}\boldsymbol{\beta} \quad \text{since } \mathbb{C}_{ijkl} = \mathbb{C}_{klij}\end{aligned} \tag{G.6}$$

$$\partial^2_{\boldsymbol{A}\theta} = \partial^2_{\theta\boldsymbol{A}} = -\frac{1}{\rho_0}\boldsymbol{\beta} \tag{G.7}$$

The other partial derivatives of Ψ are the same as in G.1.

H Supplementary figures for Chapter 3

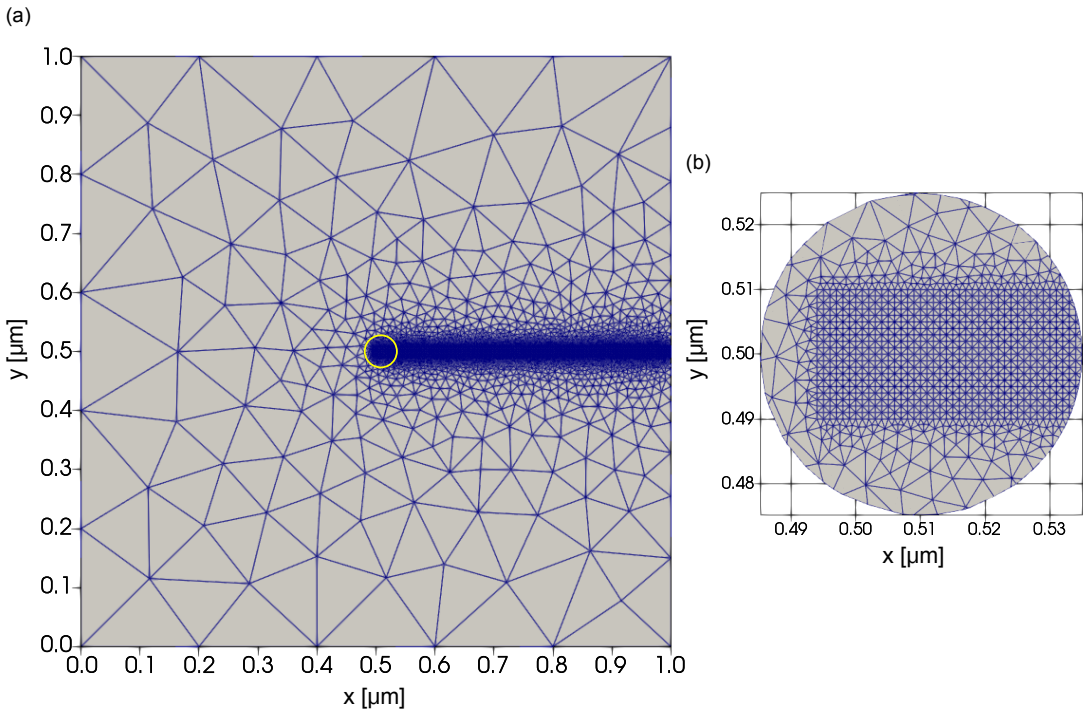

Figure H.1: Mesh used for the model verification in Section 3.5.1. The element size in the structured region is $h = 1$ nm. The yellow circle in (a) indicates the zoomed region depicted in (b)

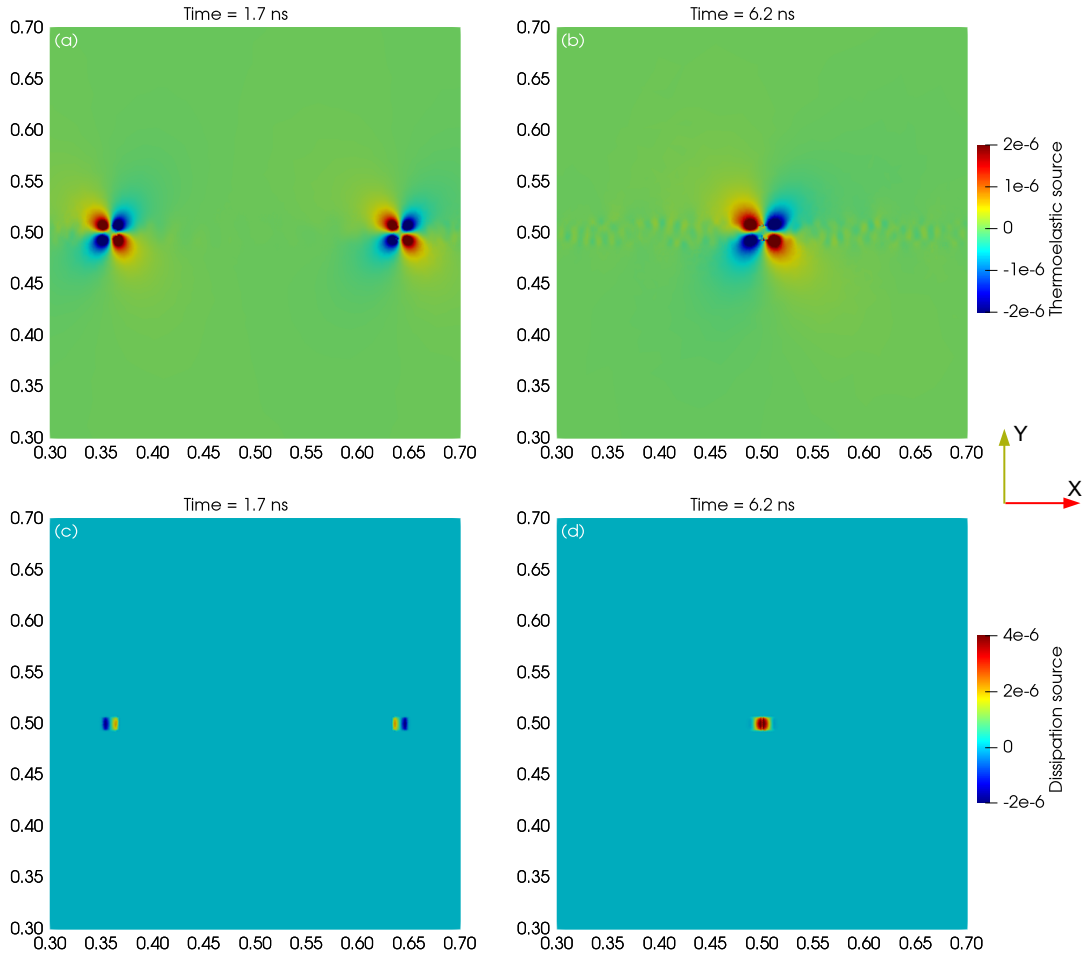

Figure H.2: Heat sources evolution during the dislocation annihilation simulation for the time steps depicted in Fig. 3.5b and c. The dimensions are in µm, and the plots are zoomed in the central region of the (1×1) µm^2 domain of Fig. 3.5a to c. (a) and (b): thermoelastic heat sources; (c) and (d): plastic dissipation heat sources. The corresponding colour bars are on the right of figures (b) and (d).

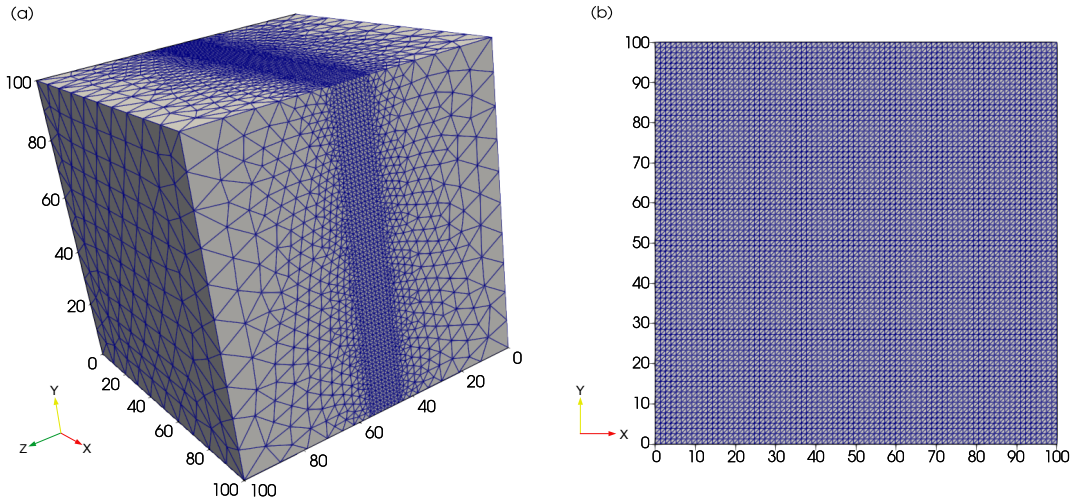

Figure H.3: Mesh used for the dislocation loop simulation in Section 3.5.2.3. (a) 3D perspective showing the structured and unstructured regions; (b) 2D view of the $z = 49.36$ plane showing the structured region where the loop expansion occurs. The dimensions are in nm.

Bibliography

Volterra, V. (1907). Sur l'équilibre des corps élastiques multiplement connexes. *Annales scientifiques de l'École normale supérieure*, *24*, 401–517.

Frenkel, J. (1926). Zur Theorie der Elastizitätsgrenze und der Festigkeit kristallinischer Körper. *Zeitschrift für Physik*, *37*(7), 572–609.

Orowan, E. (1934). Zur Kristallplastizität. III. *Zeitschrift für Physik*, *89*(9), 634–659.

Polanyi, M. (1934). Über eine Art Gitterstörung, die einen Kristall plastisch machen könnte. *Zeitschrift für Physik*, *89*(9), 660–664.

Taylor, G. I. (1934). The mechanism of plastic deformation of crystals. Part I.—Theoretical. *Proceedings of the Royal Society of London. Series A, Containing Papers of a Mathematical and Physical Character*, *145*(855), 362–387.

Taylor, G. I., & Quinney, H. (1934). The latent energy remaining in a metal after cold working. *Proceedings of the Royal Society of London. Series A, Containing Papers of a Mathematical and Physical Character*, *143*(849), 307–326.

Burgers, J. (1939). Some considerations on the fields of stress connected with dislocations in a regular crystal lattice. I. *KNAW, Proceedings*, *42*, 293.

Cattaneo, C. (1948). Sulla conduzione del calore. *Atti Semin. Mat. Fis. della Università di Modena*, *3*(3).

Peach, M., & Koehler, J. S. (1950). The Forces Exerted on Dislocations and the Stress Fields Produced by Them. *Physical Review*, *80*(3), 436–439.

Nye, J. (1953). Some geometrical relations in dislocated crystals. *Acta Metallurgica*, *1*(2), 153–162.

Eshelby, J. (1956). The Continuum Theory of Lattice Defects. In *Solid State Physics* (pp. 79–144, Vol. 3). Elsevier.

Bilby, B., Gardner, L., & Stroh, A. (1957). Extrait des actes du ix congrès international de mechanique appliqueè.

Kröner, E. (1958). *Kontinuumstheorie der Versetzungen und Eigenspannungen*. Springer Berlin Heidelberg.

Kröner, E. (1959). Allgemeine Kontinuumstheorie der Versetzungen und Eigenspannungen. *Archive for Rational Mechanics and Analysis*, *4*(1), 273–334.

deWit, R. (1960). The Continuum Theory of Stationary Dislocations. In *Solid State Physics* (pp. 249–292, Vol. 10). Elsevier.

Ericksen, J. L. (1961). Conservation Laws for Liquid Crystals. *Transactions of the Society of Rheology*, *5*(1), 23–34.

Mura, T. (1963). Continuous distribution of moving dislocations. *Philosophical Magazine*, *8*(89), 843–857.

Stojanovic, R., Djuric, S., & Vujosevic, L. (1964). On finite thermal deformations. *Archiwum Mechaniki Stosowanej*, *16*, 103–108.

Willis, J. (1967). Second-order effects of dislocations in anisotropic crystals. *International Journal of Engineering Science*, *5*(2), 171–190.

Lee, E. H. (1969). Elastic-Plastic Deformation at Finite Strains. *Journal of Applied Mechanics*, *36*(1), 1–6.

Clifton, R. J. (1972). On the Equivalence of FeFp and FpFe. *Journal of Applied Mechanics*, *39*(1), 287–289.

Bever, M., Holt, D., & Titchener, A. (1973). The stored energy of cold work. *Progress in Materials Science*, *17*, 5–177.

Gevers, R., Landuyt, J. v., & Amelinckx, S. (1978). *Diffraction and imaging techniques in material science* (2d, rev. ed). North-Holland Pub. Co. Sole distributors for the U.S.A.; Canada, Elsevier North-Holland.

Kosevich, A. M. (1979). Crystal dislocations and the theory of elasticity. In F. R. N. Nabarro (Ed.), *Dislocations in solids* (pp. 33–141). North-Holland publ.

Hirth, J. P., & Lothe, J. (1982). *Theory of dislocations* (2nd ed). Wiley.

Nemat-Nasser, S. (1982). On finite deformation elasto-plasticity. *International Journal of Solids and Structures*, *18*(10), 857–872.

Joseph, D. D., & Preziosi, L. (1989). Heat waves. *Reviews of Modern Physics*, *61*(1), 41–73.

Kubin, L. P., Canova, G., Condat, M., Devincre, B., Pontikis, V., & Bréchet, Y. (1992). Dislocation Microstructures and Plastic Flow: A 3D Simulation. *Solid State Phenomena*, *23-24*, 455–472.

Chaboche, J.-L. (1993). Cyclic Viscoplastic Constitutive Equations, Part I: A Thermodynamically Consistent Formulation. *Journal of Applied Mechanics*, *60*(4), 813–821.

Lubarda, V. A. (1999). Duality in constitutive formulation of finite-strain elastoplasticity based on F=FeFp and F=FpFe decompositions. *International Journal of Plasticity*, *15*(12), 1277–1290.

Rittel, D. (1999). On the conversion of plastic work to heat during high strain rate deformation of glassy polymers. *Mechanics of Materials*, *31*(2), 131–139.

Rosakis, P., Rosakis, A. J., Ravichandran, G., & Hodowany, J. (2000). A thermodynamic internal variable model for the partition of plastic work into heat and stored energy in metals. *Journal of the Mechanics and Physics of Solids*, *48*(3), 581–607.

Acharya, A. (2001). A model of crystal plasticity based on the theory of continuously distributed dislocations. *Journal of the Mechanics and Physics of Solids*, *49*(4), 761–784.

Weygand, D., Friedman, L. H., van der Giessen, E., & Needleman, A. (2001). Discrete dislocation modeling in three-dimensional confined volumes. *Materials Science and Engineering: A*, *309-310*, 420–424.

Elder, K. R., Katakowski, M., Haataja, M., & Grant, M. (2002). Modeling Elasticity in Crystal Growth. *Physical Review Letters*, *88*(24), 245701.

Vujosevic, L., & Lubarda, V. A. (2002). Finite-strain thermoelasticity based on multiplicative decomposition of deformation gradient. *Theoretical and Applied Mechanics*, 379–399.

Acharya, A. (2003). Driving forces and boundary conditions in continuum dislocation mechanics. *Proceedings of the Royal Society of London. Series A: Mathematical, Physical and Engineering Sciences*, *459*(2034), 1343–1363.

Acharya, A. (2004). Constitutive analysis of finite deformation field dislocation mechanics. *Journal of the Mechanics and Physics of Solids*, *52*(2), 301–316.

Truesdell, C., Noll, W., & Antman, S. S. (2004). *The Non-Linear Field Theories of Mechanics* [OCLC: 851383987]. Springer Berlin Heidelberg.

Benzerga, A., Bréchet, Y., Needleman, A., & Van der Giessen, E. (2005). The stored energy of cold work: Predictions from discrete dislocation plasticity. *Acta Materialia*, *53*(18), 4765–4779.

Roy, A., & Acharya, A. (2005). Finite element approximation of field dislocation mechanics. *Journal of the Mechanics and Physics of Solids*, *53*(1), 143–170.

Acharya, A., & Roy, A. (2006). Size effects and idealized dislocation microstructure at small scales: Predictions of a Phenomenological model of Mesoscopic Field Dislocation Mechanics: Part I. *Journal of the Mechanics and Physics of Solids*, *54*(8), 1687–1710.

Bulatov, V., & Cai, W. (2006, November). *Computer Simulations of Dislocations*. Oxford University Press.

Roy, A., & Acharya, A. (2006). Size effects and idealized dislocation microstructure at small scales: Predictions of a Phenomenological model of Mesoscopic Field Dislocation Mechanics: Part II. *Journal of the Mechanics and Physics of Solids*, *54*(8), 1711–1743.

Varadhan, S. N., Beaudoin, A. J., Acharya, A., & Fressengeas, C. (2006). Dislocation transport using an explicit Galerkin/least-squares formulation. *Modelling and Simulation in Materials Science and Engineering*, *14*(7), 1245–1270.

Hochrainer, T., Zaiser, M., & Gumbsch, P. (2007). A three-dimensional continuum theory of dislocation systems: kinematics and mean-field formulation. *Philosophical Magazine*, *87*(8-9), 1261–1282.

Fivel, M. C. (2008). Discrete dislocation dynamics: an important recent break-through in the modelling of dislocation collective behaviour. *Comptes Rendus Physique*, *9*(3), 427–436.

Acharya, A. (2010). New inroads in an old subject: Plasticity, from around the atomic to the macroscopic scale. *Journal of the Mechanics and Physics of Solids*, *58*(5), 766–778.

Bammann, D. J., & Solanki, K. N. (2010). On kinematic, thermodynamic, and kinetic coupling of a damage theory for polycrystalline material. *International Journal of Plasticity*, *26*(6), 775–793.

Stainier, L., & Ortiz, M. (2010). Study and validation of a variational theory of thermo-mechanical coupling in finite visco-plasticity. *International Journal of Solids and Structures*, *47*(5), 705–715.

Acharya, A. (2011). Microcanonical Entropy and Mesoscale Dislocation Mechanics and Plasticity. *Journal of Elasticity*, *104*(1-2), 23–44.

Acharya, A., & Tartar, L. (2011). On an equation from the theory of field dislocation mechanics. *Bollettino della Unione Matematica Italiana. Series IX*, *3*.

Hull, D., & Bacon, D. J. (2011). *Introduction to dislocations* (5. ed). Butterworth Heinemann, Elsevier.

Logg, A., Mardal, K.-A., & Wells, G. (Eds.). (2012). *Automated Solution of Differential Equations by the Finite Element Method: The FEniCS Book*. Springer.

Zhao, D., Zhu, Y., Ying, L., Hu, P., & Zhang, W. (2013). Modeling and experimental verification of thermo-mechanical coupled behavior of face-centered-cubic polycrystals. *Materials & Design (1980-2015)*, *52*, 289–294.

Hochrainer, T., Sandfeld, S., Zaiser, M., & Gumbsch, P. (2014). Continuum dislocation dynamics: Towards a physical theory of crystal plasticity. *Journal of the Mechanics and Physics of Solids*, *63*, 167–178.

Acharya, A., & Fressengeas, C. (2015). Continuum Mechanics of the Interaction of Phase Boundaries and Dislocations in Solids. In G.-Q. G. Chen, M. Grinfeld, & R. J. Knops (Eds.), *Differential geometry and continuum mechanics* (pp. 123–165). Springer International Publishing.

Acharya, A., & Zhang, X. (2015). From dislocation motion to an additive velocity gradient decomposition, and some simple models of dislocation dynamics. *Chinese Annals of Mathematics, Series B*, *36*, 645–658.

Djaka, K. S., Taupin, V., Berbenni, S., & Fressengeas, C. (2015). A numerical spectral approach to solve the dislocation density transport equation. *Modelling and Simulation in Materials Science and Engineering*, *23*(6), 065008.

Hochrainer, T. (2015). Multipole expansion of continuum dislocations dynamics in terms of alignment tensors. *Philosophical Magazine*, *95*(12), 1321–1367.

McAuliffe, C., & Waisman, H. (2015). A unified model for metal failure capturing shear banding and fracture. *International Journal of Plasticity*, *65*, 131–151.

Zhang, X., Acharya, A., Walkington, N. J., & Bielak, J. (2015). A single theory for some quasi-static, supersonic, atomic, and tectonic scale applications of dislocations. *Journal of the Mechanics and Physics of Solids*, *84*, 145–195.

Hochrainer, T. (2016). Thermodynamically consistent continuum dislocation dynamics. *Journal of the Mechanics and Physics of Solids*, *88*, 12–22.

Valdenaire, P.-L., Le Bouar, Y., Appolaire, B., & Finel, A. (2016). Density-based crystal plasticity: From the discrete to the continuum. *Physical Review B*, *93*(21), 214111.

Gurrutxaga-Lerma, B. (2017). How strong is the temperature increase due to a moving dislocation? *International Journal of Solids and Structures*, *108*, 263–274.

Mariano, P. M. (2017). Finite-speed heat propagation as a consequence of microstructural changes. *Continuum Mechanics and Thermodynamics*, *29*(6), 1241–1248.

Rittel, D., Zhang, L., & Osovski, S. (2017). The dependence of the Taylor–Quinney coefficient on the dynamic loading mode. *Journal of the Mechanics and Physics of Solids*, *107*, 96–114.

Rodney, D., Ventelon, L., Clouet, E., Pizzagalli, L., & Willaime, F. (2017). Ab initio modeling of dislocation core properties in metals and semiconductors. *Acta Materialia*, *124*, 633–659.

Sadik, S., & Yavari, A. (2017). On the origins of the idea of the multiplicative decomposition of the deformation gradient. *Mathematics and Mechanics of Solids*, *22*(4), 771–772.

Clouet, E. (2018). Ab Initio Models of Dislocations. In W. Andreoni & S. Yip (Eds.), *Handbook of Materials Modeling : Methods: Theory and Modeling* (pp. 1–22). Springer International Publishing.

Nieto-Fuentes, J. C., Rittel, D., & Osovski, S. (2018). On a dislocation-based constitutive model and dynamic thermomechanical considerations. *International Journal of Plasticity*, *108*, 55–69.

Bertin, N., Aubry, S., Arsenlis, A., & Cai, W. (2019). GPU-accelerated dislocation dynamics using subcycling time-integration. *Modelling and Simulation in Materials Science and Engineering*, *27*(7), 075014.

Morin, L., Brenner, R., & Suquet, P. (2019). Numerical simulation of model problems in plasticity based on field dislocation mechanics. *Modelling and Simulation in Materials Science and Engineering*, *27*(8), 085012.

Acharya, A., & Viñals, J. (2020). Field dislocation mechanics and phase field crystal models. *Physical Review B*, *102*(6), 064109.

Arora, R., & Acharya, A. (2020a). Dislocation pattern formation in finite deformation crystal plasticity. *International Journal of Solids and Structures*, *184*, 114–135.

Arora, R., & Acharya, A. (2020b). A unification of finite deformation J2 Von-Mises plasticity and quantitative dislocation mechanics. *Journal of the Mechanics and Physics of Solids*, *143*, 104050.

Arora, R., Zhang, X., & Acharya, A. (2020). Finite element approximation of finite deformation dislocation mechanics. *Computer Methods in Applied Mechanics and Engineering*, *367*, 113076.

Bertin, N., Sills, R. B., & Cai, W. (2020). Frontiers in the Simulation of Dislocations. *Annual Review of Materials Research*, *50*(1), 437–464.

Starkey, K., Winther, G., & El-Azab, A. (2020). Theoretical development of continuum dislocation dynamics for finite-deformation crystal plasticity at the mesoscale. *Journal of the Mechanics and Physics of Solids*, *139*, 103926.

Upadhyay, M. V. (2020). On the thermo-mechanical theory of field dislocations in transient heterogeneous temperature fields. *Journal of the Mechanics and Physics of Solids*, *145*, 104150.

Kositski, R., & Mordehai, D. (2021). Employing molecular dynamics to shed light on the microstructural origins of the Taylor-Quinney coefficient. *Acta Materialia*, *205*, 116511.

Upadhyay, M. V., & Bleyer, J. (2021). Dislocation transport using a time-explicit Runge-Kutta discontinuous Galerkin finite element approach. *Modelling and Simulation in Materials Science and Engineering*.

Arora, A., Arora, R., & Acharya, A. (2022). Mechanics of micropillar confined thin film plasticity. *Acta Materialia*, *238*, 118192.

Cui, Y., Li, K., Wang, C., & Liu, W. (2022). Dislocation evolution during additive manufacturing of tungsten. *Modelling and Simulation in Materials Science and Engineering*, *30*(2), 024001.

Felder, S., Kopic-Osmanovic, N., Holthusen, H., Brepols, T., & Reese, S. (2022). Thermo-mechanically coupled gradient-extended damage-plasticity modeling of metallic materials at finite strains. *International Journal of Plasticity*, *148*, 103142.

Grilli, N., Hu, D., Yushu, D., Chen, F., & Yan, W. (2022). Crystal plasticity model of residual stress in additive manufacturing using the element elimination and reactivation method. *Computational Mechanics*, *69*(3), 825–845.

Li, Z., Wang, T., Chu, D., Liu, Z., & Cui, Y. (2022). A coupled crystal-plasticity and phase-field model for understanding fracture behaviors of single crystal tungsten. *International Journal of Plasticity*, *157*, 103375.

Mariano, P. M., & Spadini, M. (2022). Sources of Finite Speed Temperature Propagation. *Journal of Non-Equilibrium Thermodynamics*, *47*(2), 165–178.

Starkey, K., & El-Azab, A. (2022). Total Lagrange implementation of a finite-deformation continuum dislocation dynamics model of mesoscale plasticity. *International Journal of Plasticity*, *155*, 103332.

Stimac, J. C., Bertin, N., Mason, J. K., & Bulatov, V. V. (2022). Energy storage under high-rate compression of single crystal tantalum. *Acta Materialia*, *239*, 118253.

Xiong, Q.-l., Li, Z., Shimada, T., & Kitamura, T. (2022). Atomistic investigation on the conversion of plastic work to heat in high-rate shear deformation. *International Journal of Plasticity*, *149*, 103158.

Zeng, Q., Wang, T., Zhu, S., Chen, H.-s., & Fang, D. (2022). A rate-dependent phase-field model for dynamic shear band formation in strength-like and toughness-like modes. *Journal of the Mechanics and Physics of Solids*, *164*, 104914.

Arora, A., Arora, R., & Acharya, A. (2023). Interface-Dominated Plasticity and Kink Bands in Metallic Nanolaminates. *Crystals*, *13*(5), 828.

Bertin, N., & Zhou, F. (2023). Accelerating discrete dislocation dynamics simulations with graph neural networks. *Journal of Computational Physics*, *487*, 112180.

Dæhli, L. E. B., Johnsen, J., Berstad, T., Børvik, T., & Hopperstad, O. S. (2023). An experimental–numerical study on the evolution of the Taylor–Quinney coefficient with plastic deformation in metals. *Mechanics of Materials*, *179*, 104605.

Gaudez, S., Abdesselam, K. A., Gharbi, H., Hegedüs, Z., Lienert, U., Pantleon, W., & Upadhyay, M. V. (2023). High-resolution reciprocal space mapping reveals dislocation structure evolution during 3D printing. *Additive Manufacturing*, *71*, 103602.

Longère, P. (2023). Thermodynamically consistent strain hardening variable/driving force, inelastic stored energy and self-heating in dynamic plasticity. *Mechanics of Materials*, *184*, 104728.

Rubin, M. B., & Bardella, L. (2023). An Eulerian thermodynamical formulation of size-dependent plasticity. *Journal of the Mechanics and Physics of Solids*, *170*, 105122.

Yavari, A., & Sozio, F. (2023). On the direct and reverse multiplicative decompositions of deformation gradient in nonlinear anisotropic anelasticity. *Journal of the Mechanics and Physics of Solids*, *170*, 105101.

Lima-Chaves, G. D., & Upadhyay, M. V. (2024). Finite element implementation of the thermal field dislocation mechanics model: Study of temperature evolution due to dislocation activity. *Computer Methods in Applied Mechanics and Engineering*, *421*, 116763.

Lima-Chaves, G. D., Acharya, A., & Upadhyay, M. V. (2024). A finite deformation theory of dislocation thermomechanics.

Upadhyay, M. V., & Viñals, J. (2024, March). Coupling Phase Field Crystal and Field Dislocation Mechanics for a consistent description of dislocation structure and elasticity [arXiv:2404.08658 [cond-mat]].

ECOLE DOCTORALE

Titre : Sur la thermomécanique des champs de dislocation

Mots clés : dislocations, mécanique des solides, plasticité, thermoélasticité, FEM

Résumé :
Cette thèse explore le couplage entre l'évolution des dislocations et la conduction thermique dans les corps continus, via des approches théoriques et numériques. Les principaux résultats sont : (i) une théorie thermomécanique des champs de dislocations en grandes déformations, considérant l'interaction entre dislocations et température, basée sur des variables observables ; (ii) l'implémentation numérique de la théorie en petites déformations (TFDM) via la méthode des éléments finis.
Une nouvelle théorie thermo-élastoplastique, sans décomposition multiplicative du gradient de déformation, est proposée, basée sur la mécanique des dislocations dans un champ thermique hétérogène. En utilisant uniquement des variables observables, il est démontré que la conservation du vecteur de Burgers suffit pour aboutir à la décomposition additive du gradient de vitesse spatiale. En considérant la densité de dislocations comme variable d'état dans l'énergie libre de Helmholtz et en appliquant les lois de la thermodynamique, une équation d'évolution de la température est dérivée, permettant des solutions sous forme d'ondes dispersives avec vitesse finie.
Après linéarisation, la théorie se réduit à TFDM. Une formulation variationnelle des équations est résolue numériquement par éléments finis, vérifiée par une solution analytique du champ de température généré par une dislocation en mouvement, avec un excellent accord. Les capacités de TFDM sont illustrées par des exemples comme la chaleur générée par des dislocations, leur annihilation, et l'expansion des boucles de dislocation.
Cette recherche contribue pour la compréhension de l'interaction entre l'evolution des dislocations et les champs transitoires de température. Des travaux futurs étendront l'implémentation numérique à la théorie en grandes déformations pour inclure les dislocations stockées statistiquement, ouvrant ainsi la voie pour la compréhension de l'évolution des dislocations pendant des procédés thermoméchaniques.

Title : On the thermomechanics of field dislocations

Keywords : dislocations, solid mechanics, plasticity, thermoelasticity, FEM

Abstract : This thesis explores the coupling between dislocation evolution and heat conduction in continuum bodies through theoretical and numerical approaches. The main outcomes are: (i) a thermomechanical theory of field dislocations that considers the interaction between dislocation activity and temperature evolution, allowing for finite deformations and based on observable fields; and (ii) to numerically implement the small-deformation thermal field dislocation mechanics (TFDM) theory using the finite element method.
After presenting the limitations in the state of the art, a theory with novel kinematics for thermo-elastoplastic problems is proposed, based on dislocation mechanics within a transient heterogeneous temperature field. The theory requires neither a global reference configuration nor a multiplicative decomposition of the deformation gradient. Instead, using only observable state variables, it is shown that kinematics based on the conservation of the Burgers vector is sufficient to arrive at the well-accepted additive decomposition of the spatial velocity gradient. By including dislocation density as a state variable in the Helmholtz free energy and applying the laws of thermodynamics, derive a specific structure of the temperature evolution equation is derived, allowing for solutions in the form of dispersive waves with finite propagation speed.
After geometrical linearisation, the theory reduces to the previously proposed small-strain TFDM theory. Focussing on the latter, a variational formulation of its partial differential equations is developped and numerically implemented via the finite element method in a staggered algorithm using an open-source library. The implementation is verified against an analytical solution for the temperature field generated by a moving dislocation, showing excellent agreement. Then, the capabilities of TFDM are explored in examples such as heat generated by single-edge and screw dislocations, dislocation annihilation, and dislocation loop expansion.
This research contributes to the understanding of the interaction between dislocation evolution and transient temperature fields. Future work will extend the numerical implementation to the large deformation theory to include statistically stored dislocations, allowing for a better understanding of dislocation evolution during thermomechanical processes.

Institut Polytechnique de Paris
91120 Palaiseau, France